Near-field exploration of light-matter interactions on gold and van der Waals materials

Casses, Laura

Publication date:
2022

Document Version
Publisher's PDF, also known as Version of record

Citation (APA):
Casses, L. (2022). *Near-field exploration of light-matter interactions on gold and van der Waals materials*. Technical University of Denmark.

PhD thesis in Photonics Engineering

DTU Electro
Department of Electrical and Photonics Engineering

Near-field exploration of light-matter interactions on gold and van der Waals materials

Laura N. Casses

November 2022

Supervisor: Assoc. Prof. Nicolas Leitherer-Stenger
Co-supervisors: Assoc. Prof. Martijn Wubs & Assoc. Prof. Sanshui Xiao

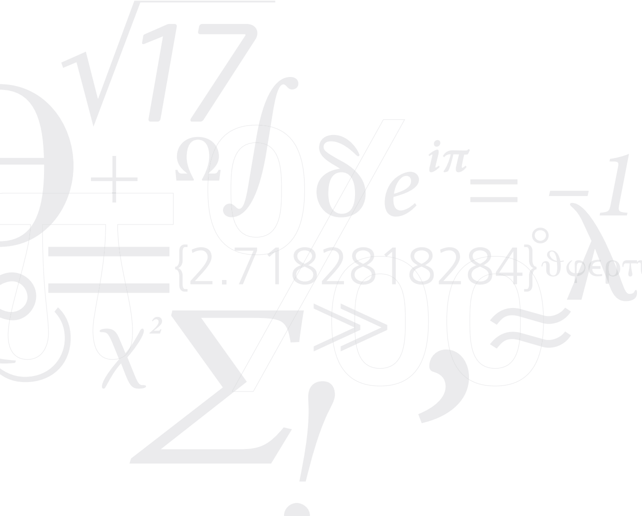

DTU Electro
Department of Electrical and Photonics Engineering
Technical University of Denmark
Ørsteds Plads
Building 340
2800 Kongens Lyngby, Denmark

Preface

This thesis is submitted in fulfillment of the requirements for the degree of Doctor of Philosophy (PhD) at the Technical University of Denmark (DTU). The project has been carried out in the Structured Electromagnetic Materials group at DTU Electro, from September 2019 to November 2022, under the supervision of Assoc. Prof. Nicolas Leitherer-Stenger, Assoc. Prof. Martijn Wubs and Assoc. Prof. Sanshui Xiao. The research has been financed by DTU Electro and the Danish National Research Foundation within the Center for Nanostructured Graphene (CNG, project DNRF103).

The research activities of CNG focus on two-dimensional materials and the control of their electrical, thermal and optical properties. In this PhD thesis, we investigate the near-field properties of surface plasmon polaritons propagating at the interface between air and monocrystalline gold. This project was carried out in collaboration with Dr. Korbinian J. Kaltenecker, from Attocube Systems AG. We then study the interaction of the surface plasmons with excitons in tungsten diselenide thin films.

Kongens Lyngby, 30th November 2022

Laura N. Casses

Abstract

The subwavelength confinement of light is a key requirement for future nanophotonic devices. As such, the subwavelength field confinement of polaritons, such as surface plasmon polaritons (SPPs) or exciton polaritons, makes them attractive for various applications such as nanocircuits, sensing, light generation and solar energy conversion. Due to their subwavelength confinement, these polaritons are however difficult to characterize directly with conventional microscopes. Near-field optical microscopy allows the visualization of strongly confined polaritons.

In this PhD work, we first study the near-field amplitude and phase of SPPs on a monocrystalline gold platelet, in the visible spectral range and with a near-field microscope in a reflection configuration. Due to the moderate confinement of these SPPs compared to SPPs in materials such as graphene, the full quantitative characterization of the wavelength and propagation length of these polaritons is challenging. Indeed, multiple excitation pathways of these polaritons lead to complex interference patterns. We measure the near-field amplitude and phase for six different angles between the incident light and the edge of the platelet. We find that the signals from the SPPs excited at an atomic force microscope tip are best isolated from the signals coming from the other excitation pathways at grazing incident angle. Moreover, we introduce a simple model to describe the amplitude and phase profiles. This model explains the $\pi/2$ phase shift observed between these profiles. Using this model, the wavelength and propagation length of the tip-launched plasmons are retrieved by isolating and fitting the profiles far from the platelets' edges. Our experimental results are in excellent agreement with theoretical models using gold refractive index values from the literature.

With this acquired knowledge, we study the coupling between the previously characterized SPPs and excitons in a van der Waals material transferred on a gold platelet. The chosen material is tungsten diselenide (WSe_2). As WSe_2 is a uniaxial anisotropic crystal, we derive 2×2 transmission and propagation matrices to calculate the dispersion relation of polaritons on this multilayered structure. A slightly lower confinement and coupling between the excitons and the SPPs is predicted when the anisotropy of WSe_2 is taken into account, compared to the case where WSe_2 is considered as isotropic. The theoretical dispersion relation is compared to measurements of the experimental dispersion relation reconstructed from near-field measurements of polaritons at several consecutive excitation energies. A small back-bending of the experimental dispersion relation is observed.

The presented methods to fully characterize the SPP complex wavevector could enable the quantitative analysis of moderately confined polaritons occurring in different materials in a reflection configuration and at visible wavelengths.

Resumé

Rumlig begrænsning af lys langt under størrelsen på en optisk bølgelængde er et nøglekrav for fremtidige nanofotoniske enheder. Det medfører at den rumlige feltbegrænsning ved polaritoner, såsom overfladeplasmonpolaritoner (SPP'er) eller exciton-polaritoner, gør dem attraktive til forskellige anvendelser såsom nanokredsløb, sensing, lysgenerering og solenergikonvertering. Medført deres rumlige feltbegrænsning, langt under størrelsen på optiske bølgelængder, er disse polaritoner dog vanskelige at karakterisere direkte med konventionelle mikroskoper. Optisk nærfeltsmikroskopi gør det muligt at visualisere stærkt begrænsede polaritoner.

I dette ph.d.-arbejde studerer vi først nærfelts amplitude og fase af SPP'er på en monokrystallinsk guldplade, i det synlige spektralområde og med et nærfeltsmikroskop i en reflektionskonfiguration. På grund af den moderate rumlige begrænsning af disse SPP'er sammenlignet med SPP'er i materialer som grafen, er den fulde kvantitative karakterisering af bølgelængden og udbredelseslængden af disse polaritoner udfordrende. Naturligt, fører flere excitationsveje for disse polaritoner til komplekse interferensmønstre. Vi måler nærfeltets amplitude og fase for seks forskellige vinkler mellem det indfaldende lys og kanten af guldpladen. Det findes, at signalerne fra SPP'erne exciteret ved en atomar kraftmikroskops-spids er bedst isoleret fra signalerne, der kommer fra de andre excitationsveje ved komplementær-indfaldsvinklen. Desuden introducerer vi en simpel model til at beskrive amplitude- og faseprofilerne. Denne model forklarer $\pi/2$ faseforskydningen observeret mellem disse profiler. Ved hjælp af denne model hentes bølgelængden og udbredelseslængden af de spidsudsendte plasmoner ved at isolere og tilpasse profilerne langt fra guldpladernes kanter. Vores eksperimentelle resultater er i fremragende overensstemmelse med teoretiske modeller, der bruger guld brydningsindeksværdier fra litteraturen.

Med denne erhvervede viden studerer vi koblingen mellem de tidligere karakteriserede SPP'er og excitoner i et van der Waals materiale overført på en guldplade. Det valgte materiale er wolframdiselenid (WSe_2). Da WSe_2 er en enakset anisotrop krystal, udleder vi 2×2 transmissions- og udbredelsesmatricer for at beregne spredningsforholdet mellem polaritoner på denne flerlagsstruktur. En lidt mindre feltbegrænsning og kobling mellem excitonerne og SPP'erne forudsiges, når anisotropien af WSe_2 tages i betragtning, sammenlignet med tilfældet, hvor WSe2 betragtes som isotropisk. Den teoretiske spredningsrelation sammenlignes med målinger af den eksperimentelle spredningsrelation rekonstrueret ud fra nærfeltsmålinger af polaritoner ved flere fortløbende excitationsenergier. En lille tilbagebøjning af den eksperi-

mentelle dispersionsrelation observeres.

De præsenterede metoder til komplet karakterisering af den komplekse bølgevektor for SPP'er, kunne muliggøre den kvantitative analyse af moderat feltbegrænsede polaritoner, der forekommer i forskellige materialer i en reflektionskonfiguration og ved synlige bølgelængder.

Acknowledgements

First and foremost, I would like to thank my supervisors, Nicolas Leitherer-Stenger, Martijn Wubs and Sanshui Xiao. All of them have provided a great help and guidance during these three years, on all aspects of the PhD project. In addition, I would like to give a special thanks to Nicolas for his involvement in the experimental side of the project and Martijn for his active help on the theory side. I am also grateful for their reassurance about the progress of this PhD project, whenever I needed it.

On the experimental side, I also would like to thank Korbinian Kaltenecker for introducing me to the s-SNOM and further discussions about it. I thank Enno Schatz for providing the monocrystalline gold platelets, answering questions and reacting to our feedback. I thank Qiaoling Lin for exfoliating and transferring the WSe_2 on the gold. I am also grateful to Binbin Zhou for helping me install and work with the Fusion and Tsunami lasers, as well as to Henrik Lassen for a peaceful share of the s-SNOM, and Peter Uhd Jepsen for allowing us to use his lab. I also thank to the kick-starting members of the Nanophoton center, who allowed me to embark on the dielectric nano-cavities journey for a while. Finally, thanks to Moritz Fischer for listening and reacting to my complaints about things not working, from Matlab codes to experiments in the lab.

On the theory side, I would like to express my gratitude to the theoreticians in the group for their insightful comments, advice and discussions about how to move forward on the theory or test my results. Special thanks to Mads Jørgensen for his insight on the Dude model.

Additionally, this PhD project would not have been the same without an open and welcoming group. I would thus like to thank my colleagues from the SEM group, past and present, for the general good mood and support, amongst whom the famous Felix Schöpf.

I have met many people during these three years, at the Fotonik (now Electro) Department and at the Friday bar, a number of whom I now consider friends. I would thus like to thank all of them, and in particular, I would like to thank Morten Fisker and Quenting Saadan for arranging regular dinner and board game events on Saturdays during Covid, and so much more. Thanks also to the DnD team, especially the people who introduced our little group to this game: Dr. Emvil and Soon-to-be-Dr. Mads. Furthermore, I would like to thank David and Nicolai for the regular beer meetings, where there is always a good atomsphere. Last but not least, I want to thank my most recent flatmates, Robert and Pratikshya, for their support through their daily talks and cheerfulness.

Finally, a big thanks to my family and friends abroad, who have supported me from different countries. In particular, I would like to acknowledge the scientific side of my family, who inspired me to pursue physics, and my sister, with whom I will always share a deep bond.

List of publications

Journal publications

Included in this thesis

- **Quantitative near-field characterization of surface plasmon polaritons on monocrystalline gold platelets**
  Laura N. Casses, Korbinian J. Kaltenecker, Sanshui Xiao, Martijn Wubs, and Nicolas Stenger
  Opt. Express, **30**(7), 11181-11191 (2022).

Additional work

- **Mono-crystalline gold platelets: a high-quality platform for surface plasmon polaritons**
  Korbinian J. Kaltenecker, Enno Krauss, Laura Casses, Mathias Geisler, Bert Hecht, N. Asger Mortensen, Peter Uhd Jepsen and Nicolas Stenger
  Nanophotonics, **9**(2), 509-522 (2020).

- **Nanometer-scale photon confinement in topology-optimized dielectric cavities**
  Marcus Albrechtsen, Babak Vosoughi Lahijani, Rasmus Ellebæk Christiansen, Vy Thi Hoang Nguyen, Laura Nevenka Casses, Søren Engelberth Hansen, Nicolas Stenger, Ole Sigmund, Henri Jansen, Jesper Mørk and Søren Stobbe
  Nat. Commun., **13**(1), 1-8 (2022).

Conference contributions

- **Near-field characterization of surface plasmon polaritons on monocrystalline gold platelets**
  Laura N. Casses, Korbinian J. Kaltenecker, Sanshui Xiao, Martijn Wubs, and Nicolas Stenger
  METANANO **2021** (Poster)

- **Quantitative near-field characterization of surface plasmon polaritons on single-crystalline gold platelets**
  Laura N. Casses, Korbinian J. Kaltenecker, Sanshui Xiao, Martijn Wubs, and Nicolas Stenger
  2nd International Nanoscale Analytics Workshop (INAW2), **2022** (Presentation)

- **Near-field characterization of surface plasmon polaritons on single-crystalline gold platelets**
  Laura N. Casses, Korbinian J. Kaltenecker, Sanshui Xiao, Martijn Wubs, and Nicolas Stenger
  12th International Conference on Elastic, Electrical, Transport, and Optical Properties of Inhomogeneous Media (ETOPIM), **2022** (Presentation)

- **Shot-filling effects in nanometer-scale electron-beam lithography**
  Marcus Albrechtsen, Babak Vosoughi Lahijani, Rasmus Ellebæk Christiansen, Vy Thi Hoang Nguyen, Laura Nevenka Casses, Søren Engelberth Hansen, Philip Trøst Kristensen, Nicolas Stenger, Ole Sigmund, Henri Jansen, Jesper Mørk, and Søren Stobbe
  47th Micro and Nano Engineering (MNE) Conference, **2021** (Poster)

Abbreviations

Al_2O_3	Aluminum oxide
AFM	Atomic force microscope
BS	Beam-splitter
CB	Conduction band
COM	Coupled oscillator model
CW	Circular wave
FFT	fast Fourier transform
FT	Fourier transform
FTIR	Fourier transform infra-red
FTS	Fourier transform spectroscopy
HeNe	helium-neon
NA	Numerical aperture
PD	Photodiode
PDMS	Polydimethylsiloxane
PsHet	Pseudo-heterodyne
PW	Plane wave
QED	Quantum electrodynamics
RMS	root-mean-square
ROI	Region of interest
SiO_2	Silicon oxide
SPP	Surface plasmon polariton

s-SNOM	Scattering-type near-field optical microscope
TMDC	Transition metal dichalcogenide
TMM	Transfer matrix method
VB	Valence band

Contents

Preface i

Abstract iii

Resumé v

Acknowledgements vii

List of publications ix

Abbreviations xi

Contents xiii

Introduction 1

1 Near-field and s-SNOM techniques 5
- 1.1 Working principle of s-SNOM 5
  - 1.1.1 Atomic force microscopy 5
  - 1.1.2 Tip illumination and interaction with the sample 7
  - 1.1.3 Non-interferometric detection of the near field 8
- 1.2 Additional detection schemes 12
  - 1.2.1 Pseudo-heterodyne detection 12
  - 1.2.2 Fourier-transform spectroscopy 15
- 1.3 Experimental setup 18

2 Optical properties of metals 21
- 2.1 The Drude model 21
- 2.2 Refractive index of gold 23
- 2.3 Surface plasmon polaritons 24

3 Characterization of surface plasmon polaritons (SPPs) 27
- 3.1 The different excitation channels of SPPs 28

3.1.1 Tip-launched SPPs 28
3.1.2 Edge-launched and tip-reflected edge-launched SPPs 29
3.2 Isolation of the tip-launched SPPs 31
3.2.1 Experimental details 32
3.2.2 Amplitude and phase profiles 33
3.2.3 Influence of the incident angle 34
3.3 Derivation of expressions for the near-field profiles 38
3.3.1 Measurement profiles 38
3.3.2 Amplitude 40
3.3.3 Phase 41
3.3.4 Perspectives and limits 43
3.4 Retrieval of the wavelength and propagation length of SPPs 45
3.4.1 Analysis of the tip-launched SPP profiles on gold 45
3.4.2 Fourier transform of plane and circular waves 47
3.4.3 Wavelength and propagation length on gold 49
3.5 Summary 51

4 Coupling between excitons and SPPs 53
4.1 Excitons in transition metal dichalcogenides 53
4.2 Optical dielectric functions of transition metal dichalcogenides 56
4.3 Light-matter coupling and the coupled-oscillator model 58
4.4 Theoretical dispersion relation with plasmon-exciton coupling 60
4.4.1 The transfer matrix method 60
4.4.2 Theoretical dispersion relation for evanescent waves in a multilayer structure 63
4.5 Theoretical dispersion relation with anisotropy 66
4.5.1 Uniaxial anisotropic materials 66
4.5.2 Anisotropic transfer matrix method 68
4.5.3 Theoretical dispersion relation with anisotropic WSe_2 69

5 s-SNOM measurements of the coupled system 71
5.1 Sample fabrication 71
5.1.1 Exfoliation of TMDs 71
5.1.2 Dry transfer on gold 72
5.2 Experimental details for the near-field measurements 74
5.3 Near-field measurements: dispersion relation on gold 74
5.3.1 The different field contributions 75
5.3.2 Fourier filtering 77
5.3.3 Dispersion relation and comparison with the theory 78
5.4 Near-field measurements of WSe_2 on gold 80
5.4.1 The different field contributions 80
5.4.2 Dispersion relations and comparison with the theory 82

Conclusion and outlook **87**

Appendices **91**

Appendix A Pseudo-heterodyne detection - detailed calculations **93**
A.1 Fourier components and multiplication 93
A.2 Back-check of equations 1.23 and 1.24 94

Appendix B Sources and detectors **95**
B.1 Sources 95
B.2 Detectors 96

Appendix C Additional measurements of SPPs at grazing angle **97**
C.1 First additional measurement: $\varphi = -1.4°$ 97
C.2 Second additional measurement: $\varphi = -0.4°$ 98

Appendix D Transfer matrix method **101**
D.1 Matlab code used to calculated the dispersion relation in the case of the isotropic TMM 101
D.1.1 Main code 101
D.1.2 Total matrix function 104
D.1.3 Transmission matrix function 104
D.1.4 Propagation matrix function 105
D.2 Derivation of the impedance coefficients for uniaxial anisotropic crystals 106

Bibliography **107**

Introduction

The invention of the optical microscope, at the end of the 16^{th} century, led to fundamental discoveries, such as the first observation of cells and bacteria [1]. In the following centuries, the spatial resolution of microscopes has been greatly improved, but an important limit was reached: the diffraction limit.

The diffraction limit is a consequence of two effects [2]. To understand these effects, let us consider the case of two point sources that radiate light. As these sources are points, they have infinite spatial frequencies. However, some of the light spatial frequencies are bound to the source and do not propagate towards the image. These components are called the evanescent waves, or near field. The propagation of light thus induces an effective low-pass filtering of the spatial frequencies. Furthermore, an optical microscope collects light at a limited angle given by the numerical aperture (NA), leading to an even stronger filtering. Thus, the image of each point source has a finite size defined by the Airy disk. In Abbe's formulation of the diffraction limit [2], the minimum distance between distinguishable images of two point sources is defined as the radius of the Airy disk

$$r_{\text{Abbe}} = \frac{0.6098\lambda}{\text{NA}}, \tag{1}$$

where λ is the wavelength of the light.

Can we break the diffraction limit with an optical microscope? In 1928, Synge proposed that placing a small metallic aperture close to an illuminated object results in sub-diffraction imaging [3]. His idea was first implemented in the optical regime in 1983 by Pohl et al. [4], using a metal-coated quartz tip as a near-field probe. A spatial resolution of $\lambda/20$, well below the diffraction limit, was demonstrated. In the 1990s, the first aperture-less scanning optical microscopes, or scattering-type scanning optical microscopes (s-SNOMs), based on atomic force microscopes (AFMs) were developed [5, 6]. Since then, s-SNOMs enabled to study many materials in the near field [7], ranging from metallic structures [8–10] to dielectrics [11, 12]. The development of interferometric detection techniques allowed to record both the amplitude and phase of the near field [13, 14], as well as removing the far-field background [14]. Furthermore, hyperspectral imaging in the near field was achieved by developing nano-Fourier transform infrared spectroscopy (nano-FTIR) [15], and allowed the full spacial and temporal [16] and spectral [17] characterization of surface waves. Today, s-SNOM is a versatile optical microscope that can be used for imaging in both transmission and reflection configurations. In the transmission configuration, the light source is placed below the sample, while top-illumination is used in the reflection configuration. Hence, only the reflection configuration allow measurements of samples with non-transparent substrates.

Surface plasmon polaritons (SPPs) have the ability to confine light far beyond the diffraction limit. SPPs are collective excitations of the electronic cloud and propagate at the interface between a dielectric (such as air) and a metal [18]. As such, their electric field is evanescent out of this interface's plane. The light confinement is important for applications such as plasmonic nanocircuits [8, 19], sensing [20, 21], light harvesting [22] and light generation [23, 24]. For several of these applications, the distance over which SPPs can propagate along the interface, i.e. the propagation length, is critical. However, high losses in metals [25] hinder long propagation lengths. The direct characterization of plasmonic structures can help assessing their near-field characteristics. For gold structures, s-SNOM enabled the characterization of the wavelength and propagation length of plasmonic slot waveguides [8], and of the resonance of the guided modes on metasurfaces [9]. The use of near-field measurements was also highlighted as a way to provide feedback to the design and fabrication of metasurfaces [26].

Losses in metals are partly attributed to the electron scattering at grain boundaries [27, 28]. Large monocrystalline gold platelets [29, 30] have therefore attracted a lot of attention because of their potential to reduce the electron scattering losses. These platelets were indeed reported to have better plasmonic resonances and to host SPPs with longer propagation lengths in plasmonic nanocircuits [31], particularly in the regime where Ohmic losses are predominant [32]. In addition, the efficiency of gap plasmon based metasurfaces could be increased by the use of monocrystalline gold [33]. The direct characterization of SPPs on monocrystalline gold platelets with s-SNOM can help assessing the quality of these platelets. Using a s-SNOM in a transmission configuration, the wavelength and propagation length of plasmonic slot waveguides made out of monocrystalline gold was characterized [32], and non-local effects in highly confined gap plasmon modes were identified [34]. In the reflection configuration, the analysis of the near-field signal is more demanding because the SPPs can be excited through several pathways, leading to complex interference patterns [35, 36]. In a previous study [36], the means to extract the wavelength of the SPPs excited at the tip - i.e. the tip-launched SPPs - has been demonstrated. However, the propagation length on a monocrystalline gold platelets using a s-SNOM in the reflection configuration and in the visible could not be retrieved.

Plasmonics can be used to enhance the optical properties of light emitters, such as excitons in transition metal dichalcogenides (TMDCs). TMDCs are part of the van der Waals materials, which are characterized by a layered structure with strong covalent bounds within a layer, but weak van der Waals forces between the layers [37]. TMDCs are well-known for their strong interaction with light [37], which can be used in applications such as nano-lasers [38], light detection [39] and solar energy conversion [40]. Indeed, thin layers of these materials host strong excitons at room temperature, with resonances in the visible and near-infrared range [41, 42]. Due to their layered structure, TMDCs are highly anisotropic [43], a property that was recently highlighted as having potential for future-generation photonic devices [44,45]. Moreover, as they are naturally passivated, they can easily be integrated with other photonic structures [37]. In the case of plasmonic structures, excitons in TMDCs can interact with the plasmons to create plasmon-exciton polaritons. Due to the subwavelength scale of these polaritons, the direct measurement of their wavelength and propagation length requires near-field techniques.

The near-field study and characterization of polaritons in van der Waals materials has been performed in many studies, across the optical spectrum [16,17,46–52]. In the mid-infrared wavelength range, s-SNOM allowed to directly observe highly confined plasmons in graphene [47, 48] and to show that graphene-boron nitride structures improve the propagation length of these plasmons [49]. In the same spectral range, in-plane anisotropic propagation of phonon polaritons in α-MoO$_3$ [50] has been characterized, revealing a high confinement and very low losses of these polaritons. In the close near-infrared to visible range, the dispersion relation of exciton-polaritons in MoSe$_2$ [51] and in WSe$_2$ [52] has been retrieved from s-SNOM measurements. However, to the best of our knowledge, no full near-field characterization of the coupling between monocrystalline gold platelets and excitons in TMDCs in the visible range had been performed at the beginning of this PhD work.

The main objective of this thesis is to study, in a quantitative way, the plasmon-exciton polaritons arising from the coupling of SPPs on monocrystalline gold and excitons in TMDCs. Thus, we want to characterize their wavelength and propagation length - as it is directly related to to their confinement and their losses - as a function of the excitation energy.

In Chapter 1, the basic principles of s-SNOM techniques are presented. This includes the principles of AFM, the effect of tip illumination, the retrieval of the near field from the far-field background, pseudo-heterodyne (PsHet) detection and nano-FTIR. Lastly, the experimental setup used in this thesis is described.

In Chapter 2, the optical properties of metals are introduced. The Drude model and its limitations to describe the properties of metals are explained, and the SPPs characteristics are presented.

In Chapter 3, the characterization of SPPs on monocrystalline gold platelets is described. The different SPP excitation channels are presented and the means to isolate the signal relevant for the characterization is described. In particular, the importance of the angle between the edge of the platelet and the in-plane light incidence is highlighted. The derivation of a model for the near-field amplitude and phase obtained with a s-SNOM in a reflection configuration is presented, and is used to retrieve the wavelength and the propagation length of the SPPs on gold.

In Chapter 4, the basic properties of TMDCs and their dielectric constants are presented. The different possible forms of coupling between excitons and SPPs are explained. Furthermore, the transfer matrix method (TMM) is introduced to calculate the dispersion relation of excitons in WSe$_2$ interacting with SPPs on monocrystalline gold. As WSe$_2$ is an anisotropic materials, an anisotropic TMM, taking into account the two dielectric constants of WSe_2, is derived and its predictions are compared to predictions made with the usual TMM that neglects anisotropy.

In Chapter 5, preliminary results showing the reconstruction of the dispersion relation of polaritons on a fabricated sample composed of WSe_2 on a monocrystalline gold platelet are discussed. As the laser used for the near-field measurements is changed to make these experiments, the dispersion relation is first measured on bare gold to check the quality of the data. Thereafter, the near-field measurements of WSe_2 on gold are described, and the dispersion relation retrieved from these measurements is analyzed.

CHAPTER 1

Near-field and s-SNOM techniques

s-SNOMs have proven to be powerful tools for the study of various materials at a scale of a few tens of nanometers and across the optical spectrum [47, 48, 52–54].

In this chapter, the basics of the s-SNOM techniques used in this thesis are presented. First, the working principle of a s-SNOM setup is explained. Models describing the tip-sample interaction are shortly introduced, and the methods for retrieving the near-field signal out of the background are derived. Additional detection methods for complete background suppression and for spectroscopy are then presented. Finally, the experimental setup used in this thesis is described.

1.1 Working principle of s-SNOM

To be able to operate properly, the simplest version of a s-SNOM needs at least an AFM-based setup, a laser focused on the probing tip, and a background removal scheme. These three elements are described in the following sections.

1.1.1 Atomic force microscopy

A s-SNOM is typically based on an AFM setup [55]. An AFM uses the forces acting on an object placed close to a surface to keep a probe (called *tip* in the following because of the pointed shape of its extremity) at an established position above the sample of interest. Thus, when scanning a sample, a change in the height of the sample is directly translated in a change of the tip height. In this section, the fundamental principles of atomic force microscopy are described, with the help of the concepts described in the book *Atomic Force Microscopy* by P. Eaton and P. West [56].

An AFM has two main operation modes to measure the topography of a sample: the contact mode and the oscillating mode. In the contact mode, the AFM probing tip is kept at a constant distance from the sample. This is done by measuring the deflection of the tip cantilever caused by the interaction with the surface, and using a feedback loop to correct for the changes in deflection. In contrast, in the oscillating mode, the changes in the tip oscillation amplitude are detected and corrected for with the feedback loop. s-SNOMs are usually driven in the intermittent contact - or *tapping* - mode. This sub-category of oscillating mode facilitates the detection of the near-field optical signals, as is shown in section 1.1.3.

A sketch of the generalized operation principle of an AFM in intermittent contact mode, in the specific case of our setup, is presented in Figure 1.1a. The cantilever - holding the tip - is driven by a piezoelectric transducer (piezo) at its resonant oscillation frequency. To detect the resulting tip oscillations, a deflection laser is pointed at the back end of the cantilever, where it is reflected towards a four quadrant photodiode (PD). The four quadrant PD detects the movements of the tip in the vertical and horizontal directions continuously during the scan. For each PD measurement, a feedback loop compares the expected output oscillations amplitude - corresponding to a certain height above the sample - with the real output. The difference between the expected output and the real output corresponds to an error in the height above the sample. Using a proportional–integral–derivative (PID) controller, the height of the tip is adjusted to correct for the errors. The tip height at each point of the scanned region gives the topography of the sample.

Figure 1.1b shows a generic force-distance curve for a tip oscillating above a sample surface. Far from the surface, there is no interaction force between the tip and sample surface (i.e. Force = 0 nN). When approaching the surface, the tip first experiences the attractive van der Waals forces (Force $<$ 0 nN). When approaching even closer, the interaction forces become repulsive (Force $>$ 0 nN) due to Pauli repulsion. In the oscillating mode, coming closer to the sample surface results in a damping of the cantilever oscillations, and thus a reduction of the oscillation amplitude.

Despite having a lot of similarities with an AFM, a s-SNOM setup differs from it on a few points. First and foremost, light coming from a second laser is focused on the tip apex at each position of the scan. Thus for practical reasons, the sample is moved in x-, y- and z-directions during the scan instead of the tip and the light focus [57]. Second, the tip apexes are usually larger than the AFM ones and often

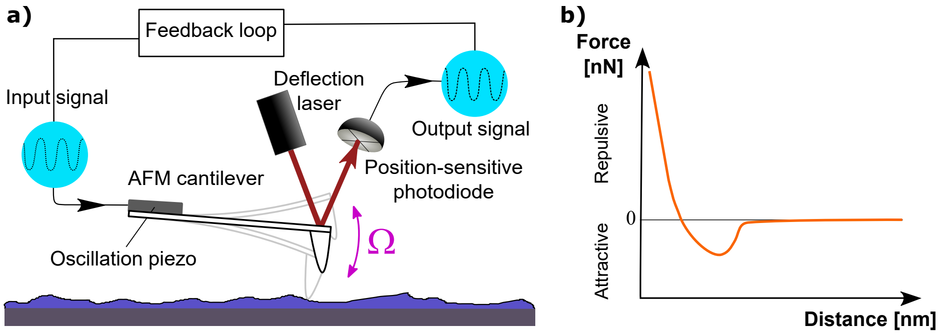

Figure 1.1. AFM principles. a) AFM setup operating in tapping mode. b) Generic force-distance curve for a tip oscillating above a surface.

coated with a metal like platinum. While the precision on the topography is thereby reduced, having a larger tip apex allows to have a higher scattering cross-section at the apex, and thus more near-field signal [58].

The effect of the laser focused on the tip apex and the extraction of the near field are explained in the next section.

1.1.2 Tip illumination and interaction with the sample

Contrary to an AFM, in a s-SNOM setup an additional light source is focused on the tip apex [7, 58, 59]. This - typically polarized - light induces a polarization of the tip, which becomes an oscillating dipole and scatters the light in all directions. As such, the sharp tip apex behaves as an optical antenna: it confines the incident light and converts it into a localized field through scattering [2]. The field amplitudes resulting from this effect in the case of *p*-polarization and *s*-polarization are simulated in Figures 1.2a and 1.2b, respectively. The figures are taken from [52] and simulated for visible wavelengths. This simulation has been done using 3D COMSOL models for a standard-shape tip (ARROW-NCPt from Nanoworld) above a multilayer of WSe_2 [52]. The nano-focusing effect [19] due to the tip - leading to a resolution far beyond the diffraction limit - can be seen in particular in the case of the *p*-polarization.

A simple model to obtain a qualitative understanding of the tip-sample interaction consists in approximating the tip apex as a polarizable sphere, thereby neglecting the influence of the tip shaft. This model is referred to as the point dipole model [11,58,59]. A representation of the point dipole model with *p*- and *s*-polarizations is shown in Figures 1.2c and 1.2d), respectively. The following paragraphs summarize the model.

A sphere of radius R and dielectric constant ϵ_{tip}, at a distance H from the sample

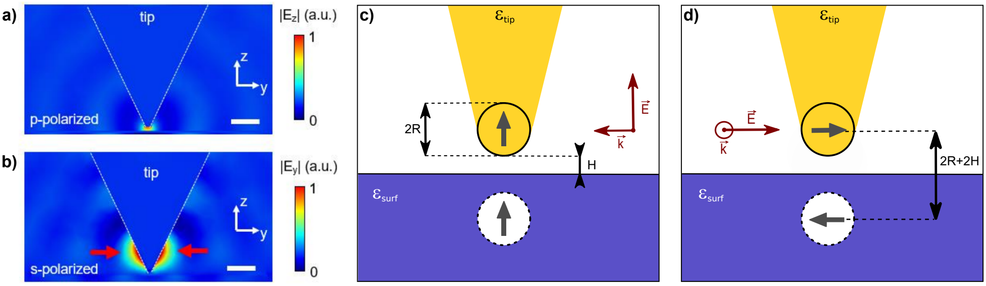

Figure 1.2. Tip nano-focusing and point dipole model. a) COMSOL calculations of the field distribution for a realistic tip shape and *p*-polarization of the light. The scale bar corresponds to 500 nm. Reprinted figure with permission from Ref. [52]. Copyright 2022 by the American Physical Society. b) Same simulation in the case of *s*-polarization. c) Point dipole model in the case of *p*-polarization. d) Point dipole model in the case of *s*-polarization.

surface has a polarizability that can be expressed as [7, 58, 60]:

$$\alpha = 4\pi R^3 \frac{\epsilon_{\text{tip}} - 1}{\epsilon_{\text{tip}} + 2} \tag{1.1}$$

The sample is considered to be a semi-infinite, homogeneous and isotropic material with a relative permittivity ϵ_{surf}. As the tip dipole is very close to the surface, it changes the surface charge distribution, effectively creating an image dipole at a distance $H + R$ under the surface. The image dipole has a relative strength $\beta = (\epsilon_{\text{surf}} - 1)/(\epsilon_{\text{surf}} + 1)$. As depicted in Figures 1.2b and 1.2c, the polarization of the image dipole is aligned with the polarization of the tip dipole. The image dipole and the tip dipole interact with each other and thus lead to the effective polarizability of both dipoles [7, 58]:

$$\alpha_{\text{eff,p}} = \frac{\alpha(1+\beta)}{1 - \frac{\alpha\beta}{16\pi(R+H)^3}} \tag{1.2}$$

for the *p*-polarization, and

$$\alpha_{\text{eff,s}} = \frac{\alpha(1+\beta)}{1 - \frac{\alpha\beta}{32\pi(R+H)^3}} \tag{1.3}$$

for the *s*-polarization.

The scattering cross-section - proportional to the effective polarizability - is therefore higher with a *p*-polarization of the electric field than with a *s*-polarization. This enhancement along the tip direction normal to the sample is even more pronounced when considering the longitudinal shape of the tip, as can be done using the finite dipole model [61]. While the point dipole model gives a qualitative understanding of the tip-sample interactions, the finite dipole model has been shown to give a better quantitative understanding of the tip-sample interactions, allowing more quantitative analysis of material properties at the nanoscale [61–63]. A detailed description of the finite dipole model can be found in Ref. [60].

1.1.3 Non-interferometric detection of the near field

In a s-SNOM system, the generally weak near-field signal is hidden in a large background coming from the diffraction-limited spot directly back-scattered from the sample. To detect the near field, s-SNOMs exploit the modulation of the AFM tip in the intermittent contact mode. This modulation scheme is introduced in details in this section. Its advantages and limits are presented, and the necessity to use additional detection schemes to recover the near field are discussed.

In the simplest version of a s-SNOM setup, the discrimination between the near field and the background field is done by modulation of the tip height and demodulation of the signal by a lock-in amplifier on the detection side [7]. The tip oscillation amplitude h is typically of the order of a few tens of nanometers [36, 58, 64–66]. The movement of the tip apex can be approximated as a harmonic oscillator [7, 67] and the tip-sample distance H can thus be described as

$$H(t) = h(1 + \cos(\Omega t)) \tag{1.4}$$

with Ω the tip oscillation (or tapping) frequency. Over the distance h, the variations of the background field E_{B} are very little compared to the near field E_{NF} which presents an exponential-like decay. Since higher harmonics correspond to the faster-varying field contributions, the near-field signal can be isolated using lock-in detection at higher orders of the tapping frequency. In the following, an expression for the modulated intensity of the detected light is derived. The derivation is mainly based on the work from Ocelic et al. [14], the thesis from N. Ocelic [60] and some considerations in the review from J. M. Atkin [7]. Additional considerations on a specific expression for the background and on background artefacts can be found in Ref. [60].

Figure 1.3 shows the fields involved in the demodulation scheme. The electric field coming onto the PD, E_{S}, is composed of the near field and signal of interest E_{NF} and the far-field background E_{B}:

$$E_{\mathrm{S}} = E_{\mathrm{NF}} + E_{\mathrm{B}}. \tag{1.5}$$

These fields are varying periodically, with a period Ω, due to the periodic tip oscilla-

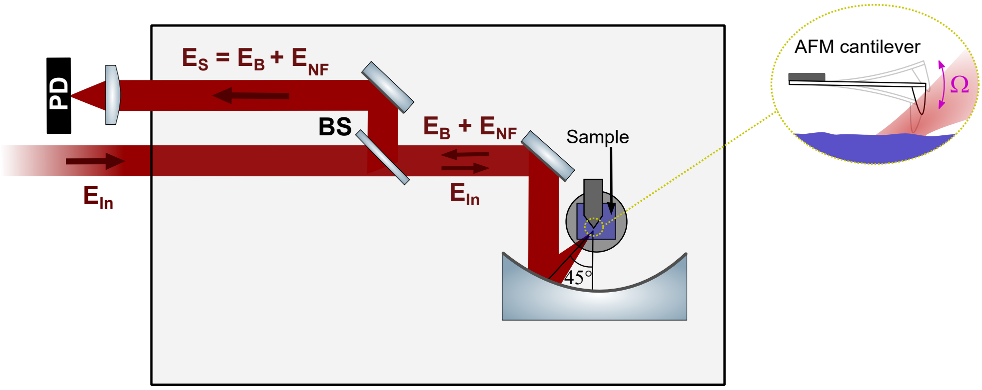

Figure 1.3. Sketch of a s-SNOM setup showing the different field contributions involved in the s-SNOM demodulation. The incident light E_{in} is focused on the AFM tip oscillating at a frequency Ω. Part of the light coming from the near field of the sample E_{NF} and the far-field background light E_{B} is then backscattered and directed by a beam splitter (BS) towards a PD.

tions. Thus, they can be decomposed in the form of Fourier series:

$$E_{\mathrm{S}} = \sum_{n=-\infty}^{n=+\infty} E_{\mathrm{s},n} \exp(in\Omega t), \tag{1.6}$$

$$E_{\mathrm{NF}} = \sum_{n=-\infty}^{n=+\infty} E_{\mathrm{nf},n} \exp(in\Omega t), \tag{1.7}$$

$$E_{\mathrm{B}} = \sum_{n=-\infty}^{n=+\infty} E_{\mathrm{b},n} \exp(in\Omega t), \tag{1.8}$$

where $E_{j,n} = |E_{j,n}|e^{i\phi_{j,n}}$, $j = \{\mathrm{s}, \mathrm{nf}, \mathrm{b}\}$ includes the amplitude and the phase of the fields.

The detector displays the signal in the form of an output voltage proportional to the intensity I_{D} that is collected by the parabolic mirror (see Figure 1.3). This intensity is proportional to the electric field E_{S} such as

$$I_{\mathrm{D}} \propto |E_{\mathrm{S}}|^2 = E_{\mathrm{S}} E_{\mathrm{S}}^*, \tag{1.9}$$

meaning that

$$I_{\mathrm{D}} \propto |E_{\mathrm{NF}}|^2 + |E_{\mathrm{B}}|^2 + E_{\mathrm{NF}} E_{\mathrm{B}}^* + E_{\mathrm{NF}}^* E_{\mathrm{B}}. \tag{1.10}$$

The Fourier components of I_{D} are thus (see Appendix A.1 for more details on the multiplication of the Fourier components):

$$I_{\mathrm{d},n} \propto \sum_k E_{\mathrm{nf},k} E_{\mathrm{nf},k-n}^* + \sum_k E_{\mathrm{b},k} E_{\mathrm{b},k-n}^* + \sum_k E_{\mathrm{nf},k} E_{\mathrm{b},k-n}^* + \sum_k E_{\mathrm{b},k} E_{\mathrm{nf},k-n}^*. \tag{1.11}$$

Considering the relative strengths and variations of the fields [7,13,60], a few assumptions can be made:

1. The background field at the 0^{th} order is dominating compared to the background field at any other order: $|E_{\mathrm{b},0}| \gg |E_{\mathrm{b,n}}|, n \in \mathbb{Z}^*$.
2. The background field at the 0^{th} order is dominating compared to the near field at any order: $|E_{\mathrm{b},0}| \gg |E_{\mathrm{nf},n}|, n \in \mathbb{Z}$. As a consequence: $E_{\mathrm{s},0} = E_{\mathrm{nf},0} + E_{\mathrm{b},0} \approx E_{\mathrm{b},0}$.
3. For an intensity $I_{\mathrm{d},n}, |n| > |n_0|$, the near field at any n^{th} order is dominating compared to the background at the same order: $|E_{\mathrm{b},n}| \ll |E_{\mathrm{nf},n}|, |n| \geq |n_0|$. Usually for the visible $n_0 \sim 3$.

Assumptions 1. and 3. are a direct consequence of the slow variations of the background field. Assumption 2. comes from considerations on the difference between the scattering cross-section of the near field compared to the far field. The signal coming from the near field is indeed restricted to a small (few tens of nanometers) area around the tip apex. By contrast, the signal from the background can come from the whole region illuminated by the diffraction limited incident light, meaning the tip shaft and the sample surface. Assumption 2. is generally true as long as the near field is sufficiently weak.

Assumptions 1. and 2. mean that all the terms that do not contain $|E_{\mathrm{b},0}|$ can be neglected. In addition, with Assumption 3., for $n > n_0$ sufficiently big and taking κ as the proportionality constant, we obtain

$$I_{\mathrm{d},n} \approx \kappa \left(E^*_{\mathrm{b},0} E_{\mathrm{nf},n} + E_{\mathrm{b},0} E^*_{\mathrm{nf},n} \right) . \tag{1.12}$$

Then by expressing the fields as a function of their amplitude and phase, the intensity can finally be written as

$$\boxed{I_{\mathrm{d},n} \approx 2\kappa |E_{\mathrm{b},0}||E_{\mathrm{nf},n}| \cos(\Phi_{\mathrm{nf},n} - \Phi_{\mathrm{b},0})} . \tag{1.13}$$

The spectrum associated with the different intensity orders is given approximately in Figure 1.4a. The near-field information is mainly contained in the higher orders (3Ω and above), but these orders are also having a smaller amplitude than the lower orders. This spectrum is to compare to the spectrum in Figure 1.6, with pseudo-heterodyne detection. Experimentally, the evolution of the intensity $I_{\mathrm{d},n}$ as a function of the tip and illumination to sample distance can be measured. This evolution is presented in Figure 1.4b for the first four orders. The higher orders present the exponential-like decay characteristic of the near field.

The relative near-field amplitude can thus be retrieved by the use of lock-in detection at higher orders of the tapping frequency. However, the background is not completely removed in this case. Instead, a field proportional to the near-field amplitude can be obtained as long as $|E_{\mathrm{b},0}|$ is a constant. If this assumption is true,

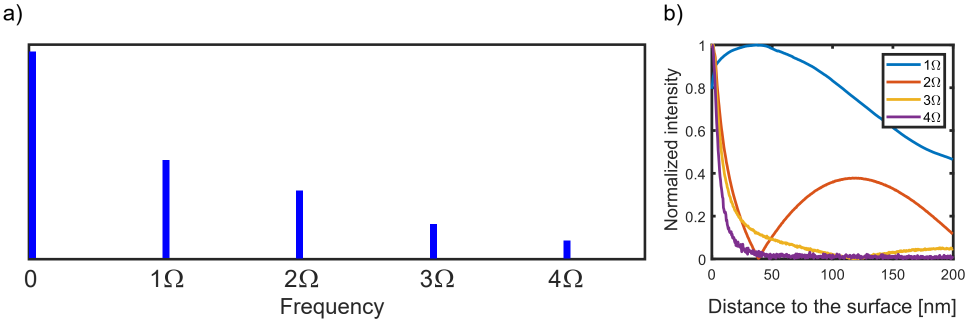

Figure 1.4. The different intensity orders. a) Schematic of the spectrum of the detector output signal, in the case of non-interferometric detection. b) Approach curve measured experimentally with our setup.

the background can be used as an advantage as it can enhance the signal from the near field [13]. However, the phase term $\Phi_{\mathrm{b},0}$ cannot be generally considered as a constant [60], so that the phase information $\Phi_{\mathrm{nf},n}$ is lost in the process. To obtain the phase information and completely exclude the multiplicative background $|E_{\mathrm{b},0}|$, interferometric schemes such as the pseudo-heterodyne detection have to be used.

1.2 Additional detection schemes

Because of the lack of control on the background amplitude $|E_{\mathrm{b},0}|$ and phase $\Phi_{\mathrm{b},0}$, additional detection schemes have been implemented in s-SNOM to remove the background. For example, in a homodyne detection scheme, an additional reference field of same wavelength as the s-SNOM light source is added to the detected signal [7]. This controlled reference field is set to be much stronger than the background field. Thus, it dominates the signal and the uncontrolled terms in Equation 1.13 are replaced with the ones from the known reference field. In contrast, in the heterodyne detection scheme, a reference field beating at a shifted frequency compared to the incident field is added to the detected signal [13]. Lock-in detection at a frequency different than the tapping frequency can thus be used to detect a background-free signal. More recently, PsHet detection [14] has been implemented. This technique combines the advantage of a background-free signal with a setup that is simpler and applicable to a broad spectral range [14]. Furthermore, the interference with a reference field in the case of a broadband light source allows to do nano-Fourier transform spectroscopy (nano-FTS).

In this section, the pseudo-heterodyne detection scheme is presented in details, as well as the basics of the technique allowing to do nano-FTS.

1.2.1 Pseudo-heterodyne detection

In the PsHet detection scheme, a reference field is added using an additional mirror, as sketched in Fig. 1.5. This new signal does not depend on the tip modulation, but since the mirror itself is oscillating, the reference field has a sinusoidal phase modulation. The reference field can be described as [14]

$$E_{\mathrm{R}} = \rho \exp(i\gamma \sin(Mt) + i\Phi_{\mathrm{R}}), \tag{1.14}$$

with ρ and Φ_{R} its amplitude and phase, respectively, M its mirror oscillation frequency and γ its mirror oscillation amplitude. M is taken as much smaller than the tip oscillation frequency Ω. The Fourier decomposition of this reference field gives [14]

$$E_{\mathrm{R}} = \sum_{m=-\infty}^{m=+\infty} E_{\mathrm{r},m} \exp(imMt) \quad \text{with} \quad E_{\mathrm{r},m} = \rho J_m(\gamma) \exp(i\Phi_{\mathrm{R}} + im\pi/2) \tag{1.15}$$

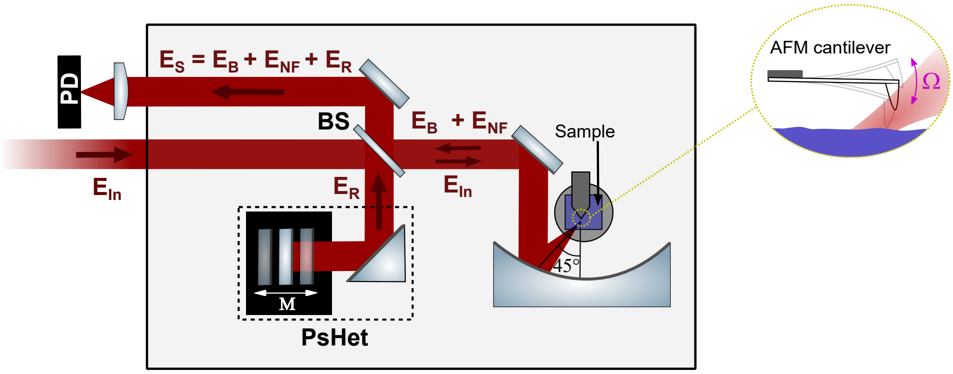

Figure 1.5. Sketch of a s-SNOM setup with pseudoheterodyne detection, showing the different field contributions. The beam path corresponds to the one from the setup used in this thesis. Compared to Figure 1.3, a reference mirror oscillating at a frequency $M \ll \Omega$ has been added. This mirror provides the field contribution E_R.

where J_m is the Bessel function of the first kind and m^th order. We thus now have a total frequency:

$$E_\mathrm{S}^\mathrm{PH} = E_\mathrm{NF} + E_\mathrm{B} + E_\mathrm{R} \tag{1.16}$$

The total intensity sent to the detector $I_\mathrm{D} \propto E_\mathrm{S}^\mathrm{PH} E_\mathrm{S}^\mathrm{PH*}$ thus contains 6 additional components due to the interference with the reference field. However, E_R is independent from the modulation at frequency Ω and is thus suppressed by demodulation at $n\Omega$, for $n \neq 0$. Assumption 1. and 3. mentioned in section 1.1.3 are also still valid, so that the terms $|E_\mathrm{R}|^2$ and $|E_\mathrm{B}|^2$ and $E_\mathrm{B}E_\mathrm{R}^* + E_\mathrm{B}^*E_\mathrm{R}$ can be discarded due to the demodulation at $n\Omega$, and I_D can be expressed as

$$I_D \propto |E_\mathrm{NF}|^2 + E_\mathrm{NF}E_\mathrm{R}^* + E_\mathrm{NF}^*E_\mathrm{R} + E_\mathrm{NF}E_\mathrm{B}^* + E_\mathrm{NF}^*E_\mathrm{B}. \tag{1.17}$$

Second, the near field and background field are independent from the reference mirror oscillations, so that demodulation at the frequency $n\Omega + mM$, with $n, m \in \mathbb{Z}^*$, discards the terms $|E_\mathrm{NF}|^2$ and $E_\mathrm{NF}E_\mathrm{B}^* + E_\mathrm{NF}^*E_\mathrm{B}$. The equation thus finally becomes

$$I_D \propto E_\mathrm{NF}E_\mathrm{R}^* + E_\mathrm{NF}^*E_\mathrm{R}. \tag{1.18}$$

As the mirror oscillation frequency M is much lower than the tip oscillation frequency Ω, the decomposition of I_D in its n Fourier components can be carried out first. The intensity Fourier series component at the n^th order thus have the form:

$$I_{d,n} \propto E_{\mathrm{nf},n}E_\mathrm{R}^* + E_{\mathrm{nf},n}^*E_\mathrm{R} \tag{1.19}$$

After decomposing the reference field E_R into its m Fourier components, the expression of the intensity becomes

$$I_{d,n} \propto 2|E_{\mathrm{nf},n}| \sum_m |E_{r,m}| \cos(mMt + \Phi_{\mathrm{r},m} - \Phi_{\mathrm{nf},n}), \tag{1.20}$$

where $\Phi_{\mathrm{r},m} = \Phi_{\mathrm{R}} + m\pi/2$. Thus, as long as the reference modulation M is lower than the tip vibration frequency Ω, each of the scattered signal harmonics with frequency $n\Omega$ splits into sidebands with frequency $f_{n,m} = n\Omega + mM$. Figure 1.6 presents a schematic view of the corresponding spectrum.

At the frequency $f_{n,m}$ and taking κ' as the proportionality constant, the intensity Fourier component $I_{n,m}$ have the form:

$$I_{n,m} = 2\kappa' |E_{\mathrm{nf},n}| \rho J_m(\gamma) \cos(\Phi_{\mathrm{R}} + m\pi/2 - \Phi_{\mathrm{nf},n}) \tag{1.21}$$

This equation gives rise to two cases. For m even, the Fourier components of the intensity $I_{n,m}$ are proportional to a cosine. For m odd, the Fourier components of $I_{n,m}$ are proportional to a sine. This means that by adding the odd and even terms divided by their respective Bessel term $J_m(\gamma)$, the near field $E_{\mathrm{nf},n}$ can be reconstructed.

In the particular case where $m = 1$ for the imaginary part and $m = 2$ for the real part, and using the suitable choice $\gamma = 2.63$ so that $J_1(\gamma) = J_2(\gamma) \approx 1/2.16$, the expression can be further simplified as

$$E_{\mathrm{nf},n} = 2.16C\,[I_{n,2} + iI_{n,1}] \text{ with } C = \frac{\exp(i\Phi_{\mathrm{R}})}{2\kappa'\rho}. \tag{1.22}$$

The near-field amplitude and phase can thus be retrieved using the relations

$$|E^{\mathrm{exp}}_{\mathrm{nf},n}| = 2.16|C|\sqrt{I^2_{n,2} + I^2_{n,1}} \tag{1.23}$$

$$\Phi^{\mathrm{exp}}_{\mathrm{nf},n} + \Phi^{\mathrm{exp}}_{\mathrm{R}} = \arctan\left(\frac{I_{n,1}}{I_{n,2}}\right) \tag{1.24}$$

A back-check of these formula are given in appendix. It should be noted that the near-field phase can only be reconstructed up to the additive constant Φ_{R}.

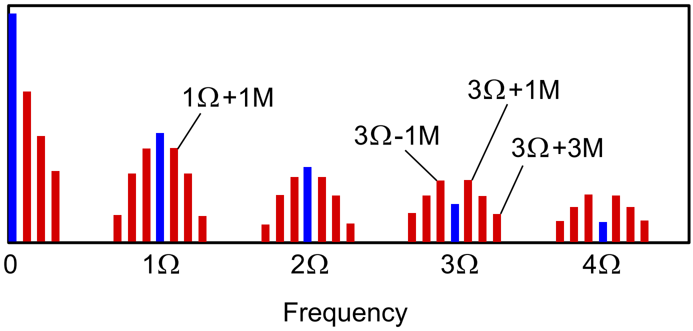

Figure 1.6. Schematic of the spectrum of the detector output signal, in the case of PsHet detection. The relative heights between the peaks do not aim to accurately describe the experimental ones. Figure inspired from [14].

As mentioned previously, this relation can be used at the condition of adjusting the mirror oscillation amplitude γ such that $J_1(\gamma) = J_2(\gamma)$, meaning $\gamma = 2.63$. Experimentally, this phase modulation amplitude corresponds to a mirror length modulation amplitude of [7]

$$\Delta l = \gamma\lambda/(2.2\pi) \approx 0.21\lambda, \tag{1.25}$$

with λ the wavelength of the incident light. This means that the the PsHet scheme should be adjusted to the excitation wavelength.

1.2.2 Fourier-transform spectroscopy

Fourier-transform infrared (FTIR) spectroscopy is a well-established interferometric method [68] to obtain the spectrum of a sample under study. More recently, this method has been combined with nanoimaging [15, 69] to do hyperspectral imaging at the nanometer-scale [70]. This method is referred to as nano-FTIR spectroscopy. As the acronyms suggests, this method is widely used to obtain infrared spectra. However, it is applicable to other spectral ranges as well and is more generally referred as Fourier-transform spectroscopy (FTS) in this thesis. In this section, the basic principles of FTS and nano-FTS are explained. The concepts are based on the book *Fourier Transform Infrared Spectrometry* from P.R. Griffiths and J.A. de Haseth [68] and the PhD thesis of F. Huth [71].

The main principles and setup of FTS can be explained using a conventional Michelson interferometer, as sketched in Figure 1.7a. In a Michelson setup, a beam is separated by a 50/50 BS in two arms directed towards a fixed mirror (at a distance D from the BS) and a reference mirror (at a variable distance D+d from the BS).

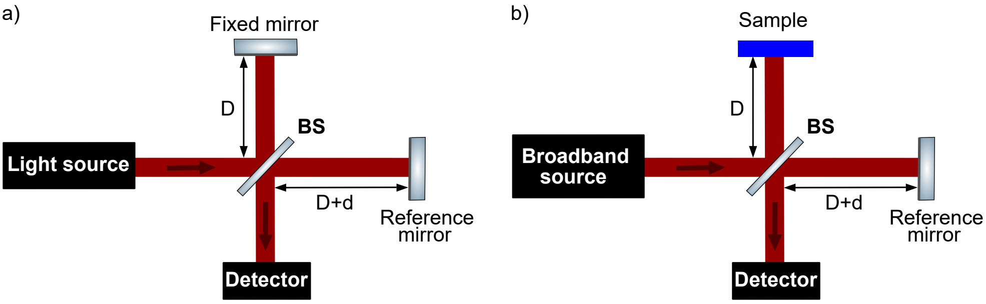

Figure 1.7. Principles of FTS. a) Sketch of a conventional Michelson interferometer. The beam coming from the light source is separated by a BS in two arms directed respectively towards a fixed mirror and a reference mirror that can be moved. The beams reflected from these two mirrors then recombine at the detector. b) Setup in the case of FTS in reflection. The fixed mirror is replaced with the sample to be analyzed, and the light source is a broadband source.

The light reflected from the two mirrors recombine at the BS, leading to a detected intensity that in the case of a single wavelength source takes the form [68]

$$I(d, \lambda) = 0.5 I_0(\lambda)(1 + \cos(2\pi d/\lambda)) \tag{1.26}$$

where I_0 is the intensity of the incident light and λ is the wavelength of the light source. Moving the position of the reference mirror thus induces sinusoidal oscillations at the detector. The period of these sinusoidal oscillations gives information about the wavelength λ. The recording of the intensity of the light as a function of the reference mirror distance d is called an interferogram.

In the case of FTS in reflection, the light source is a broadband source, and the fixed mirror is replaced with a sample. Contrary to the fixed mirror, the sample can absorb, transmit and/or reflect parts of the spectrum of the broadband source.

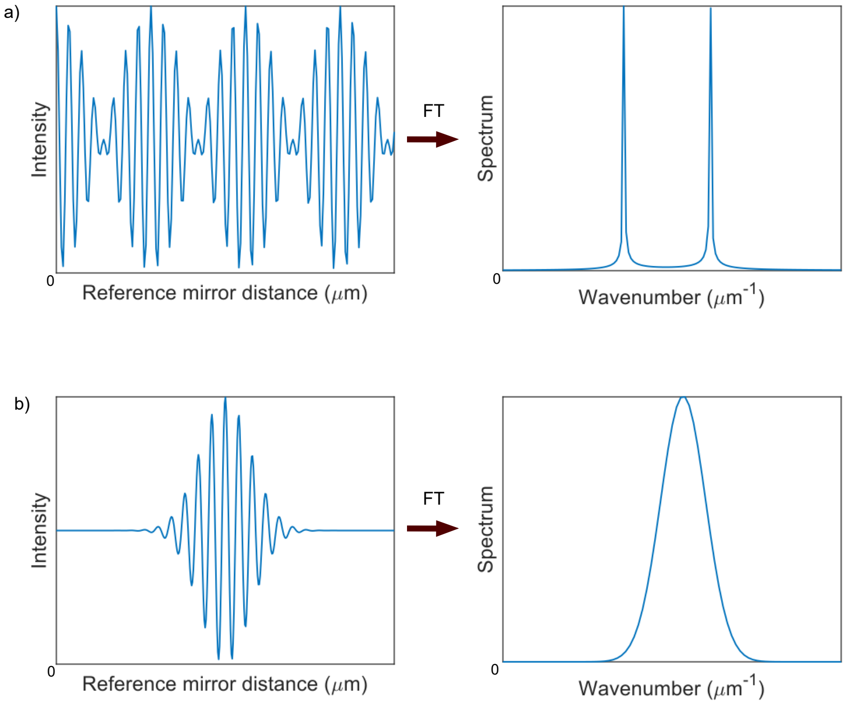

Figure 1.8. Examples of interferograms and spectra . a) Interferogram and its Fourier transform in the case of 2 wavelengths components. b) Interferogram and its Fourier transform in the case of a broadband source.

The advantage of the broadband source is that it probes all the wavelength components at the same time. However, the interferogram is also more complex and the intensity contribution of each wavelength cannot be extracted directly. To get the wavelength contribution, a Fourier transform (FT) has to be applied. As shown for clarity in Figure 1.8a in the case of two wavelengths, the FT converts the interferogram into the relative intensity of its wavelengths components, namely the spectrum. The same process happens in the case of a broadband source having a continuum of wavelength contributions, as shown in Figure 1.8b.

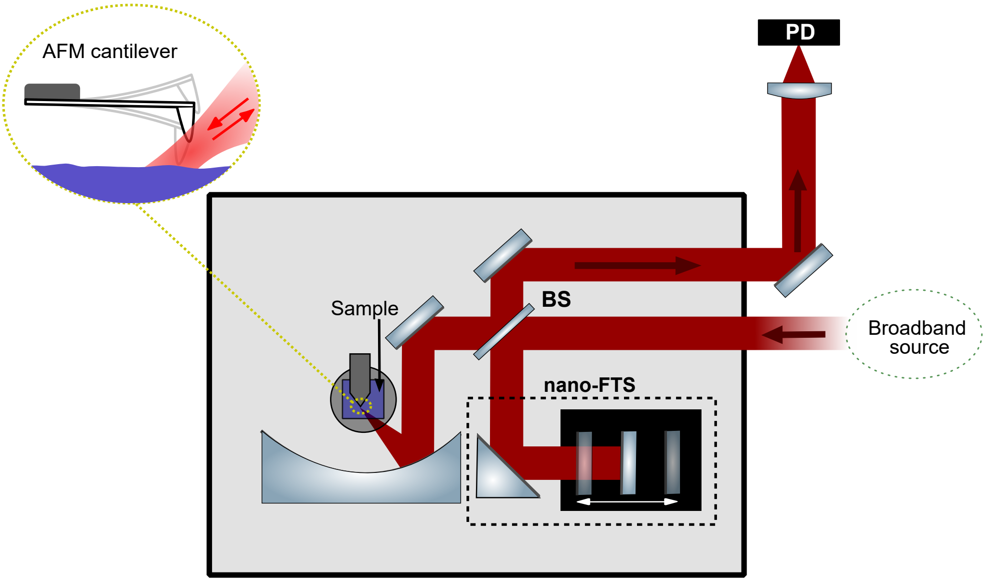

Figure 1.9. Sketch of a s-SNOM setup for Fourier-transform spectroscopy. The beam path corresponds to the one from the setup used in this thesis. As for the case of conventional FTS, the beam from a broadband source is separated in two arms directed towards a reference mirror and the sample, respectively. The beams reflected from the reference mirror and scattered from the tip and sample then recombine at the BS and are directed towards a PD.

In the case of a near-field setup, the aforementioned principles remain the same. Figure 1.9 shows the setup in the case of nano-FTS. The sample, which is in this case under the AFM tip, is illuminated by a broadband source. The light scattered from the tip and the sample is then recombined with the light reflected from the moving reference mirror at the BS. The interference of these two beams is detected at the PD.

In the case of nano-FTS spectroscopy, the background is not completely suppressed. Indeed, following the same arguments as in Sections 1.1.3 and 1.2.1, the total signal at the detector can be described as [71]

$$I_{\mathrm{d},n} \approx 2\kappa|E_{\mathrm{b},0}||E_{\mathrm{nf},n}|\cos(\Phi_{\mathrm{nf},n} - \Phi_{\mathrm{b},0}) + 2\kappa|E_{\mathrm{Ref}}||E_{\mathrm{nf},n}|\cos(\Phi_{\mathrm{nf},n} - \Phi_{\mathrm{Ref}}), \quad (1.27)$$

where $|E_{\mathrm{Ref}}|$ and Φ_{Ref} are in this case the amplitude and phase of the nano-FTS reference mirror. Typically, $|E_{\mathrm{B}}| \ll |E_{\mathrm{Ref}}|$. Thus, it can usually be discarded from the total signal.

1.3 Experimental setup

Figure 1.10 shows a sketch of the setup used in this thesis. All the optics inside the neaSNOM box has been purchased from Neaspec GmbH (now Attocube systems AG). For simplification, the deflection laser and other components associated with the AFM feedback loop and the s-SNOM lock-in detection are not represented. In our setup, the deflection laser has a wavelength of 790 ± 10 nm. The beam path of the sources used for the tip illumination can be changed with the help of flip mirrors (mirrors with rounded arrows around them). The incident light from a continuous wave or pulsed laser can therewith be directed either towards the right or left entrance of the s-SNOM. In both cases, light is then separated in two beams by a 50/50 BS. Half of it is focused downwards by a parabolic mirror (NA=0.37) onto an AFM tip oscillating in intermittent contact mode while scanning the sample. The tip used is a commercially available platinum-coated silicon tip (ARROW-NCPt from Nanoworld). It is oscillating at about 250-300 kHz and usually with a peak-to-peak amplitude of 50-70 nm. The light is then scattered in all directions. A small part of it is reaching the parabolic mirror and directed by reflection at the BS towards a one pixel PD (2051/2053 from Newport).

When using a continuous wave laser, the PsHet module (mirrors on the left side of the neaSNOM) with a reference mirror oscillating at a frequency of 300 MHz and with an amplitude of about 21% of the laser wavelength can be used. As seen in section 1.2.1, PsHet detection allows to strongly suppress the background coming from direct scattering from the sample, and retrieve the amplitude and phase of the signal.

When using a broadband laser, the nano-FTS module (mirrors on the right side of the neaSNOM) can be used. In such case, the reference mirror is swept through the coherence range of the laser. Using the nano-FTS allows to recreate the spectrum of the sample under study. However, as has been seen in section 1.2.2, the background is not completely suppressed.

At the beginning of this PhD work, the setup was consisting of the neaSNOM with the nano-FTS module and the permanently available illumination sources were a helium-neon (HeNe) laser and a green laser diode (522 nm). Since the nano-FTS module is optimized for broadband spectroscopy, it couldn't be used with continuous wave sources so the measurements were mostly done using the simplest form of s-SNOM as presented in section 1.1.3. During the project, a PsHet module has been installed, as well as two femtosecond lasers (pulse width of about 10 and 100 fs) in the wavelength range of 800 nm, enabling a proper use of the nano-FTS and PsHet modules. Furthermore, the setup has been built such that new lasers or other optical components could be quickly added to the beam path. Additional elements such as a tunable near-infrared laser, polarizers and half-wave plates have thus been used when

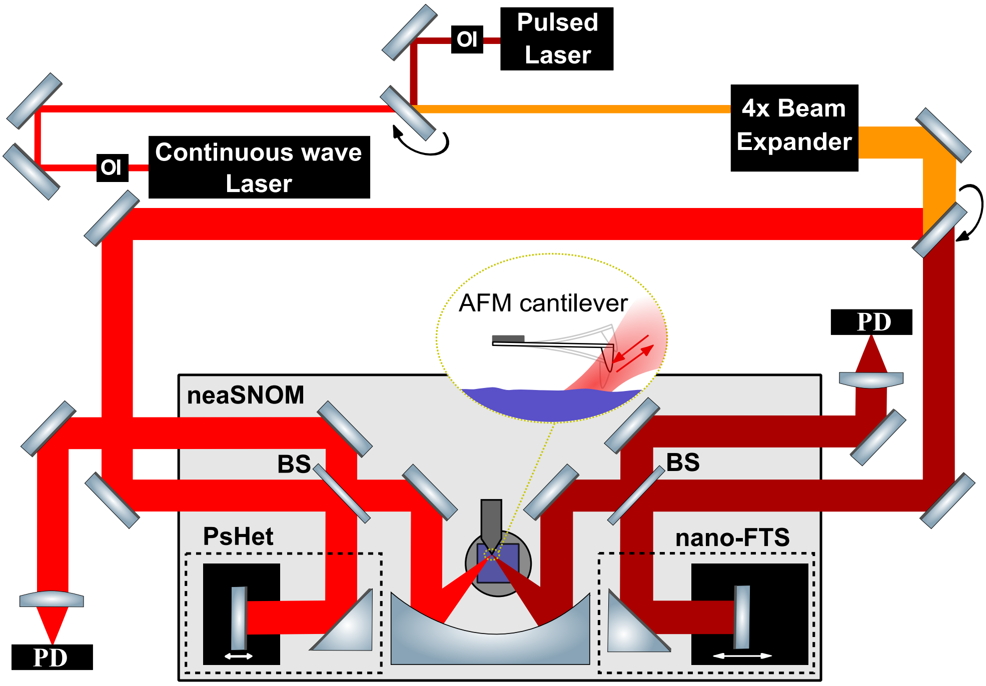

Figure 1.10. Experimental setup. The red beams represent the continuous wave laser path, the brown beams the broadband laser path, and orange the paths where both always travel through. The eventual back-reflections reaching the laser are stopped by optical isolators (OI). Flip mirrors bring the incident laser either towards the left or right side of the neaSNOM. The laser beam is focused by a parabolic mirror on the oscillating tip of the AFM cantilever. The light that is backscattered in the same direction as the beam path is then recollected and directed towards a photodiode. Depending on the type of laser, either the PsHet or the nanoFTIR can be used to help the signal detection.

needed. The presence of such an element is mentioned in the thesis when applicable. More information about the laser sources and detectors can be found in Appendix B.

CHAPTER 2

Optical properties of metals

Metals have been used for centuries, either by making use of their mechanical properties to make weapons and armors, high reflectivity to make mirrors and jewelry, or more recently electronic transport properties to make modern electronics.

In this chapter, the basic optical properties of metals are described, with a focus on gold properties. The Drude model and the deviations from this model due to interband transitions are explained, and the fundamental properties of wave traveling at their surface - the SPPs - are presented. This chapter is based on the books *Optical Properties of Solids* from M. Fox [72] and *Plasmonics, Fundamentals and Applications* from S.A. Maier [18].

2.1 The Drude model

Metals are characterized by having one or several of their most energetic electrons - the free electrons - per atom that can move in the crystal lattice. In the Drude model, the movement of these free electrons is considered as a gas of particles moving in a medium with positive ions. Their movement is damped through collisions occurring at a characteristic time τ, leading to a damping of the electrons' movement $\gamma = 1/\tau$. Applying Newton's second law to an electron of mass m_e, of position $\mathbf{x}(\mathrm{t})$ and driven by an electric field $\mathbf{E}$ leads to the equation

$$m_e \frac{d^2\mathbf{x}}{dt^2} + m_e \gamma \frac{d\mathbf{x}}{dt} = -e\mathbf{E}, \tag{2.1}$$

where e the elementary charge of a single electron.

Furthermore, the driving electric field can be expressed as $\mathbf{E}(t) = E_0 e^{-i\omega t}$. Assuming that the electron has the same harmonic time dependence and calculating the dielectric displacement $\mathbf{D}$ for a number of electrons per unit volume N gives the equation

$$\mathbf{D} = \varepsilon_0 \varepsilon_{\mathrm{d}}(\omega)\mathbf{E} = \varepsilon_0 \left(1 - \frac{\omega_p^2}{\omega^2 + i\gamma\omega}\right)\mathbf{E}, \text{ with } \omega_{\mathrm{p}} = \sqrt{\frac{Ne^2}{\varepsilon_0 m_e}} \tag{2.2}$$

where ε_0 is the electric permittivity in vacuum. Thus, the expression of the dielectric function as described by the Drude model is [18, 72]

$$\varepsilon_{\mathrm{d}}(\omega) = 1 - \frac{\omega_{\mathrm{p}}^2}{\omega^2 + i\gamma\omega}. \tag{2.3}$$

Figure 2.1a presents the real and imaginary part of dielectric function for a Drude metal of plasma frequency $\omega_{\mathrm{p}} = 1.37\ 10^{16}$ Hz and damping $\gamma = 1.05\ 10^{14}$ Hz , as described by the Drude model. In the Drude model, the real part is negative - $\mathrm{Re}(\varepsilon_{\mathrm{d}}) = -20$ for a wavelength 633 nm - and until reaching the plasma frequency ω_{p}, for which it becomes zero. It then continues to increase, taking positive values. The imaginary part is positive at low frequencies and decreases towards zero at high frequencies. For a wavelength of 633 nm, $\mathrm{Im}(\varepsilon_{\mathrm{d}}) = 0.7$.

The reflectivity R of metals can then be calculated using the relation [72]

$$R = \left| \frac{\sqrt{\varepsilon_{\mathrm{d}}} - 1}{\sqrt{\varepsilon_{\mathrm{d}}} + 1} \right|^2 . \tag{2.4}$$

Figure 2.1b shows the reflectivity of a typical Drude metal as a function of the frequency normalized to ω_{p}. For frequencies below ω_{p}, the reflectivity is equal to 1, while for frequencies above ω_{p}, the reflectivity drops to zero. Thus, the Drude model explains the high reflectivity of metals at low energies such as the microwave or infrared regime, and the transparency of metals in the ultraviolet range [72]. The transition from high to low reflectivity is sharp when the damping are neglected. The addition of damping γ slightly reduces the reflectivity close to ω_{p} and makes the transition smoother, while keeping the general shape.

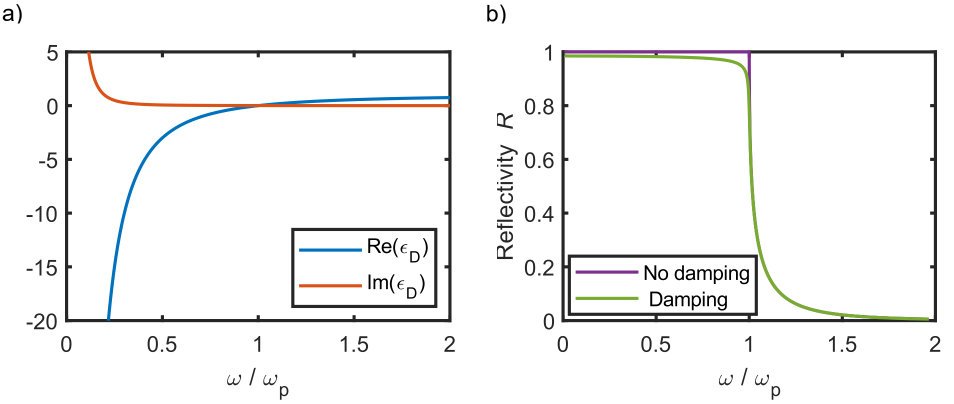

Figure 2.1. Metal in the Drude model. a) Real and imaginary part of the dielectric function as a function of the angular frequency normalized to the plasma frequency, with plasma frequency $\omega_{\mathrm{p}} = 1.37\ 10^{16}$ Hz and damping $\gamma = 1.05\ 10^{14}$ Hz. b) Reflectivity of the same metal as a function of the normalized angular frequency, without and with damping.

However, the Drude model fails to accurately represent the optical properties of metals in the case of metals such as gold or copper. The reasons for the discrepancies between this model and the experiments are presented in the next section.

2.2 Refractive index of gold

When comparing real metals such as gold with their Drude model, some extensive discrepancies can be seen. Figure 2.2 present the comparison between real and imaginary part of the dielectric function of a Drude metal of same plasma frequency and damping as gold (ε_{D}) and as measured by the Johnson and Christy [73] ($\varepsilon_{J\&C}$). Compared to the Drude model, $\mathrm{Re}(\varepsilon_{J\&C})$ reached values close to zero for lower frequencies than ω_{p} and $\mathrm{Im}(\varepsilon_{J\&C})$ doesn't asymptotically decays to zero. The difference is significant in the visible range, where for example at a wavelength of 633 nm, $\mathrm{Re}(\varepsilon_{J\&C})$ = -11.8 instead of -20 and $\mathrm{Im}(\varepsilon_{J\&C}) = 1.25$ instead of 0.7.

The reason for these discrepancies are the interbands transitions in gold [72, 74]. Electrons can indeed be excited from occupied to unoccupied states of the gold electronic band structure, leading to absorption that is not taken into account in the Drude model. In the case of gold, the electrons lying in the $5d$ band states can be excited to the $6sp$ states [74].

These additional transitions can be taken into account by using the Drude-Lorentz model [75], which adds Lorentzian resonances to the dielectric function. However, this model does not follow very well experimental values of the gold dielectric function in the visible range [75]. Therefore, in this thesis, we take the values measured in previous studies [73, 76, 77] as reference for our experiments.

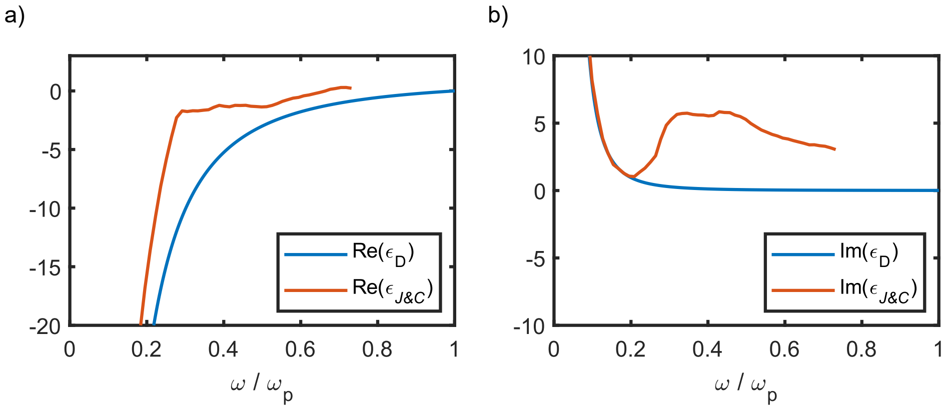

Figure 2.2. Comparison between the dielectric functions of a Drude metal of plasma frequency $\omega_{\mathrm{p}} = 1.37\ 10^{16}$ Hz and of damping $\gamma = 1.05\ 10^{14}$ Hz (ε_{D}) and gold ($\varepsilon_{J\&C}$). a) Real part of the dielectric function as a function of $\omega/\omega_{\mathrm{p}}$. b) Imaginary part of the dielectric function as a function of $\omega/\omega_{\mathrm{p}}$.

2.3 Surface plasmon polaritons

SPPs are collective oscillations of the electronic cloud traveling at the interface between two materials. In the simplest geometry, the interface is a dielectric material of dielectric function ε_d and a metal of dielectric function ε_m, as sketched in Figure 2.3. In this geometry, the SPPs are *p*-polarized, meaning that their electric field vector is in a plane normal to the interface. They are bound to the interface, meaning that their field exponentially decays in the z-direction (direction normal to the interface, see Figure 2.3), but they can propagate in the (x,y)-directions. As such, they qualify as evanescent fields in the z-direction.

The condition for the existence of SPPs in the case of a single interface can be deduced from the boundary conditions and Maxwell's equations, and can be expressed as [18, 72]

$$\frac{k_z^d}{k_z^m} = -\frac{\varepsilon_\mathrm{d}}{\varepsilon_\mathrm{m}}, \tag{2.5}$$

where $k_z^d > 0$ and $k_z^m > 0$ are the components of the wavevector normal to the interface for the dielectric material and the metal, respectively. Equation 2.5 highlights that the dielectric constants ε_d and ε_m must have opposite sign for the SPPs to exist.

The dispersion relation of the SPPs can be expressed as [18, 72]

$$q = \frac{\omega}{c}\sqrt{\frac{\varepsilon_\mathrm{m}\varepsilon_\mathrm{d}}{\varepsilon_\mathrm{m}+\varepsilon_\mathrm{d}}}, \tag{2.6}$$

where q is the in-plane wavevector (i.e. wavevector parallel the the dielectric/metal interface) and c is the speed of light in vacuum. Thus, the SPPs are able to propagate in the region where the real part of ε_m, $\mathrm{Re}(\varepsilon_\mathrm{m})$, is negative and $\varepsilon_\mathrm{m} + \varepsilon_\mathrm{d} < 0$.

The wavelength of SPPs is then expressed as

$$\lambda_\mathrm{SPP} = \frac{2\pi}{\mathrm{Re}\{q\}}, \tag{2.7}$$

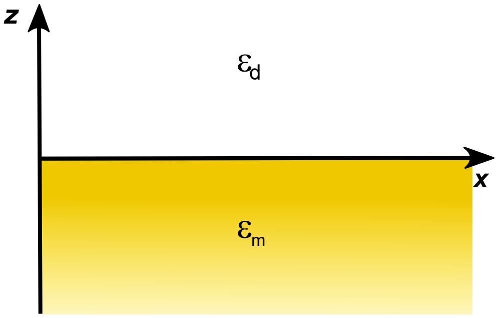

Figure 2.3. Simplest geometry for the propagation of SPPs at the interface between a metal of dielectric function ε_m and a dielectric of dielectric function ε_d.

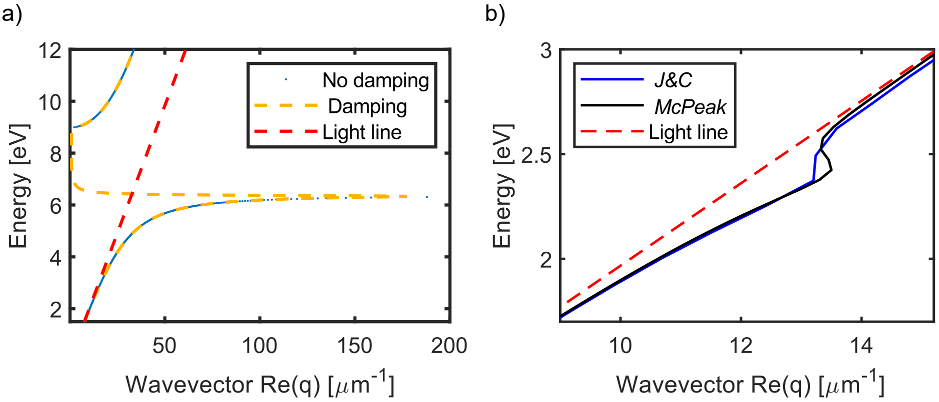

Figure 2.4. Dispersion relation of SPPs. a) SPP propagating at the interface between a Drude metal of plasmon frequency $\omega_\mathrm{p} = 1.37\ 10^{16}$ Hz and air, without damping and with a damping of $\gamma = 1.05\ 10^{14}$ Hz. b) SPP propagating at the interface between gold and air. The data for the gold dielectric function is taken from Johnson and Christy (*J&C*) [73] and McPeak et al. (*McPeak*) [77].

and the propagation length for the SPP intensity is

$$L_\mathrm{p}^\mathrm{SPP} = \frac{1}{2\,\mathrm{Im}\{q\}}. \tag{2.8}$$

Figure 2.4a displays the dispersion relation of SPPs traveling at the interface between air and a generic metal following the Drude model, with $\omega_\mathrm{p} = 1.37\ 10^{16}$ Hz and $\gamma = 1.05\ 10^{14}$ Hz. As SPPs are bound to the surface, their energy range corresponds to the portion of the curve lying to the right of the light line, defined as the dispersion relation in free space. As light propagation in air follows the light line, SPPs cannot be excited directly by plane waves (PWs). Specific techniques using prisms, gratings, or sharp probes must be used to bridge the wavevector gap between the light line and the dispersion relation of the SPPs. For the same reason, SPPs cannot be directly imaged with a conventional microscope. It is however possible to directly map the SPPs using the subwavelength resolution and the sharp tip of the s-SNOM.

In a lossless metal, the wavevector q of the SPPs tends towards infinity, for the surface plasmon frequency $\omega_\mathrm{sp} = \omega_\mathrm{p}/(\varepsilon_\mathrm{d} + 1)$. It would imply that at this frequency, the wavelength λ_SPP and the group velocity of the SPPs tend to zero. Metals are however lossy, which limits q to a finite value, as can be seen in the case of damping in Figure 2.4a in the case with damping.

Figure 2.4b shows the comparison between the dispersion relation of SPPs on gold, based on the values of the gold dielectric function measured by Johnson and Christy [73] and the ones measured by McPeak et al. [77]. McPeak et al. use template stripping with an improved recipe to obtain very smooth gold surfaces [77]. In the case of gold, the losses due to the interband transitions are particularly important compared to what can be seen for silver, for example. The confinement of the SPPs is therefore not as strong as on silver but the chemical stability of gold makes it an interesting platform for long-terms studies.

The dispersion relations plotted in Figure 2.4b are different depending on the experimental values for the SPPs. Notably, it seems that the plasmonic properties are slightly better for the values of McPeak et al. around 2-2.5 eV, probably due to their improved recipe. These values could thus be compared to the values obtained by direct measurement of SPPs on monocrystalline gold, as is shown in the next chapter.

CHAPTER 3

Characterization of surface plasmon polaritons (SPPs)

Near-field characterization of surface waves has been realized for a wide range of polaritons across the optical spectrum, from plasmons in graphene in the mid-infrared [49] to excitonic waveguides [51] in the visible range. Many of these works used a s-SNOM in a reflection configuration such as ours. In this configuration, interference patterns due to SPPs excited through several excitation channels on an air/gold interface have been studied [35,36], and a method was found to isolate the SPPs launched by the tip - i.e. the tip-launched SPPs - and to extract their wavelength in the visible range [36]. Yet, the full characterization of both wavelength and the propagation length of SPPs at in the visible range were not achieved with a s-SNOM in reflection before our work. The characterization of SPPs for this interface is nevertheless relevant, as the many tabulated values of the dielectric functions available in the literature [73, 76, 77] predict different wavelengths and propagation lengths of the SPPs. It is thus important to experimentally determine the value of the complex wavevector of our gold platelets before studying its coupling with other materials in a quantitative way. The synthesis of monocrystalline gold platelets [29, 31, 78], having a very low surface roughness, provides an opportunity to do so.

In this chapter, the different excitation channels for the SPPs are explained and a method to isolate the pure tip-launched SPPs is demonstrated. The tip-launched SPPs should indeed be easier to characterize fully, as the incident laser beam is always following the tip, and the characterization of the other types of SPPs involves the precise knowledge of the incident angles [35, 79]. Furthermore, an expression for the amplitude and the phase of the near-field signal is derived. With these expressions the wavelength and propagation length of the SPPs are retrieved for an excitation wavelength of 633 nm. This chapter is based on our study "Quantitative near-field characterization of surface plasmon polaritons on monocrystalline gold platelets", published in *Optics Express* [66].

3.1 The different excitation channels of SPPs

As mentioned in Section 2.3, the dispersion relation of the SPPs propagating at the interface between gold and air is close to the light line compared to SPPs at the air/silver interface [18] or in graphene [47, 49, 80], for example. The SPPs can thus be excited at the tip, but also at the edges of the gold platelets. The different ways to excite SPPs on gold are presented here.

3.1.1 Tip-launched SPPs

The tip-launched SPPs are defined as the SPPs excited directly by the tip. Thus, in a s-SNOM measurement in reflection, at each position of the scan, a tip-launched SPP wave is launched by the tip, propagates towards the edge of the gold platelet, is reflected at the edge, propagates back towards the tip, and finally is scattered by the tip towards the detector. These processes are labeled as 1 to 4 in Figure 3.1a.

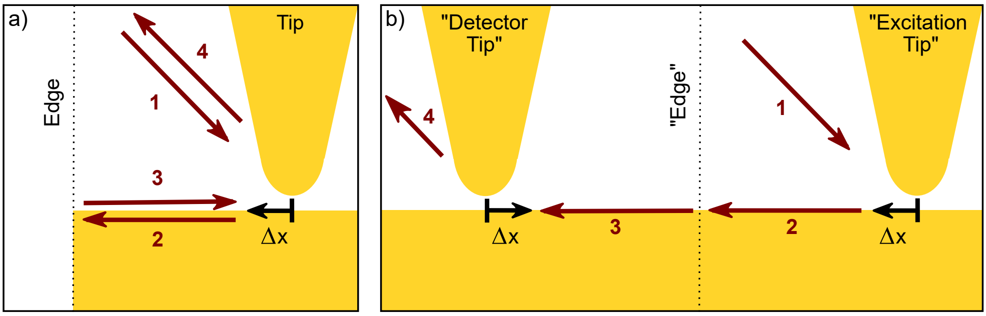

Figure 3.1. Tip-launched SPPs. a) Sketch of the tip-launched SPP path, indicated by the red arrows. The black arrow represents the movement of the tip from one position to another, Δx. b) Equivalent path in which the "excitation" and "detection" functions of the tip have been separated. The former position of the edge is highlighted by the dotted line. From one measurement point to the other, the "excitation tip" and "detector tip" move towards each other by a total distance $2\Delta x$.

In the measurements of tip-launched SPPs, the tip is at the same time acting as the emitter of the tip-launched plasmons and as the receiver. The distance the SPP has traveled is thus at all point of the scan twice the distance that is recorded in the measurement [49]. The tip-launched SPPs can thus be measured as long as their propagation length is larger than two times the distance between the tip and the edge, supposing no additional losses due to the reflection at the edge. Furthermore, each step Δx from one position of the tip to another corresponds to a reduction of the distance traveled by the tip-launched SPPs of $2\Delta x$, as highlighted by Figure 3.1b.

Therefore, two sets of coordinates are needed when talking about the tip-launched SPPs in our s-SNOM measurements:

- A coordinate system corresponding to the coordinates of the near-field maps, (x, y, z). It is associated with a field from the tip-launched plasmons of the form

$$E_{\mathrm{tl}} = \frac{A}{\sqrt{x}} e^{-\Gamma_{\mathrm{tl}} x} e^{i(K_{\mathrm{tl}} x - \phi_{\mathrm{p}})}. \tag{3.1}$$

- A coordinate system corresponding to the hypothetical situation where the receiving part is fixed and only the tip is moving, (x', y', z'). It is associated with a SPP field of the form

$$E_{\mathrm{SPP}} = \frac{A}{\sqrt{x'}} e^{-\Gamma_{\mathrm{SPP}} x'} e^{i(K_{\mathrm{SPP}} x' - \phi_{\mathrm{p}})}. \tag{3.2}$$

  This second set of coordinates corresponds to the distance that the SPPs have really traveled.

The two coordinates are related through the transformation $x' = 2x$, for all position coordinates x' and x.

The relationship between the characteristic constants is thus:

$$K_{\mathrm{tl}} = 2K_{\mathrm{SPP}} \quad \text{and} \quad \Gamma_{\mathrm{tl}} = 2\Gamma_{\mathrm{SPP}} \tag{3.3}$$

Defining the **field** propagation length as $L_{\mathrm{p}}^{\mathrm{tl}} = 1/\Gamma_{\mathrm{tl}}$ and $L_{\mathrm{p}}^{\mathrm{SPP}} = 1/\Gamma_{\mathrm{SPP}}$, this also means:

$$L_{\mathrm{p}}^{\mathrm{tl}} = \frac{L_{\mathrm{p}}^{\mathrm{SPP}}}{2} \tag{3.4}$$

and, as the wavelength of the SPPs is defined as $\Lambda_{\mathrm{tl}} = 2\pi/K_{\mathrm{tl}}$, the tip-launched wavelength is given by

$$\Lambda_{\mathrm{tl}} = \frac{\lambda_{\mathrm{SPP}}}{2} = \frac{\lambda_0}{2\,\mathrm{Re}(\tilde{n})}, \tag{3.5}$$

where λ_{SPP} is the SPP wavelength, λ_0 is the laser wavelength in free space, and $\mathrm{Re}(\tilde{n})$ is the real part of the SPP effective refractive index, defined as $\tilde{n} = \sqrt{\frac{\varepsilon_{\mathrm{m}}\varepsilon_{\mathrm{d}}}{\varepsilon_{\mathrm{m}}+\varepsilon_{\mathrm{d}}}}$. The factor 2 between the real SPP wavelength λ_{SPP} and the measured wavelength Λ_{tl} due to the tip-launched SPP path has been mentioned in several works [17,36,49,50].

In the following, the variable K is be used when plotting the wavevector in the coordinates (x, y, z) of the near-field map, while the variable q is used whenever the SPP wavevector in the coordinates (x', y', z') is plotted.

3.1.2 Edge-launched and tip-reflected edge-launched SPPs

As mentioned in Section 2.3, the SPPs on gold are not particularly confined. They can therefore be excited not only by the s-SNOM tip, but also at the sharp edges of the monocrystalline gold platelets. Furthermore, the incident laser is focused on the tip with a parabolic mirror of numerical aperture NA $= 0.37$. Thus, the diffraction-limited laser spot has a diameter of $\phi = 2.1$ µm at the focal point of the parabolic mirror. In addition, the light is focused on the tip at an incident polar angle of $\theta = 60°$. The size of the spot on the gold surface is thus not a disk, but rather an ellipse of minor axis ϕ and of major axis about 8.5 µm, which is much larger than the tip apex radius of about 25 nm.

Hence, when the tip comes closer to the edge of the platelet, the laser beam starts to cover the sharp edge of the platelet, which means that SPPs can also be launched and scattered from the edge. These SPPs are called edge SPPs in the following. They can be separated in different categories depending on their optical paths. These categories are presented in Figure 3.2. They have been observed and studied using a s-SNOM setup without interferometric detection (as in Figure 1.3), mainly by Walla et al. [35] and Kaltenecker et al [36].

The first category (see Figure 3.2a) is the edge-launched SPPs [35]. These SPPs are excited at the edge, propagate towards the tip and are scattered by the tip towards the detector, where they interfere with the rest of the signal. The wavelength corresponding to the interference between these edge-launched SPPs and the background field E_B (as defined in Section 1.1.3) has been calculated [35] as

$$\Lambda_{\mathrm{el1}}(\theta,\varphi) = \frac{\lambda_0}{-\sin(\theta)\sin(\varphi) + \sqrt{\sin^2(\theta)\sin^2(\varphi) - \sin^2(\theta) + \mathrm{Re}(\tilde{n})^2}}, \tag{3.6}$$

where θ is the polar angle of the incident light, and φ is the azimuthal angle between the edge and the incident light (see Figure 3.2a).

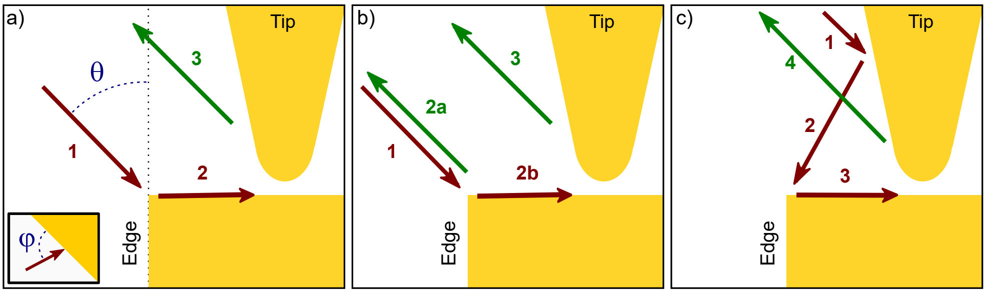

Figure 3.2. Sketch of the optical paths for the different types of edge SPPs. a) Path for the first type of edge-launched SPP interference leading to a signal of wavelength Λ_{el1}. The inset shows a top view of the gold and highlights the angle φ between the platelet edge and the incident light. b) Path for the second type of edge-launched SPP interference leading to a signal of wavelength Λ_{el2}. c) Path for the tip-reflected edge-launched SPPs interference leading to a signal of wavelength Λ_{trel}.

Another category of edge-launched SPP interference has been identified by Kaltenecker et al. [36] (see Figure 3.2b). These SPPs are also excited at the edge and propagate towards the tip, but interfere with the light that is scattered back directly at the edge. As these SPPs are launched the same way as the edge-launched SPPs, they are referred to as the second type of edge-launched SPPs. The wavelength corresponding to the interference between these SPPs and the background field has been calculated to be [36]

$$\Lambda_{\mathrm{el2}}(\theta, \varphi) = \frac{\lambda_0}{+\sin(\theta)\sin(\varphi) + \sqrt{\sin^2(\theta)\sin^2(\varphi) - \sin^2(\theta) + \mathrm{Re}(\tilde{n})^2}}, \tag{3.7}$$

which means that $\Lambda_{\mathrm{el2}}(\theta, \varphi) = \Lambda_{\mathrm{el1}}(\theta, -\varphi)$. Note that inverting the arrows in Figures 3.2a and 3.2b leads also to the detection of SPP patterns, scattered from the edge instead of being launched at the edge. As these SPPs have the same optical path as the edge-launched SPPs, they lead to the same wavelengths and thus cannot be differentiated from the edge-launched SPPs.

As the beam spot does not cover only the tip apex but also the tip shaft, a third category of edge SPPs arises from the light reflected at the tip shaft towards the edge (see Figure 3.2c). The SPPs are then again excited at the edge, propagate towards the tip, and are scattered by the tip towards the detector, where they interfere with the rest of the signal. These SPPs are called the tip-reflected edge-launched SPPs. As the angle of incidence at the edge here strongly depends on the geometry of the tip, the wavelength corresponding to the interference of these SPPs with the background field is usually estimated with the expression [35, 36]

$$\Lambda_{\mathrm{trel}} = \Lambda_{\mathrm{el1}}(\theta', \varphi), \tag{3.8}$$

where θ' is a fitting parameter corresponding to the polar angle between the light reflected at the tip and the surface of the platelet [35].

It should be noted that all these wavelengths correspond to the interference between the SPPs and the large background field E_{B} due to the direct back-scattering of the laser light towards the detector [36]. The SPPs can also interfere with each other, but since the strength of their signal is low compared to the background field, the interferences between SPPs are considered as second-order effects having little influence on the total signal. Furthermore, the PsHet detection is supposed to remove the background field. The validity of Equations 3.7, 3.7 and 3.8 should thus be tested when characterizing the edge SPPs with s-SNOM and PsHet detection.

3.2 Isolation of the tip-launched SPPs

As mentioned in Section 3.1, the measurement of SPPs on gold with s-SNOM involves several excitation channels, which leads to complex interference patterns close to the edge of the platelet. In our previous study [36], a method was developed to isolate and extract the wavelength of the tip-launched SPPs on a monocrystalline gold platelet. However, the propagation length could not be characterized. The platelets were indeed too small for the propagation length of SPPs on gold, such that in most cases the tip-launched SPPs reflected from different edges would influence each other.

Moreover, the initial approximation of the tip-launched SPPs as PWs - instead of circular waves (CWs) - was shown to not describe these SPPs properly.

This section presents the experimental details and study of the incident angle dependence from our work [66], leading to the the isolation of a clear tip-launched signal.

3.2.1 Experimental details

Figure 3.3a shows an optical image from the sample used to measure the SPPs on gold. It consists in a monocrystalline gold platelet covered with aluminum oxide (Al_2O_3) and deposited on a chip made of silicon on which a 300-nm silicon oxide (SiO_2) layer was thermally grown. The sketch of the sample cross section in the inset highlights these different layers (the silicon is not represented for simplification).

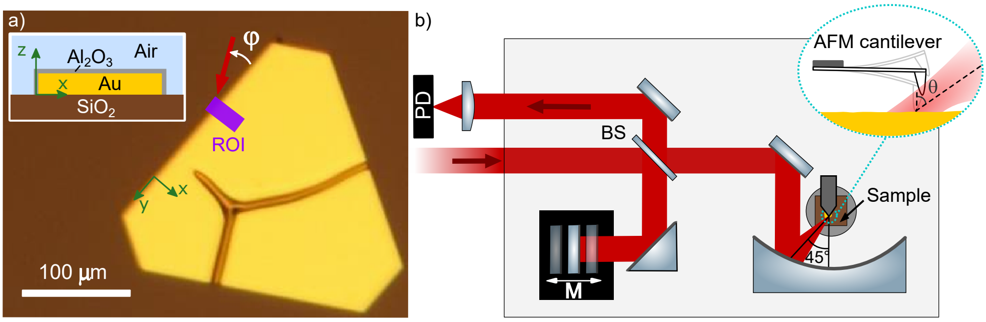

Figure 3.3. Sample and experimental setup. a) Optical image of the sample. The red arrow represents the incident light, impinging of the sample with an azimuthal angle φ. The region of interest (ROI) is highlighted by the violet rectangle. The inset shows a sketch of the substrate and sample cross-section. b) Sketch of the s-SNOM setup (same configuration as in Figure 1.5). Figures from [66]. ©2022 *Optica Publishing Group under the terms of the Open Access Publishing Agreement.*

The sample was purchased from Nanostruct GmbH. The gold platelets were grown by a wet-chemical synthesis process [81], which creates crystals with a high aspect ratio and a typical root-mean-square (RMS) roughness of 200 pm (value given by the supplier and confirmed in [36]). The platelet is about 200 µm large and about 90 nm thin. The 2-nm layer of Al_2O_3 has been deposited by atomic layer deposition to protect the gold surface from impurities. It is also used as a spacer between the gold platelet and the van der Waals material in Chapter 5.

The darker branching trace in the middle of the platelet corresponds to a fold that has likely been created during the deposition on the substrate. This fold is - at worst - about 50 µm away from the region of interest (ROI). Knowing that the typical propagation length of SPPs is predicted to be about 10-14 µm [73,77], eventual SPPs launched or reflected at this fold should not interfere with the measurement.

Following the same logic, the SPPs launched or reflected from other edges of the platelet do not influence the measurement either, as the ROI is far from the platelet's corners.

Figure 3.3b represents the s-SNOM configuration used in the experiments. A stabilized HeNe laser (HRS015 from Thorlabs GmbH) has been used to focus light of wavelength 633 nm onto a platinum-coated s-SNOM tip (nominal apex radius: 25 nm). The polar angle between the light incidence and the normal to the surface is $\theta = 60°$. PsHet detection was used to suppress the background field and retrieve the amplitude and phase of the near field, as explained in Section 1.2.1. The 3$^{\text{rd}}$ harmonic of the tip oscillation frequency has been used to obtain the near-field amplitude and phase. The resulting maps - made with a scanning step size of 30 nm and a step integration time of 6.6 ms - are described and analyzed in the following sections.

3.2.2 Amplitude and phase profiles

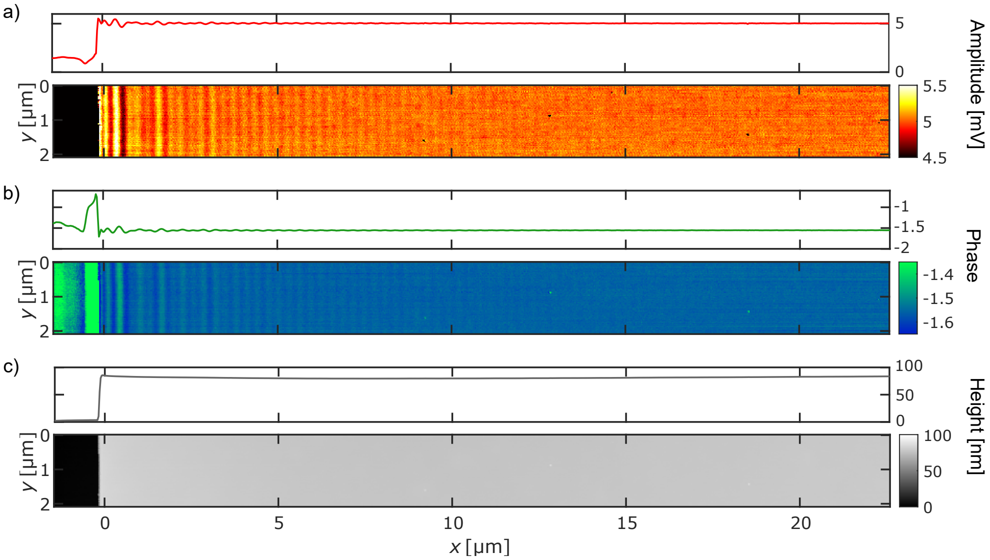

Figure 3.4. Measurement results. a) Near-field amplitude, b) near-field phase, and c) topography of the ROI for an incidence angle of $\varphi = -3°$. The respective profiles are displayed above the maps, and the origin of the x-axis is chosen to be at the platelet's edge. Figures from [66]. ©2022 *Optica Publishing Group under the terms of the Open Access Publishing Agreement.*

Figure 3.4 displays the maps of the near-field amplitude (Figure 3.4a), near-field phase (Figure 3.4b) and topography (Figure 3.4c) of the ROI. The scales of the near-field amplitude and phase are adjusted and the map of initial width 36 µm has been cropped to highlight the interference patterns on the gold. These interference patterns are due to the edge SPPs and tip-launched SPPs. Moreover, the position of the origin of the x-axis has been chosen at the edge of the platelet. The sample thickness of about 90 nm is confirmed by the topography. The gold platelet is thus thick enough to avoid hybridization between the SPPs at the air/gold and the SPPs at the gold/SiO_2 interfaces [36, 82]. Furthermore, the topography confirms the sharp and defect-less edge of the gold platelet. This property is important, as a small defect at the edge could act as a local scatterer that launches SPPs and thus perturb the interference patterns of the near-field amplitude and phase.

For all the measured maps, the scanning area is rotated such that the maps always have the edge in the vertical direction (along y). These maps are invariant along the y-direction and profiles can be made by averaging 200 pixels in the y-direction, without loss of information. These profiles are shown above each amplitude, phase and topography map, respectively, and highlight that the interference patterns on the gold are superimposed with an offset. A change in this offset can be seen, especially in the amplitude profile, at the boundary between the silicon ($x < 0$) and the gold ($x > 0$). Note that, on the gold, the offset of the near-field amplitude is much larger than the SPP oscillations. This characteristic is used in Section 3.3, and the nature of the offset is discussed in the same section.

3.2.3 Influence of the incident angle

Figure 3.5 presents the near-field amplitude profiles of the SPPs on gold from measurements at six different azimuthal angles φ between the incident light and the platelet's edge. To highlight the interference patterns, the constant offset has been subtracted and the amplitude profiles have been normalized. The respective Fourier transforms are presented below each profile. The insets depict a top view of the sample, with the approximate direction of the light indicated by the red arrow.

Two regions can be distinguished in the amplitude profiles. The region closest to the edge (white area) shows interference patterns with either long wavelengths compared to the wavelength of the expected tip-launched SPPs, or complex interference patterns. This region is characterized by the interference contributions from the edge-launched SPPs and the tip-reflected edge-launched SPPs in addition to the tip-launched SPPs. By contrast, a few micrometers away from the edge (red area starting at x_b), the edge SPPs cannot contribute anymore to the signal, as the incident light does not cover the edges anymore. Thus, only the tip-launched SPP oscillations remain.

The different SPP contributions at each angle φ can be recognized in the FT of each profile (black curves in the lower panel of Figures 3.5a-f). The FT was applied to the profiles by applying the fast Fourier transform (FFT) algorithm from Matlab®. Table 3.1 summarizes the predicted wavelength of the edge SPPs for each angle φ. This angle is calculated using the nominal value of 45° for the incidence light, the rotation angle of the scanning direction, and the measure of the angle between the edge and the vertical in the maps. The angle θ is taken as 60° (nominal value) for the edge-launched SPPs and 35° for the tip-reflected edge-launched SPPs. We use the dielectric function from Aguilar-Gama et al. [83] for the Al_2O_3 and the one from McPeak et al. [77] for the gold to calculate in-plane wavevector q of the multilayer structure [18] and deduce the refractive index as $\tilde{n} = q/(\omega/c)$. Thereby, we find a value of $\mathrm{Re}(\tilde{n}) = 1.045$. The vertical lines indicate the predicted position of the edge SPP wavelengths, calculated using Equations 3.6, 3.7 and 3.8.

φ (°)	Λ_{el1} (µm)	Λ_{el2} (µm)	Λ_{trel} (µm)
-3	1.0	1.2	0.71
43.1	2.6	0.44	1.1
87.2	3.5	0.33	1.3
178.5	1.1	1.0	0.73
-136	0.44	2.7	0.47
-93	0.33	3.5	0.39

Table 3.1. Predicted values for the edge SPPs as a function of the azimuthal angle φ, calculated from Equations 3.6, 3.7 and 3.8

For angles φ equal to 43.1° and 87.2°, a large contribution probably coming from the tip-reflected edge-launched SPPs can be recognized. By contrast, for angles of -136° and -93°, the first type of edge-launched SPPs are prominent. For the same angles, Λ_{trel} is calculated to be very close to Λ_{el1}, but since the tip-reflected edge-launched SPPs are created by reflection at the tip towards the edge (recall Figure 3.2c), they are unlikely to be excited in a configuration where the edge is behind the tip. Furthermore, no clear effect from the second type of edge-launched SPPs, of wavelength Λ_{el2}, can be seen for any of the studied angles, contrary to what has been reported in Ref. [36]. As this type of SPPs is interfering with the light directly back-scattered at the edge, which is part of the background light, the absence of clear peak at Λ_{el2} gives an indication that the PsHet detection is effective in suppressing the background.

For angles φ of -3° and 178.5°, i.e. at grazing incidence angle, the tip-launched SPP peak at the predicted wavelength of $\Lambda_{\mathrm{tl}} = 0.303$ µm is much more pronounced than for the other angles. This effect is particularly visible for $\varphi = -3°$. Several reasons can induce this effect. First, all the wavelengths of the edge SPPs are further away from Λ_{tl} than for the other angles. The peak at Λ_{tl} is thus not hidden behind another, more prominent peak. Second, the excitation of SPPs at the edges could be less effective at grazing incidence angle. Moreover, the projection of the laser spot size on the sample is smaller at grazing incident angle, which means that the interference patterns from the edge SPPs cover a smaller portion of the profile (see the different positions of x_b depending on the angle). Finally, the tip itself could excite more efficiently SPPs at specific angles. A previous study [35] has indeed highlighted that, since s-SNOM tips are not circularly symmetric, the excitation of SPPs is anisotropic. This anisotropic excitation could thus explain why the tip-launched SPPs seem more pronounced at an angle of -3° compared to 178.5°.

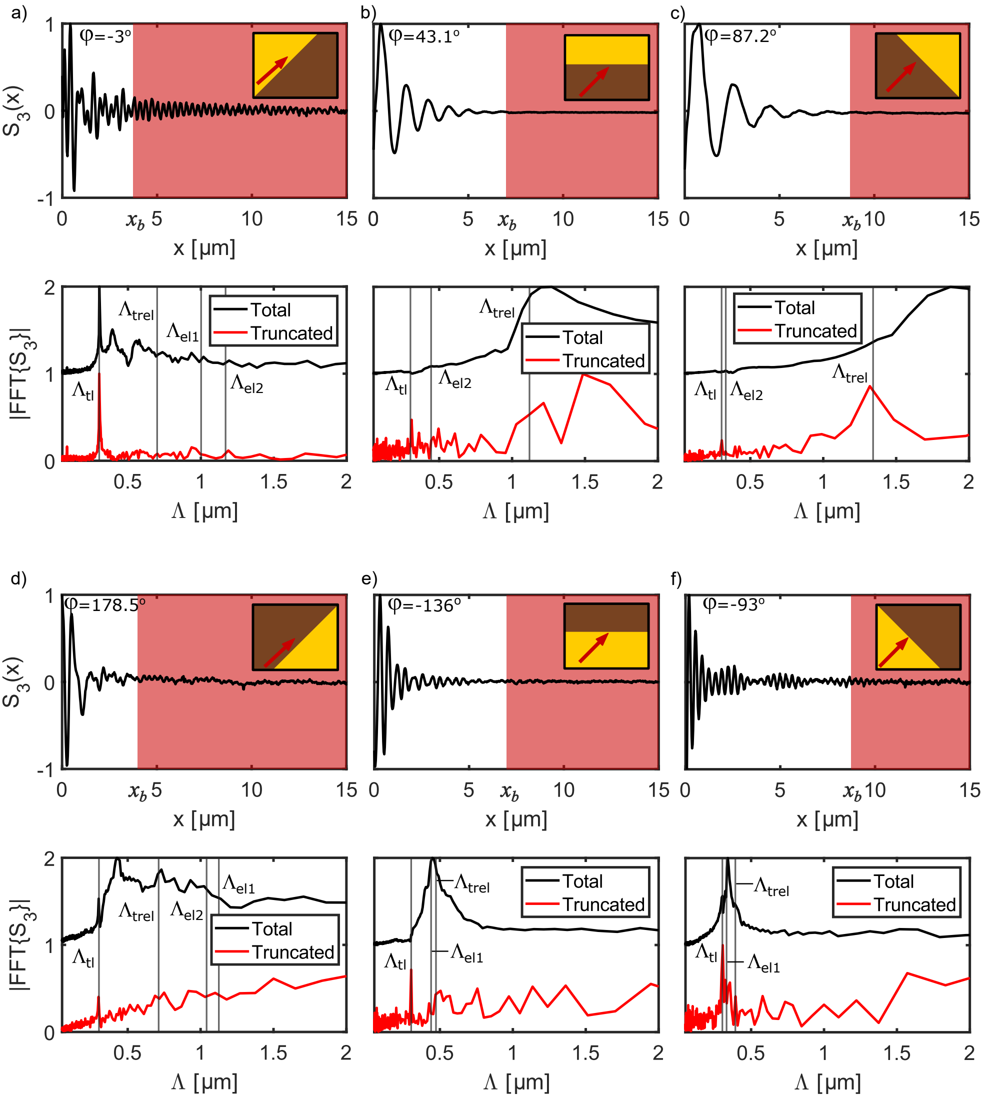

Figure 3.5. **Amplitude profiles and respective Fourier transforms (FT)** for an incident azimuthal angle of a) $\varphi = -3°$, b) $\varphi = 43.1°$, c) $\varphi = 87.2°$, d) $\varphi = 178.5°$, e) $\varphi = -136°$ and $\varphi = -93°$. The spectra are plotted as a function of the fringe spacing $\Lambda = 2\pi/K$. The profile truncated at x_b is highlighted by the red area and the corresponding FT is displayed as the red spectrum. The vertical lines highlight the predicted position of the tip-launched and edge SPPs' wavelength, calculated using Equations 3.5, 3.6, 3.7 and 3.8. The insets depict a top view of the sample, where the red arrows represent the directions of the incident light. Figures from [66]. ©2022 *Optica Publishing Group under the terms of the Open Access Publishing Agreement.*

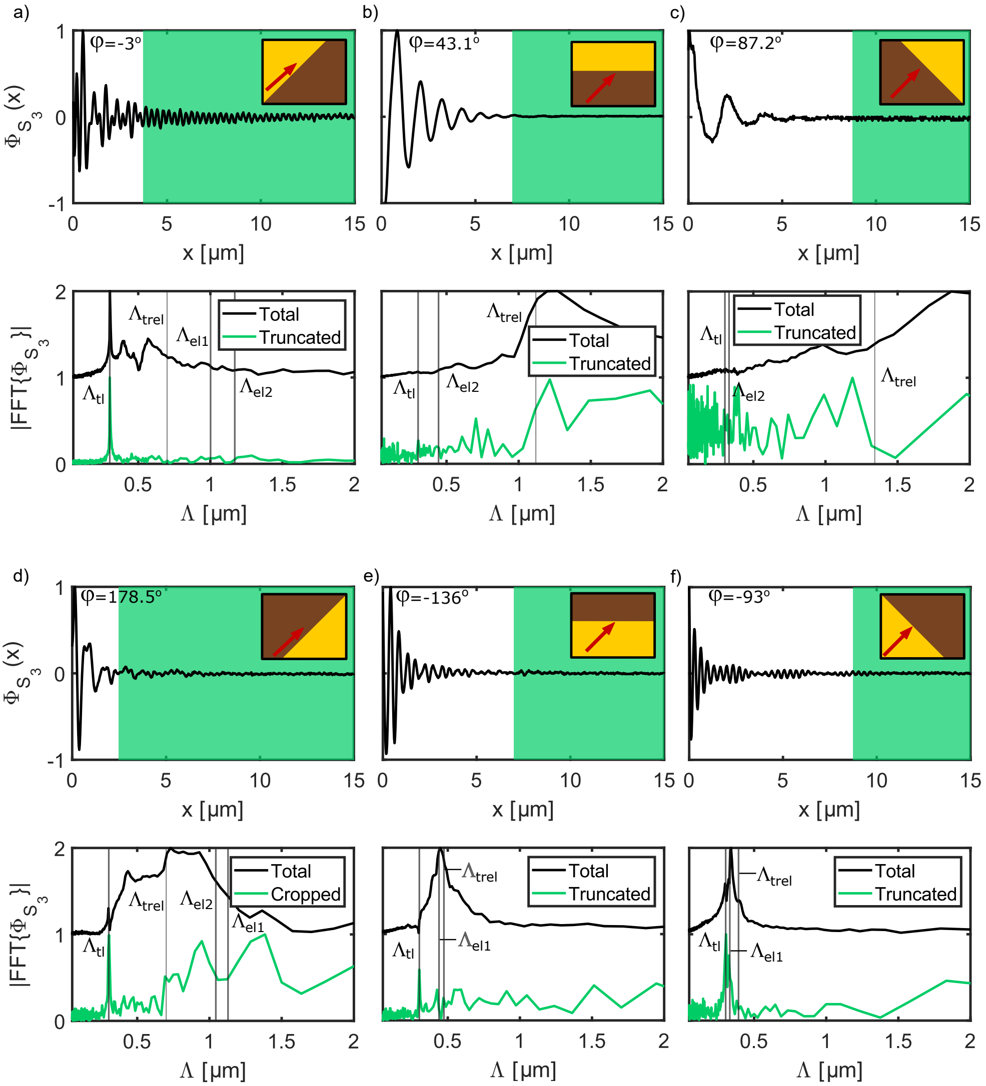

Figure 3.6. **Phase profiles and respective Fourier transforms (FT)** for an incident azimuthal angle of a) $\varphi = -3°$, b) $\varphi = 43.1°$, c) $\varphi = 87.2°$, d) $\varphi = 178.5°$, e) $\varphi = -136°$ and $\varphi = -93°$. The spectra are plotted as a function of the fringe spacing $\Lambda = 2\pi/K$. The truncated profile is highlighted by the green area and the corresponding FT is displayed as the green spectrum. The vertical lines highlight the positions of the tip-launched and edge-launched SPPs. The insets depict a top view of the sample, where the red arrows represent the directions of the incident light.

The prominence of the tip-launched peak directly influences the characterization of the tip-launched SPPs. To highlight this point, the FT of the truncated profile lying in the red region, starting at x_b, is plotted (red spectra of Figure 3.5). For all the resulting spectra, the peak from the tip-launched SPPs is made clearer, such that the wavelength of the tip-launched SPPs can be measured. However, most of the peaks are still too noisy for a proper characterisation of the propagation length, related to the width of the peaks. By contrast, the peak of the truncated profile in Figure 3.5a ($\varphi = -3°$) shows a much lower noise floor and can thus be used to measure the tip-launched SPP propagation length.

Figure 3.6 presents the near-field phase profiles from the same measurements as in Figure 3.5. The phase profiles present the same type of oscillations, and the corresponding spectra show similar peaks, where the same types of edge SPPs and tip-launched SPPs can be recognized. The phase profiles thus seem to contain the same information as the amplitude profiles.

Intuitively, it could be argued that, if the PsHet detection removes the background - which was the previous reason for the SPP interferences - then the pure SPP signal should be retrieved by the s-SNOM. In this scenario, in the region further from the edge where only the tip-launched SPPs are left, the near-field amplitude would be a decaying exponential and the near-field phase would be varying from $-\pi$ to π, as a non-interfering field reconstructed using the inverse tangent function [84]. As none of the aforementioned profiles show these characteristics, a further understanding of and the derivation of expressions for the near-field amplitude and phase are needed.

3.3 Derivation of expressions for the near-field profiles

The PsHet detection suppresses the background coming from light back-scattered directly towards the detector [14]. Since interference fringes in the near-field measurements of the SPPs are still present, the SPPs must interfere with some other signal coming from the near-field.

In this section, the derivation of the expression for the near-field amplitude and near-field phase of the tip-launched SPPs is presented, based on the observation of the experimental amplitude and phase profiles. The derivation follows the supplementary information in Ref. [66]. Lastly, the limits to the approximations made in order to get these expressions are tested.

3.3.1 Measurement profiles

Figures 3.7a and 3.7b present the full profile of the near-field amplitude and phase from the measurement at $\varphi = 3°$. Both these profiles are well-fitted with a CW description - attributed to the tip-launched SPP contribution, as in Ref. [49] - superimposed with a constant offset. Far away from the edge ($x > 30$ µm), the oscillations from the CW become negligible and only the offset remains. The amplitude offset is defined as $|E_{\mathrm{g}}|$ and the phase offset as ϕ_{g}. In the region where only the edge SPPs are absent, the near field obtained with the s-SNOM can thus be expressed as

$$E_{\mathrm{NF}} = E_{\mathrm{tl}} + E_{\mathrm{g}} \text{ with } E_{\mathrm{tl}} = \frac{A}{\sqrt{x}} e^{-\Gamma_{\mathrm{tl}} x} e^{i(K_{\mathrm{tl}} x - \phi_{\mathrm{p}})} \text{ and } E_{\mathrm{g}} = |E_{\mathrm{g}}| e^{i\phi_{\mathrm{g}}} \tag{3.9}$$

where E_{tl} is the tip-launched SPP field defined as in Equation 3.1, and E_{g} is the field corresponding to the offset.

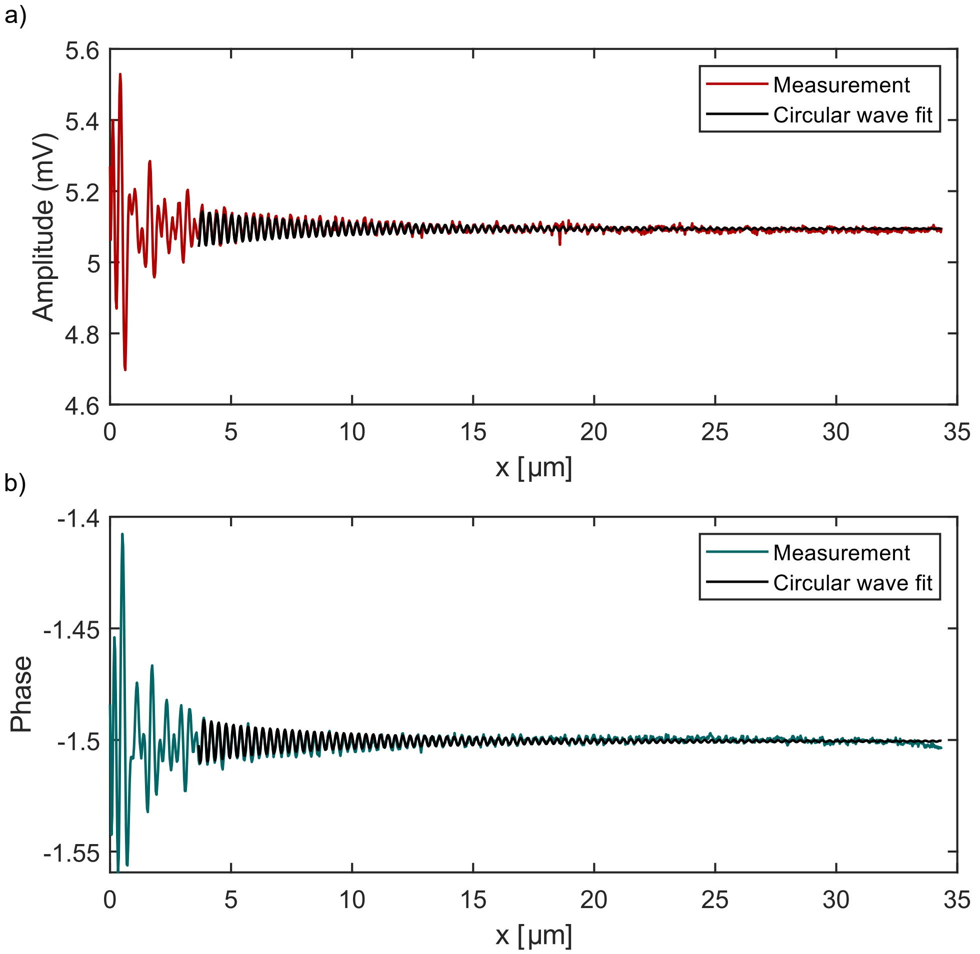

Figure 3.7. Measurement profiles. a) Near-field amplitude and CW fit. b) Near-field phase and CW.

In the literature treating s-SNOM measurement of SPPs with PsHet detection, an article studying the origin of the interference patterns explains these patterns as the result of the interference between the SPPs (in this case only one type of edge-launched SPPs) with the incident light and its direct reflection at the gold surface [85]. However, if the PsHet detection removes the far-field background as mentioned in Section 1.2.1, then the origin of the offset should be purely near-field. Indeed, in the work from Woessner et al. [49], the interference pattern of the graphene plasmons is interpreted as coming from the interference with the "local response", meaning the near-field response of the scanned surface due to the coupling to the AFM tip. The same interpretation is given in the work from Barnett et al. [79], where the constant is mentioned as the near-field contrast of the material in the absence of surface waves. This "local response" is depending on the evanescent reflection coefficient of the surface [49, 53] and is thus constant throughout the scan, as long as the scanned material or topography is not changed. In our view, this near-field interpretation of the offset is much more convincing, especially because other works use this near-field response to extract material parameters such as the dielectric function [53, 86].

3.3.2 Amplitude

The amplitude squared of the total field is

$$\begin{aligned} |E_{\mathrm{NF}}|^2 &= |E_{\mathrm{tl}} + E_{\mathrm{g}}|^2 && (3.10)\\ &= |E_{\mathrm{tl}}|^2 + |E_{\mathrm{g}}|^2 + E_{\mathrm{tl}}^* E_{\mathrm{g}} + E_{\mathrm{tl}} E_{\mathrm{g}}^* && (3.11)\\ &= \frac{A^2}{x} e^{-2\Gamma_{\mathrm{tl}} x} + |E_{\mathrm{g}}|^2 + 2\frac{A|E_{\mathrm{g}}|}{\sqrt{x}} e^{-\Gamma_{\mathrm{tl}} x} \cos(K_{\mathrm{tl}} x - \phi_{\mathrm{p}} - \phi_{\mathrm{g}}) && (3.12) \end{aligned}$$

When fitting the near-field amplitude with Equation 3.10, we obtain: $|E_{\mathrm{g}}| = 5.1$ mV, $A = 0.13$ mV.$\sqrt{\mu\mathrm{m}}$. Furthermore, x is in the interval [3 µm, 30 µm]. Thus, in the interval where the tip-launched SPPs are present, the maximum value of the dimensionless quantity $\frac{A}{|E_{\mathrm{g}}|\sqrt{x}}$ is $\frac{A}{|E_{\mathrm{g}}|\sqrt{x}} = \frac{0.13}{5.1\sqrt{3}} = 0.015$.

At the first-order Taylor approximation in the variable $\frac{A}{|E_{\mathrm{g}}|\sqrt{x}}$, the first term of Equation 3.12 can be neglected and the expression becomes

$$|E_{\mathrm{NF}}|^2 \approx |E_{\mathrm{g}}|^2 \left(1 + 2\frac{A}{|E_{\mathrm{g}}|\sqrt{x}} e^{-\Gamma_{\mathrm{tl}} x} \cos(K_{\mathrm{tl}} x - \phi_{\mathrm{p}} - \phi_{\mathrm{g}})\right). \tag{3.13}$$

Thus, the amplitude can be expressed as

$$|E_{\mathrm{NF}}| = |E_{\mathrm{g}}| \sqrt{1 + 2\frac{A}{|E_{\mathrm{g}}|\sqrt{x}} e^{-\Gamma_{\mathrm{tl}} x} \cos(K_{\mathrm{tl}} x - \phi_{\mathrm{p}} - \phi_{\mathrm{g}})}, \tag{3.14}$$

and using again the first-order Taylor approximation, we end up with the final expression for the near-field amplitude profile

$$\boxed{|E_{\mathrm{NF}}| \approx |E_{\mathrm{g}}| + \frac{A}{\sqrt{x}} e^{-\Gamma_{\mathrm{tl}} x} \cos(K_{\mathrm{tl}} x - \phi)} \tag{3.15}$$

with $\phi = \phi_\mathrm{p} + \phi_\mathrm{g}$.

The information that can be accessed in the amplitude fit is thus $|E_\mathrm{g}|$, A, ϕ, and the SPP characterization constants K_tl and Γ_tl.

As only the total phase $\phi = \phi_\mathrm{p}+\phi_\mathrm{g}$ can be accessed in the amplitude measurement, the phase information should be expressed in the same way in the following section, to capture a possible global phase shift.

3.3.3 Phase

As seen in Section 1.2.1, when using the PsHet detection, the near-field phase Φ_NF can only be reconstructed up to the additive constant Φ_R related to the reference field. The near-field phase can thus be expressed as

$$\Phi_\mathrm{NF} = \arctan\left(\frac{\mathrm{Im}(E_\mathrm{tl} + E_\mathrm{g})}{\mathrm{Re}(E_\mathrm{tl} + E_\mathrm{g})}\right) - \Phi_\mathrm{R}, \tag{3.16}$$

where “Im(...)” represent the imaginary part and “Re(...)” the real part. Note that to obtain this expression we supposed $\mathrm{Re}(E_\mathrm{g}) > 0$, meaning that - with relatively small oscillations from E_tl - the phase $\Phi_\mathrm{NF} + \Phi_\mathrm{R}$ has values always between $-\pi/2$ and $\pi/2$. Having $\mathrm{Re}(E_\mathrm{g}) < 0$ would only change the result by an additional constant π, so the analysis would be the same.

In this section, we derive the phase profile expression for two different cases:

- for $\mathrm{Re}(E_\mathrm{g})$ not small compared to $|E_\mathrm{g}|$. This means $\mathrm{Re}(E_\mathrm{g}) \gg \mathrm{Im}(E_\mathrm{g})$ (hence $\mathrm{Re}(E_\mathrm{g}) \approx |E_\mathrm{g}|$) or $\mathrm{Re}(E_\mathrm{g}) \approx \mathrm{Im}(E_\mathrm{g})$ (hence $\mathrm{Re}(E_\mathrm{g}) \approx |E_\mathrm{g}|/\sqrt{2}$).
- for $\mathrm{Re}(E_\mathrm{g})$ small compared to $|E_\mathrm{g}|$, meaning $\mathrm{Re}(E_\mathrm{g}) \ll \mathrm{Im}(E_\mathrm{g})$.

Case where $\mathrm{Re}(E_\mathrm{g})$ is not small compared to $|E_\mathrm{g}|$.

To simplify the expressions, we calculate the quantity $F = \tan(\Phi_{NF}) = \frac{\mathrm{Im}(E_\mathrm{tl}+E_\mathrm{g})}{\mathrm{Re}(E_\mathrm{tl}+E_\mathrm{g})}$. F can be expressed as

$$F = \frac{\mathrm{Im}(E_\mathrm{g}) + |E_\mathrm{p}|\sin(K_\mathrm{tl}x - \phi_\mathrm{p})}{\mathrm{Re}(E_\mathrm{g}) + |E_\mathrm{p}|\cos(K_\mathrm{tl}x - \phi_\mathrm{p})} \tag{3.17}$$

$$= \frac{1}{\mathrm{Re}(E_\mathrm{g})}\frac{\mathrm{Im}(E_\mathrm{g}) + |E_\mathrm{p}|\sin(K_\mathrm{tl}x - \phi_\mathrm{p})}{1 + |E_\mathrm{p}|/\mathrm{Re}(E_\mathrm{g})\cos(K_\mathrm{tl}x - \phi_\mathrm{p})}, \tag{3.18}$$

with $|E_\mathrm{p}| = \frac{A}{\sqrt{x}}e^{-\Gamma_\mathrm{tl}x}$.

Since $|E_\mathrm{p}|/\mathrm{Re}(E_\mathrm{g}) = \frac{A}{\mathrm{Re}(E_\mathrm{g})\sqrt{x}}e^{-\Gamma_\mathrm{tl}x} \ll 1$, we can make the first-order Taylor approximation

$$F \approx \frac{1}{\mathrm{Re}(E_\mathrm{g})}[\mathrm{Im}(E_\mathrm{g}) + |E_\mathrm{p}|\sin(K_\mathrm{tl}x - \phi_\mathrm{p})][1 - |E_\mathrm{p}|/\mathrm{Re}(E_\mathrm{g})\cos(K_\mathrm{tl}x - \phi_\mathrm{p})] \tag{3.19}$$

$$\approx \frac{\mathrm{Im}(E_\mathrm{g})}{\mathrm{Re}(E_\mathrm{g})} + \frac{|E_\mathrm{p}|}{\mathrm{Re}(E_\mathrm{g})}\sin(K_\mathrm{tl}x - \phi_\mathrm{p}) - \frac{\mathrm{Im}(E_\mathrm{g})}{\mathrm{Re}(E_\mathrm{g})^2}|E_\mathrm{p}|\cos(K_\mathrm{tl}x - \phi_\mathrm{p}). \tag{3.20}$$

Using the polar representation $E_\mathrm{g} = |E_\mathrm{g}|e^{i\phi_\mathrm{g}}$, one can rearrange the terms and find

$$\begin{aligned} F &= \frac{1}{\mathrm{Re}(E_\mathrm{g})^2}\left[\mathrm{Im}(E_\mathrm{g})\,\mathrm{Re}(E_\mathrm{g}) + |E_\mathrm{g}||E_\mathrm{p}|\sin(K_\mathrm{tl}x - \phi_\mathrm{p} - \phi_\mathrm{g})\right] && (3.21)\\ &= \frac{1}{\mathrm{Re}(E_\mathrm{g})^2}\left[\mathrm{Im}(E_\mathrm{g})\,\mathrm{Re}(E_\mathrm{g}) + |E_\mathrm{g}|\frac{A}{\sqrt{x}}e^{-\Gamma_\mathrm{tl}x}\sin(K_\mathrm{tl}x - \phi)\right]. && (3.22)\end{aligned}$$

This means that the phase Φ_{NF} can be expressed as

$$\Phi_{NF} \approx \arctan\left(\frac{\mathrm{Im}(E_\mathrm{g})}{\mathrm{Re}(E_\mathrm{g})} + |E_\mathrm{g}|\frac{A}{\mathrm{Re}(E_\mathrm{g})^2\sqrt{x}}e^{-\Gamma_\mathrm{tl}x}\sin(K_\mathrm{tl}x - \phi)\right) - \Phi_\mathrm{R}. \tag{3.23}$$

The first-order Taylor approximation of $\arctan(a + X)$ in the variable X can the be used for $X \ll 1$ and $a = \frac{\mathrm{Im}(E_g)}{\mathrm{Re}(E_g)}$,

$$\arctan(a + X) \approx \arctan(a) + \frac{X}{1 + a^2} \tag{3.24}$$

to obtain from Equation 3.23 the expression

$$\Phi_{NF} \approx \arctan\left(\frac{\mathrm{Im}(E_g)}{\mathrm{Re}(E_g)}\right) - \Phi_R + \frac{|E_g|}{\mathrm{Re}(E_g)^2\left(1 + \frac{\mathrm{Im}(E_g)^2}{\mathrm{Re}(E_g)^2}\right)}\frac{A}{\sqrt{x}}e^{-\Gamma x}\sin(K_{tl}x - \phi). \tag{3.25}$$

As a result, the phase can be expressed as

$$\boxed{\Phi_{NF} \approx \arctan\left(\frac{\mathrm{Im}(E_g)}{\mathrm{Re}(E_g)}\right) - \Phi_R + \frac{A}{|E_g|\sqrt{x}}e^{-\Gamma x}\sin(K_{tl}x - \phi).} \tag{3.26}$$

Case where $\mathrm{Re}(E_\mathbf{g})$ is small compared to $|E_\mathbf{g}|$.

For this case, the relationship $\arctan\left(\frac{1}{x}\right) = \pm\frac{\pi}{2} - \arctan(x)$ can be used, where the "+" corresponds to $x > 0$ and "−" to $x < 0$. By using this relationship, we can get back to the same starting point as in Equation 3.18, with the imaginary parts being replaced by the real parts and inversely:

$$G = \frac{1}{F} = \frac{1}{\mathrm{Im}(E_\mathrm{g})}\frac{\mathrm{Re}(E_\mathrm{g}) + |E_\mathrm{p}|\cos(K_\mathrm{tl}x - \phi_\mathrm{p})}{1 + |E_\mathrm{p}|/\,\mathrm{Im}(E_\mathrm{g})\sin(K_\mathrm{tl}x - \phi_\mathrm{p})}. \tag{3.27}$$

Thus, this leads to a similar derivation as in the first case, leading to the expression

$$G = \frac{1}{\mathrm{Im}(E_\mathrm{g})^2}\left[\mathrm{Re}(E_\mathrm{g})\,\mathrm{Im}(E_\mathrm{g}) + |E_\mathrm{g}|\frac{A}{\sqrt{x}}e^{-\Gamma_\mathrm{tl}x}\sin(\phi - K_\mathrm{tl}x)\right]. \tag{3.28}$$

This means that in this last case the phase Φ_{NF} can be expressed as

$$\Phi_\mathrm{NF} \approx \pm\frac{\pi}{2} - \arctan\left(\frac{\mathrm{Re}(E_\mathrm{g})}{\mathrm{Im}(E_\mathrm{g})} - |E_\mathrm{g}|\frac{A}{\mathrm{Im}(E_\mathrm{g})^2\sqrt{x}}e^{-\Gamma_\mathrm{tl}x}\sin(K_\mathrm{tl}x - \phi)\right) - \Phi_\mathrm{R} \tag{3.29}$$

and by using again Equation 3.24 with $a = \frac{\mathrm{Re}(E_g)}{\mathrm{Im}(E_g)}$, it becomes

$$\Phi_{NF} \approx \pm\frac{\pi}{2} - \arctan\left(\frac{\mathrm{Im}(E_\mathrm{g})}{\mathrm{Re}(E_\mathrm{g})}\right) + \frac{A}{|E_\mathrm{g}|\sqrt{x}} e^{-\Gamma_\mathrm{tl} x} \sin(K_\mathrm{tl} - \phi) - \Phi_\mathrm{R}, \tag{3.30}$$

which can be reduced to

$$\boxed{\Phi_{NF} = \arctan\left(\frac{\mathrm{Re}(E_\mathrm{g})}{\mathrm{Im}(E_\mathrm{g})}\right) - \Phi_\mathrm{R} + \frac{A}{|E_\mathrm{g}|\sqrt{x}} e^{-\Gamma_\mathrm{tl} x} \sin(K_\mathrm{tl} - \phi).} \tag{3.31}$$

In summary, in both cases, the near-field phase can be expressed as

$$\boxed{\Phi_{NF} \approx \phi_\mathrm{g} - \Phi_\mathrm{R} + \frac{A}{|E_\mathrm{g}|\sqrt{x}} e^{-\Gamma_\mathrm{tl} x} \sin(K_\mathrm{tl} - \phi).} \tag{3.32}$$

3.3.4 Perspectives and limits

It should be highlighted that Equations 3.15 and 3.32, while being derived in the context of SPPs on gold, are valid for a much broader range of surface waves. Essentially, any kind of CW (and even PW if the factor $1/\sqrt{x}$ is dropped) interfering with a constant field, with sufficiently small oscillations compared to the constant field, can be approximated by these equations. In the literature, an expression for the amplitude of edge-launched SPPs has been derived [51]. Furthermore, the sinusoidal behaviour of tip-launched SPPs, due to the interference with a constant field, has been assumed [17, 50] to characterize different types of polaritons. The expression of the amplitude of the tip-launched SPPs for a s-SNOM without PsHet detection has also been derived [36]. However, to the best of our knowledge, the expression of the phase of the tip-launched SPPs in the case of a s-SNOM in reflection and with PsHet detection, i.e. Equation 3.32, has not been derived before this work. The derivation of the amplitude and phase provides a better understanding of the s-SNOM signals with PsHet detection and highlights that the dielectric function of the measured material can be deduced both from the measurement of K_tl and L_p^tl, and possibly also from the measurement of the constant offset as in Refs. [53, 86].

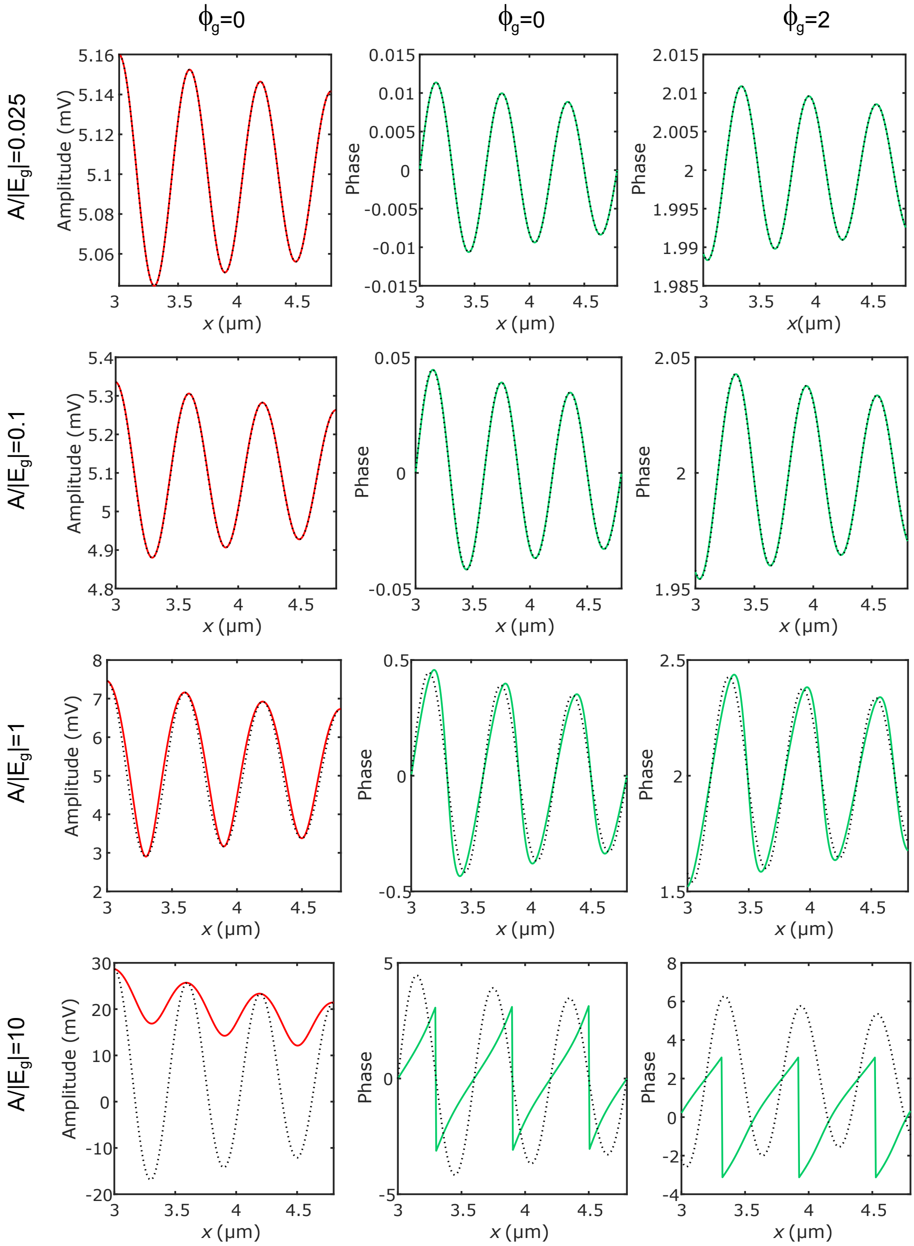

Figure 3.8. Comparison between the exact expressions from Equations 3.10 (plotted in red) and 3.16 (plotted in green), and Equations 3.15 and 3.32 (both plotted as dotted curves) for the amplitude and phase, respectively. For simplification, $\Phi_\mathrm{R} = 0$ and $\phi_\mathrm{p} = 0$. From left to right, all plots in a column have $\phi_\mathrm{g} = 0$, 0, and 2 rad. From top to bottom, all plots in a row have a ratio $\frac{A}{|E_\mathrm{g}|} = 0.025$ (experimental values), $\frac{A}{|E_\mathrm{g}|} = 0.1$, 1, and 10.

Figure 3.8 illustrates what is meant by “sufficiently small” oscillations. The exact expression of the amplitude (in red) and phase (in green) is plotted for different values of the ratio $\frac{A}{|E_\mathrm{g}|}$ and, in the case of the phase, for two different values of the constant phase, $\phi_\mathrm{g} = 0$ and $\phi_\mathrm{g} = 2$. The exact expression is compared to the derived expressions (dashed black curves) of Equations 3.15 and 3.32, for the amplitude and phase respectively. The position x is larger than 3 µm, as the tip-launched SPPs can experimentally isolated from this approximate position. The variables are taken as $\Phi_\mathrm{R} = 0$, $\phi_\mathrm{p} = 0$, $|E_\mathrm{g}| = 5.1$ mV, $L_\mathrm{p}^\mathrm{tl} = 13.5$ µm, $K_\mathrm{tl} = 0.6$ µm^{-1}, and ϕ_g and A are varied. The first line of plots uses a ratio of $\frac{A}{|E_\mathrm{g}|} = 0.025\ \sqrt{\text{µm}}$ (A about 40 times smaller than $|E_\mathrm{g}|$), reflecting the experimental values. No difference can be seen between the exact and approximated expression, which validates the use of Equations 3.15 and 3.32 for our experiments. The second line of plots uses a ratio $\frac{A}{|E_\mathrm{g}|} = 0.1\ \sqrt{\text{µm}}$. In this case too, no difference can be seen between the exact and approximated values. It is only for $\frac{A}{|E_\mathrm{g}|} = 1\ \sqrt{\text{µm}}$ that the differences starts to be visible. For $\frac{A}{|E_\mathrm{g}|} = 10\ \sqrt{\text{µm}}$ (last line), the approximated expressions do not hold anymore, and the amplitude and phase start to look more like the amplitude and phase without interference. In such case, the constant ϕ_g cannot be translated directly in a constant phase offset anymore, as can be seen from the difference between $\phi_\mathrm{g} = 0$ rad (center figure) and $\phi_\mathrm{g} = 2$ rad (right-hand side figure) in the last line. In conclusion, from $x = 3$ µm and up until a ratio $\frac{A}{|E_\mathrm{g}|} = 1$, Equations 3.15 and 3.32 can be used for the determination of the wavelength and propagation length of surface waves measured with a s-SNOM in reflection.

As long as Equations 3.15 and 3.32 hold, both the near-field amplitude and the near-field phase have a sinusoidal behaviour, with a $\pi/2$ phase shift between these two signals. This behaviour is verified in the next section.

3.4 Retrieval of the wavelength and propagation length of SPPs

In the previous sections, a clear tip-launched signal has been isolated, and expressions for the corresponding amplitude and phase signals have been derived. In this section, the retrieved information is used to determine the wavelength and propagation length of SPPs on gold.

3.4.1 Analysis of the tip-launched SPP profiles on gold

Figure 3.9a presents a zoomed-in version of the normalized profiles from Figures 3.5a and 3.6a. Both profiles present the sinusoidal oscillation seen in Section 3.3.1. Furthermore, the phase profile seems to have its oscillations peaks about one fourth of a wavelength later than the amplitude profile. There is thus a phase-shift between the two profiles of about $\pi/2$. The value of this phase shift, as well as the similarities between the amplitude and phase profiles, are confirmed when shifting the phase profile by $-\pi/2$, as shown in Figure 3.9b. The $\pi/2$ phase-shift predicted by the theoretical expressions of Equations 3.15 and 3.32, and mentioned in a previous study [85], is thus confirmed.

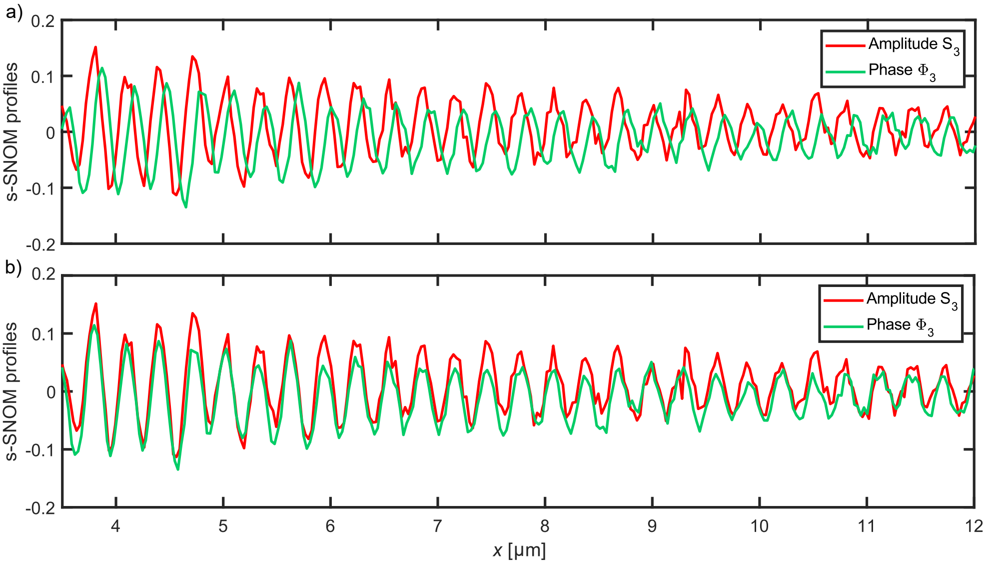

Figure 3.9. Near-field amplitude and phase profiles at grazing incidence angle ($\varphi = -3°$). a) Comparison between the amplitude and phase profiles. b) Same profiles, with the phase shifted by $-\pi/2$. Figures from [66]. ©2022 *Optica Publishing Group under the terms of the Open Access Publishing Agreement.*

Table 3.2 presents the results from fitting the amplitude profile (AP) and phase profile (PP) with Equations 3.15 and 3.32, respectively. The uncertainties correspond to the 95% confidence bound given by the fit. The values of r^2 given by the fit indicate that these equations describe well the experimental profiles. The slightly lower values of r^2 for the phase profile compared to the amplitude profile is attributed to a slight modification of the phase offset at the end of the profile (around $x = 33$ µm). Moreover, all constants retrieved from the fit of the amplitude and phase profiles agree with each other, which gives one more indication that the derived expressions describe the experiment well.

In addition, with the simple expressions derived in Section 3.3, it would be worth considering if the FT of the profiles could also be fitted.

	$\lvert E_\mathrm{g}\rvert$ (mV)	A (mV.$\sqrt{\mathrm{µm}}$)	$\frac{A}{\lvert E_\mathrm{g}\rvert}$ ($\sqrt{\mathrm{µm}}$)	K_tl (µm^{-1})	L_p^tl (µm)	ϕ	$\phi_\mathrm{g} - \Phi_\mathrm{R}$	r^2
AP	$5.0941 \pm 8\ 10^{-5}$	0.126 ± 0.02		20.662 ± 0.003	12.5 ± 0.4	-2.97 ± 0.02		0.99
PP			0.025 ± 0.002	20.674 ± 0.009	11.9 ± 0.3	-2.92 ± 0.08	$1.501 \pm 8\ 10^{-5}$	0.73

Table 3.2. Values of the constants defined for Equations 3.15 and 3.32, obtained by fitting the amplitude profile (AP) and phase profile (PP), respectively, for a starting value $x_b = 4.02$ µm.

3.4.2 Fourier transform of plane and circular waves

Applying the FT to the amplitude and phase profiles has the advantage of displaying the same information as a function of the spatial frequency - here the wavevector K - instead of the position x. This allows to filter out eventual noise, or slowly-varying offset, at other frequencies than the tip-launched peak frequency. Moreover, the resulting tip-launched peak is then displayed in a concise manner, through a single resonance. For PWs, the maximum of the Lorentzian peak can be directly related to the wavelength of the PW, and the width of the peak can be related to the propagation length. In our case, tip-launched plasmons are however CWs. Thus, we consider if it would be possible to do the same for CWs.

There is no exact expression for the one-dimensional FT of a CW expressed as in Equation 3.1, as the CW is diverging like $1/\sqrt{x}$ at $x \to 0$ µm. However, relatively simple expressions can be found using the Mathematica program (from Wolfram Research Inc.), and has been used to find the SPP wavelength on gold in a previous work [87]. For the simplified amplitude profile $|E^\mathrm{S}_\mathrm{NF}|$

$$|E^\mathrm{S}_\mathrm{NF}| = \frac{1}{\sqrt{x}} e^{-\Gamma_\mathrm{tl} x} \cos(K_\mathrm{tl} x), \tag{3.33}$$

the FT is expressed as

$$\mathrm{FT}\{S_3\}(K) = \frac{\sqrt{\frac{\pi}{2}}\sqrt{1 + \sqrt{1 - \frac{K_{tl}^2 {L_p^{tl}}^2}{(i + L_p^{tl} K)^2}}}}{\sqrt{\frac{1}{L_p^{tl}} - iK}\sqrt{1 - \frac{K_{tl}^2 {L_p^{tl}}^2}{(i + L_p^{tl} K)^2}}}. \tag{3.34}$$

This expression is plotted in Figure 3.10a and compared with the discrete Fourier transform of $|E^\mathrm{S}_\mathrm{NF}|$, with x starting at 0.1 µm (dashed curve). Both curves overlap well, and without the necessary truncation of our experimental profiles at x_b, Equation 3.34 could be used as the fitting function of the amplitude peak. However, the tip-launched profiles are truncated at least from $x \approx 2-3$ µm. Because more slow-varying components are present at the beginning of a CW profile, the analytical FT expression is different depending on the truncation starting position x_b. The discrete FT of $|E^\mathrm{S}_\mathrm{NF}|$ with x starting at 3 µm is plotted in Figure 3.10b to illustrate this point. This discrete FT of a truncated CW profile has a peak width smaller than the FT of a CW, but still larger than the FT of a PW. Furthermore, like for the CW FT - and unlike the

Lorentzian shape - the discrete FT of the truncated profile does not fall quickly to zero far from the resonance.

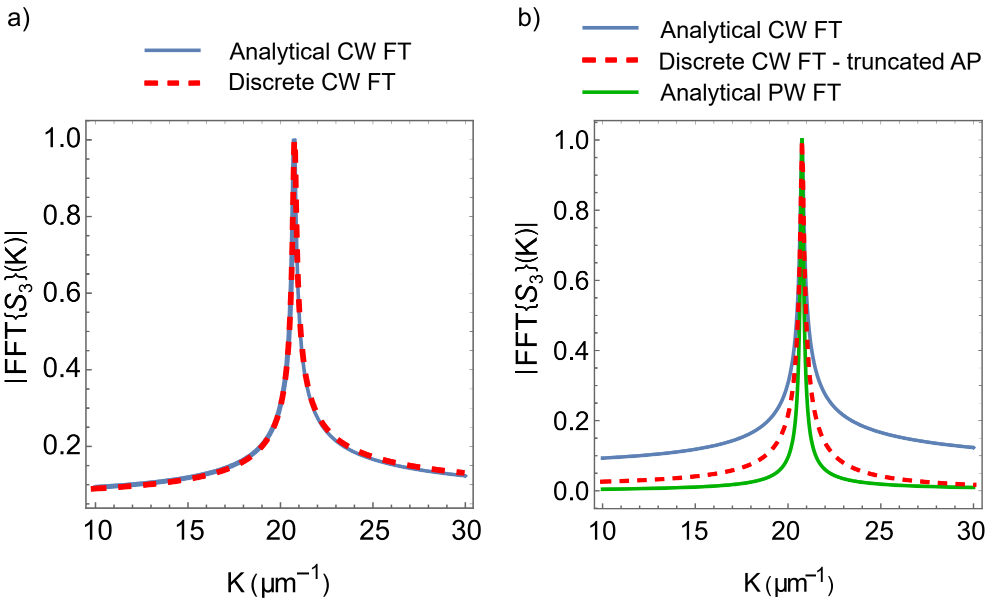

Figure 3.10. Comparison between the analytical expression of the Fourier transform (FT) and the discrete Fourier transform of a CW, calculated with Mathematica. a) Analytical CW FT and discrete CW FT truncated at 0.1 μm. b) Analytical CW FT and discrete CW FT, where the profile in real space has been truncated at 3 μm. The Analytical FT of a PW has been plotted as a comparison. For all the plots, the values of $K_{\mathrm{tl}} = 20.75\ \mu\mathrm{m}^{-1}$ and $L_p^{\mathrm{tl}} = 13.65\ \mu\mathrm{m}$ have been used.

The analytical expression of the FT of the truncated profile of a CW is complicated. Thus, the relation between the peak width and the propagation length is probably not simple. Furthermore, this expression depends on the truncation starting value x_b. Therefore, the fitting of the experimental profiles in Fourier space are done numerically, using the FT of a CW profile, of parameters K_{tl} and L_p^{tl} to determine.

To make the fitting in k-space of the amplitude and phase profiles, the constant in Equations 3.15 and 3.32 are first subtracted, with the values obtained from the real-space fitting. Then, as the FFT algorithm calculates (here spatial) spectra with a resolution limited by the length of the position range: $\Delta K = 2\pi/(x_{\max} - x_{\min})$, the profile is zero-padded, meaning that a vector of zeros is added at the end of the profile vector. The zero padding enables an accurate estimate of the peak heights [88]. As the signal at the end of the amplitude and phase profiles - with the offset subtracted - is negligible compared to the noise, no further information is added when making the profile vector bigger. The FT is then applied to the experimental profile truncated at

x_b. The resulted curve is fitted using the FT of a CW, also truncated at x_b. A small offset accounting for the experimental noise is also added to the fit function.

3.4.3 Wavelength and propagation length on gold

Figure 3.10 presents the CW fit of the tip-launched SPP amplitude (Figure 3.10a) and phase (Figure 3.10b) peaks of the spectra presented in the spectra of Figures 3.5 and 3.6, respectively. In this case, the amplitude and phase profiles were truncated at a value $x_b = 4.02$ µm. The CW fit is compared with the FT of the tip-launched SPP profiles calculated using the dielectric function values from McPeak et al. [77] and Aguilar-Gamma [83] (dashed curve). This theoretical curve overlaps well with the experimental values and the fit.

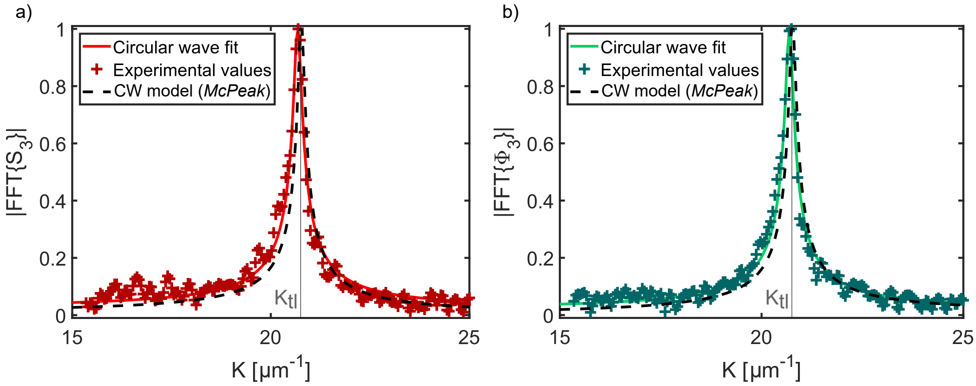

Figure 3.11. Fit of the tip-launched SPP in Fourier space. a) Fit of the amplitude peak visible in the spectrum from Figure 3.5a. b) Fit of the phase peak visible in the spectrum from Figure 3.6a. The “CW model” curve refers to the FT of a CW where the dielectric functions from McPeak et al. [77] and Aguilar-Gama et al. [83] have been used for the gold flake and the Al_2O_3 film, respectively. Figures from [66]. ©2022 *Optica Publishing Group under the terms of the Open Access Publishing Agreement.*

For a more quantitative comparison, the values of the wavevector K_{tl} and propagation length $L_{\mathrm{p}}^{\mathrm{tl}}$ extracted from the fit are compared with the theoretical ones. These values are presented in Table 3.3. All the extracted values of K_{tl} and $L_{\mathrm{p}}^{\mathrm{tl}}$ agree with each other. K_{tl} has however a slightly smaller value than determined with the values from McPeak et al., and the propagation length is slightly shorter.

One possible reason for this discrepancy could be that the fit is slightly unstable with regards to the choice of x_b. It could be that the noise at x_b influences the estimation of the starting amplitude of the oscillations, and thus the determination of the propagation length, in particular. To verify that the fit is stable, the same fitting procedure is applied for 30 different values of x_b, from $x_b = 3.42$ µm to $x_b = 4.32$ µm. These values of x_b have been chosen to be sufficiently far from the platelet's edge so

	Amplitude profile		**Phase profile**		**McPeak *et al.***
	k-space	Real space	k-space	Real space	
K_{tl} (µm^{-1})	20.658 ± 0.009	20.662 ± 0.003	20.674 ± 0.007	20.674 ± 0.009	20.75
$L_{\mathrm{p}}^{\mathrm{tl}}$ (µm)	12 ± 1	12.5 ± 0.4	12 ± 1	11.9 ± 0.3	13.65

Table 3.3. Comparison of values for the wavevector $K_{\mathrm{tl}} = 2\pi/\Lambda_{\mathrm{tl}}$ and propagation length $L_{\mathrm{p}}^{\mathrm{tl}}$, as obtained in real space and in Fourier space, for one starting value x_b. Table from [66]. ©2022 *Optica Publishing Group under the terms of the Open Access Publishing Agreement.*

that the tip-launched signal is isolated, but also sufficiently close to the edge to have enough tip-launched signal for a precise fit. The average values and 95% confidence bounds are calculated for all the fits, and summarized in Table 3.4. As the values remain the same, we conclude that the fitting is stable with regards to the choice of x_b.

	Amplitude profile		**Phase profile**		**Theory**
	k-space	Real space	k-space	Real space	
K_{tl} (µm^{-1})	20.65 ± 0.01	20.662 ± 0.003	20.67 ± 0.01	20.67 ± 0.01	20.75
$L_{\mathrm{p}}^{\mathrm{tl}}$ (µm)	11.3 ± 0.8	12.5 ± 0.7	11.6 ± 0.7	12.1 ± 0.7	13.65

Table 3.4. Comparison of values for the wavevector and propagation length, as obtained in real space and in Fourier space, for an average of 30 different starting values. Table from [66]. ©2022 *Optica Publishing Group under the terms of the Open Access Publishing Agreement.*

Another possible reason could be that the tabulated values taken to compare with the experiments are different from the experimental dielectric function. This could be the case with the Al_2O_3, for which the values of dielectric function is taken from a layer of 50 nm deposited by ALD [83]. The same study highlights that the dielectric function for such thin layers depend of the thickness of Al_2O_3.

It should also be highlighted here that the values of the uncertainties associated with K_{tl} and $L_{\mathrm{p}}^{\mathrm{tl}}$ are the uncertainties of the fit, and do not correspond to a global uncertainty of any experimental characterization of the tip-launched SPPs. A possible additional source of uncertainty - not taken into account in Tables 3.3 and 3.4 - could actually come from the AFM positioning itself. Two additional measurements - made on the same gold platelet eight months after the measurement presented in this section - are provided in Appendix C. These measurements give values of K_{tl} and $L_{\mathrm{p}}^{\mathrm{tl}}$ that are consistent with the values presented in Tables 3.3 and 3.4. There are however some slight differences that seem to confirm that some larger uncertainties, probably due to the AFM positioning, are involved. An evaluation of the global uncertainty can be made by calculating the variance over many different measurements on the same gold platelet.

3.5 Summary

In this Chapter we have demonstrated that selecting the near-field amplitude and phase information far from the edges of a monocrystalline gold platelet and with a grazing angle between the incident light and the edge enables to isolate the tip-launched SPPs in a clear manner. This method works well, as long as the propagation length $L_{\mathrm{p}}^{\mathrm{tl}}$ is longer than two times the region where the edge SPPs are dominant. We derived expressions for the resulting amplitude and phase of the tip-launched SPPs interfering with the light directly reflected from the gold towards the tip. These expressions describe the experimental profiles well and are consistent with the $\pi/2$ phase-shift between the amplitude and phase. With these expressions, we retrieved for the first time to our knowledge both the wavelength $\Lambda_{\mathrm{tl}} = 304.0$ nm and the propagation length $L_{\mathrm{p}}^{\mathrm{tl}} = 12$ µm, with a s-SNOM in a reflection configuration. The SPP wavelength has thus been determined to be $\Lambda_{\mathrm{SPP}} = 608.0$ nm, and the field propagation length $L_{\mathrm{p}}^{\mathrm{SPP}} = 24$ µm. Among the different values of the gold dielectric function, it has been found that the values from McPeak et al. seem to correspond better to our experimental values than other tabulated values of the dielectric function do [73, 76], even though it is polycrystalline gold. For this reason, a recent work [10] suggested that the ultimate limit for losses in gold has been reached. These values were found to be stable in time, as measurements of the same gold platelet eight months after the presented experiment (see Appendix C) gave the same results.

With these tools in hand, we could in principle characterize the wavevector of any kind of polaritons in the visible range. This could be particularly interesting in the case of some van der Waals materials such as transition metal dichalcogenides (TMDCs), which host strong excitons in the visible range and could thus show SPP to exciton coupling. In the following chapters, TMDCs materials placed on top of the gold platelets are therefore studied both theoretically and experimentally.

CHAPTER 4

Coupling between excitons and SPPs

Van der Waals materials are layered materials where each layer is held together by covalent bonds, but the different layers are held by weak van der Waals forces. This family of materials attracted a lot of interest with the exfoliation of graphene with scotch tape in 2004 [89]. Soon after, a large number of other materials with new properties were synthesized, and many more are expected to be stable in their 2D form [90, 91]. In particular, the TMDCs host strong excitons that can interact with cavities, waveguides, and other structures. In this work, we focus on coupling with SPPs propagating at the surface of the gold platelets studied in Chapter 3.

In this chapter, the optical properties of excitons in TMDCs are presented in Section 4.1. These properties are well-described by the optical dielectric function which is introduced in the Section 4.2. The dielectric function is used in light-matter interaction models that can assess the coupling between an emitter and a cavity. In Section 4.3, the different coupling regimes are described, with a focus on the SPP-TMDC coupling. The theoretical dispersion relation for the SPP-TMDC coupling is then calculated with the help of the TMM and described in Section 4.4. A correction to the calculation of the TMM taking into account the anisotropy of the TMDCs is then introduced, and the resulting dispersion relation is presented in Section 4.5.

4.1 Excitons in transition metal dichalcogenides

TMDCs are a group of layered crystals composed of transition metal and chalcogen atoms. These materials have been studied for a long time in their layered form [92–94]. Monolayers of these materials can be exfoliated in the same way as graphene [89]. Indeed, just like graphite, TMDCs are part of the van der Waals materials: the atoms in each layer are held together by covalent bonds, but the different layers are held by weak van der Waals forces. This property makes them easy to separate by exfoliation. Furthermore, the absence of covalent bonds between the layers means that they are naturally passivated, which makes them easy to integrate with other photonic structures [37].

TMDCs are most often found in the form MX_2, where M is the metal and X is the chalcogen. To date, the most studied ones have M = Mo or W and X = S, Se or Te [37, 41, 42, 53, 95–98]. Their thermodynamically most stable crystal structure is the trigonal prismatic (2H) phase. In a monolayer of the 2H structure seen from the top, the M and X atoms are alternated to form a hexagonal lattice (see Figure 4.1a). Seen from the side, the M atom is sandwiched between two layers of chalcogens X, with the X atoms on top of each other, as represented in Figure 4.1b. In the case of a bilayer, the second layer is rotated by 180° and the M atom is placed on top of the X atom, as shown in Figure 4.1b.

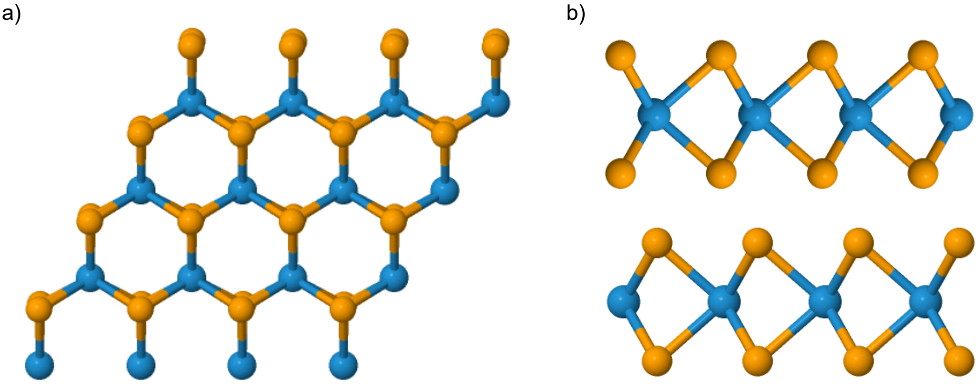

Figure 4.1. Atomic structure of the 2H phase of a generic TMDC. a) Top view. b) Side view. The structures are taken from the C2DB database [90, 91].

Among other interesting properties, TMDCs are famous for hosting excitons at room temperature [37]. Excitons are quasi-particles formed after excitation of an electron from the valence band (VB) to the conduction band (CB) of a semiconductor material. The formation process of excitons in a generic direct-bandgap material is shown in Figure 4.2a. The electron e^- is first excited with an energy higher than the bandgap energy E_g, leaving a hole h^+ in the VB (process **1** in the figure). The electron and hole then relax at the bottom of the CB and the top of the VB, respectively (process **2**). The electron and hole have opposite charges and are formed at the same position in the crystal lattice. This means they can bind through Coulomb interaction and form an exciton [72], thus effectively lowering the energy E_{exc} of the bound electron-hole pair (process **3**).

Excitons can be separated in two categories. The *Frenkel* excitons are tightly bound to specific atoms or molecules in the lattice and have binding energies of 0.1-1 eV [72]. Because of their high binding energy, they are not easily destroyed by collisions with thermally excited phonons of energy of the order of $k_B T \approx 0.026$ eV, where k_B is the Boltzmann's constant and $T \approx 300$ K is the room temperature. By contrast, the *Wannier-Mott* excitons are delocalized and typically have binding energies lower than $k_B T$ in bulk materials and at room temperature. However, the 2D nature of TMDCs has the effect of reducing the electronic screening of the interaction between the electron and the hole [41] (see Figure 4.2b). Thus, strong excitons can be formed at room temperature, and even their excited states can influence the optical properties of TMDCs [41, 42].

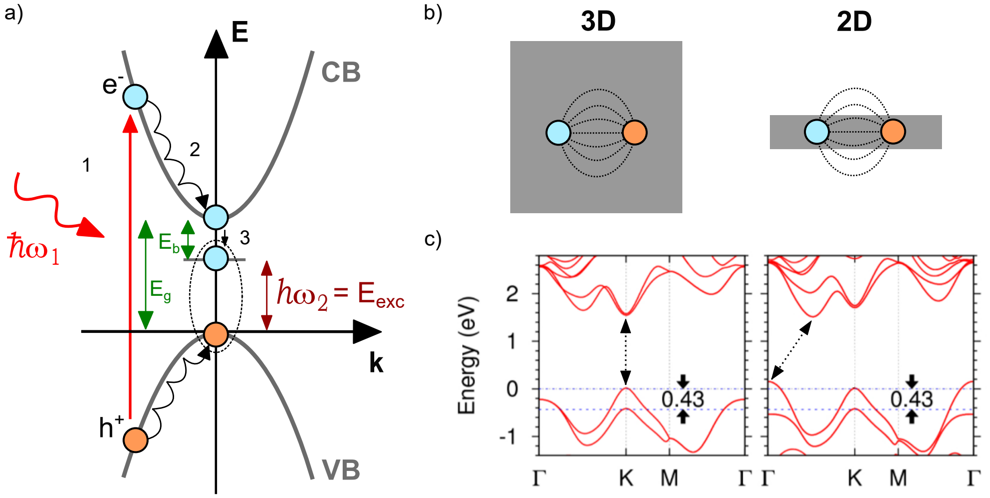

Figure 4.2. Excitons in TMDCs. a) Excitonic states and exciton formation in the two-level model. b) Environment of the excitons in a bulk material (left) compared to an atomically thin structure such as TMDCs (right). The dashed lines represent the Coulomb interaction field lines. Because the dielectric function in the material is higher than outside the material, screening between the electron and the hole is reduced. c) Bandgap of WS_2 for a monolayer (left) and a bilayer (right). The dashed double arrow highlights the direct (left) and indirect (right) bandgap. Figure from Ref. [95].

The band diagram of a typical monolayer and bilayer of a TMDC (in this case WS_2) is presented in Figure 4.2c. As the diagram shows, TMDCs are semiconductors, with a bandgap energy of about 1-2 eV at the K-point. For a monolayer, the bandgap is direct. However, as soon as a second layer is added, the bandgap becomes indirect (see Figure 4.2c). This effect has drastic consequences on the photoluminescence properties of the TMDCs, as the photoluminescence intensity of TMDCs can be one to two orders of magnitude smaller for a bilayer than for a monolayer [95]. The reason for this effect is that the luminescent process in an indirect bandgap needs to be a phonon-assisted process to conserve the momentum of the initial and final states [72].

The splitting of the VB at the K-point has been shown to correspond to the effect of the spin-orbit coupling [95]. The transitions associated with the higher band at the K-point corresponds to the A-exciton, while the one associated with the lower band corresponds to the B-exciton. The excitons associated with the higher energies follow the alphabetic order [99].

The excitonic optical properties of the TMDCs can be described by the dielectric function of the TMDCs, as is explained in the next section.

4.2 Optical dielectric functions of transition metal dichalcogenides

The relative permittivity, here called optical dielectric function, efficiently describes the absorption and transmission processes of light when interacting with matter [72]. The precise characterization of the dielectric function is therefore crucial, as it determines the way materials interact with light.

For dielectric and semiconductor materials, the dielectric function can be described by the Lorentz model

$$\varepsilon_{TMDC}(E) = \varepsilon_\infty + \sum_{i=1}^{N} \frac{f_i}{E_i^2 - E^2 - i\gamma_i E}, \tag{4.1}$$

where ε_∞ is the dielectric function at energies higher than the measurement window, f_i is the oscillator strength of the resonance i ($i \in [1, N]$), E_i is the resonance energy and γ_i is the resonance's damping factor.

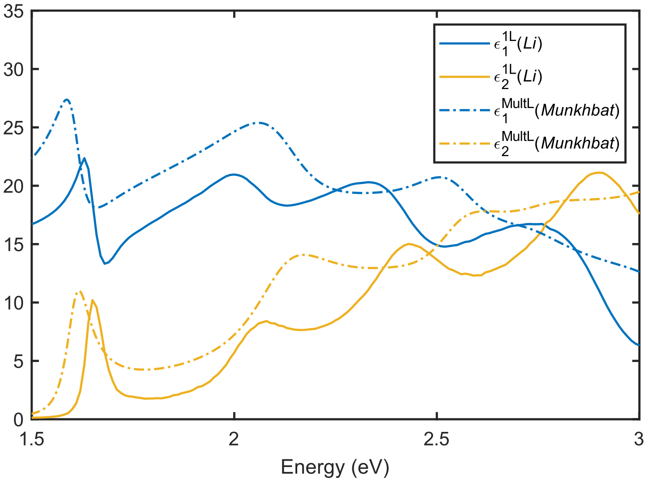

Figure 4.3. Measured real (ε_1) and imaginary (ε_2) parts of the dielectric function of WSe$_2$, for in-plane field polarization (i.e. s-polarisation) and for a monolayer (1L) and a multilayer (MultL) of several hundreds of nanometer thickness. Data taken from [100] for the monolayer and [43] for the multilayer.

The in-plane dielectric function of TMDCs has been measured as early as 2014 for monolayer TMDCs [100]. Figure 4.3 shows the aforementioned dielectric function in the case of WSe_2. A resonance at 1.65 eV corresponding to the A-exciton can be seen. Since then, researchers have investigated new ways to determine the dielectric function without *a priori* knowledge of electronic transitions outside of the spectral range of the measurement [101]. The influence of the number of layers on the dielectric function of TMDCs has also been studied, experimentally and theoretically [99, 102]. According to these works, the A-exciton is red-shifted when increasing the number of layers. This effect has been attributed to the mutual contractions of the CBs and the VBs as WSe_2 becomes thicker [99]. The same behaviour can be seen when comparing the monolayer dielectric function from Li et al. [100] with the multilayer dielectric function from Munkhbat et al. [43].

Recently, even near-field methods have been used to determine the dielectric function of monolayer WSe_2 and $MoSe_2$ and their heterostructures [53].

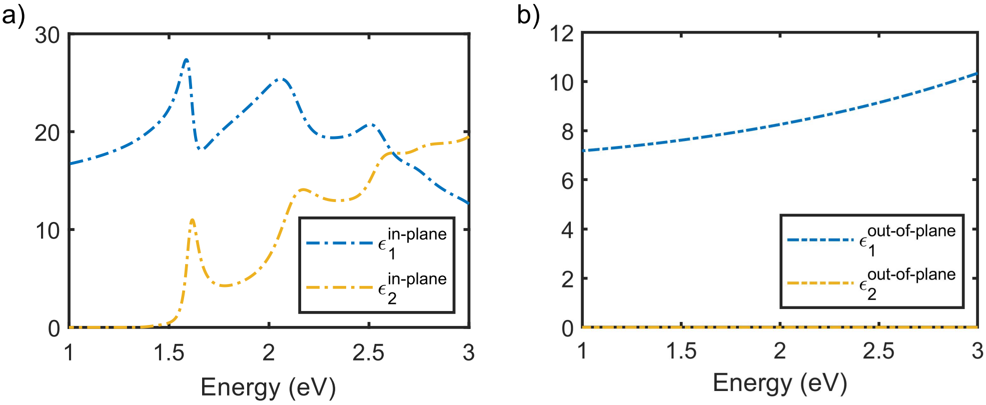

Figure 4.4. Measured real (ε_1) and imaginary (ε_2) parts of WSe_2 for a) in-plane and b) out-of-plane polarizations. Data taken from Ref. [43].

However, due to the intrinsic anisotropy of these layered van der Waals materials, the in-plane and out-of-plane dielectric functions are different. This property has been acknowledged from the first measurements of the dielectric function [99–101]. However, at first, the out-of-plane dielectric functions was not measured because of the experimental configuration did not allow to access it [100]. Later, it was argued that the effect of anisotropy could be resolved only when the layer thickness exceeded a few tens of nanometers [103, 104].

Measurements of in-plane and out-of-plane dielectric functions by using nano-FTIR spectroscopy were reported in 2020 for WSe_2 in the mid-infrared, revealing a strong anisotropy of this TMDC [105]. In 2021, ellipsometry measurements reaching the visible range were performed for thin-film MoS_2 and highlighted the anisotropy of this material [44, 104]. This strong anisotropy was corroborated by s-SNOM measurements on MoS_2 [44] and on WS_2 [106]. These findings were confirmed by an extensive study of both in-plane and out-of-plane components for ten different multilayer TMDCs which has been recently carried out for a wide spectral range by ellipsometry [43]. The results for the case of WSe_2 are presented in Figure 4.4. The anisotropy can clearly be seen by comparing the in-plane dielectric function in Figure 4.4a and out-of-plane dielectric function in 4.4b. Indeed, the real part of the dielectric function is about twice larger in-plane than out of plane, and the imaginary part is practically vanishing for the out-of plane dielectric function, while taking values up to 20 at 3 eV for the in-plane one.

Following the available data and the thin-layer argument, some predictions seem to have only taken the in-plane dielectric function into account when calculating the light-TMDCs interactions [52, 107–109]. However, while the anisotropy in TMDCs such as WSe_2 is likely not important when working with s-polarized light, it potentially becomes important for excitation with p-polarization and coupling with SPPs, and in the case of thicker layers of TMDCs. The magnitude of this inaccuracy is investigated in Section 4.5.

4.3 Light-matter coupling and the coupled-oscillator model

The previous sections highlighted the optical properties of the TMDCs. These properties can be modified by changing the environment around it.

Modifications of emitters' properties through their environment was first formalized in the framework of cavity quantum electrodynamics (QED) [110]. In this framework, an emitter can optically couple with a cavity if these two components spatially and spectrally overlap. In such a case, the behavior of the coupled system does not only depend on the individual properties of the emitter and cavity, but also on their coupling.

The optical response of the emitter-cavity system can take different forms depending on the value of the coupling strength g. Two main coupling regimes can be distinguished: the weak- and the strong-coupling regime. In the weak-coupling regime, the emission rate of the emitter can be modified. Depending on the position and direction of the emitter with regards to the cavity, the rate can be decreased or increased, leading to an enhancement or reduction of the emitter luminescence, respectively [2]. The magnitude of this effect is typically quantified with the ratio between the decay rate of the emitter in the cavity and the decay rate in free space, i.e. the Purcell factor. In the strong-coupling regime, the cavity and the emitter interact so strongly that the emitted photon can be reabsorbed before escaping the cavity. In such a case, the emitter and photon populations oscillate in time until the photon leaves the cavity. There is a coherent exchange of energy between the emitter and the cavity at a rate defined as the Rabi oscillation frequency Ω_R. This effect leads to two new hybrid modes characterized by an energy splitting of $\hbar\Omega_R$. The strong coupling can theoretically be described by considering the coupling between two harmonic oscillators and by using a framework than can be either classical, semi-classical, or fully quantum mechanical [111]. All models give the same prediction for the size of the splitting. In this thesis, only the classical approach has been considered.

In this work, we are considering the coupling between propagating SPPs and excitons in TMDCs. The coupling between these two entities can be described with the coupled-oscillator model (COM). In this model, the coupling between a classical field and a Lorentzian oscillator is considered, in a frequency range close to the resonance frequency of the Lorentzian oscillator and far from the SPP plasma frequency. Within the COM framework, and if damping is neglected, the frequencies of the two hybrid modes can be described as [107, 111]

$$\omega_{\pm}(q) = \frac{\omega_{\mathrm{spp}}(q) + \Omega_{\mathrm{exc}}}{2} \pm \frac{1}{2}\sqrt{(\omega_{\mathrm{spp}}(q) - \Omega_{\mathrm{exc}})^2 + \Omega_{\mathrm{R}}^2} \tag{4.2}$$

where q is the in-plane wavevector, $\omega_{\mathrm{spp}}(q)$ is the frequency of the SPP dispersion without the emitter's resonance, $\hbar\Omega_{\mathrm{exc}}$ is the exciton energy and $\hbar\Omega_{\mathrm{R}}$ is the energy of the splitting, called Rabi splitting energy.

Experimentally, it is considered that the strong-coupling regime starts when the energy splitting $\hbar\Omega_{\mathrm{R}}$ is larger than the average full widths at half maximum of the emitter and cavity,

$$\hbar\Omega_{\mathrm{R}} > \frac{1}{2}(\Gamma_{\mathrm{spp}} + \Gamma_{\mathrm{exc}}), \tag{4.3}$$

where Γ_{spp} and Γ_{exc} are the losses from the SPPs and from the excitons, respectively.

Gonçalves et al. [107] predicted that the transition towards strong coupling between excitons and SPPs could be observed for a TMDC (in their case a monolayer of WS_2) placed on top of a gold surface. However, the splitting could be visible only if a material with high dielectric function were placed above the TMDC. In this work, we decided to use the TMDC itself as the material with high dielectric function to place directly on top of the platelets studied in Chapter 3. For a thin layer of TMDC, the confinement of the SPPs might be lower than for the semi-infinite layer of dielectric material considered in Ref. [107]. However, the signal from the plasmon-exciton polaritons is thereby easier to obtain, as the tip can scan directly above the TMDC.

The multilayer structure to be considered is thus composed of (from top to bottom) air, TMDC, aluminum oxide, and gold. As, to our knowledge, there is no analytical expression for the coupling strength of such a multilayer structure, we here characterized the coupling by calculating numerically the dispersion relation of the structure by using the transfer matrix method. In our framework, the excitonic resonance is treated through the dielectric function of the TMDCs.

4.4 Theoretical dispersion relation with plasmon-exciton coupling

As mentioned in the previous section, the structure considered in this work is a stratified structured composed not only of a gold platelet hosting the SPPs and of a TMDC hosting the excitons. Indeed, there is also a 2-nm layer of aluminum oxide between the gold platelet and the TMDC, and air, as the experiments take place in ambient conditions.

In this section, the transfer matrix method is derived and is used to predict the dispersion relation of excitons in WSe_2 interacting with SPPs on monocrystalline gold platelets.

4.4.1 The transfer matrix method

The transfer matrix method (TMM) relates the field components at two different positions of a stratified medium, by using a matrix formalism. It has proven to be a powerful and flexible method for the calculation of light propagation in different layered structures [112, 113].

The main idea of the TMM is to describe the stratified medium by elementary matrices that can be separately calculated and multiplied to give the total reflected and transmitted fields as a function of a given incident field. In this section, the derivation of the TMM in the case of *p*-polarized light is presented, as it is corresponding to the polarization of SPPs at an air/metal interface. The derivation is based on references [112] and [114]. As a note, any homogeneous layer of the stratified medium is considered as isotropic in this derivation. The anisotropic case is presented in Section 4.5.2.

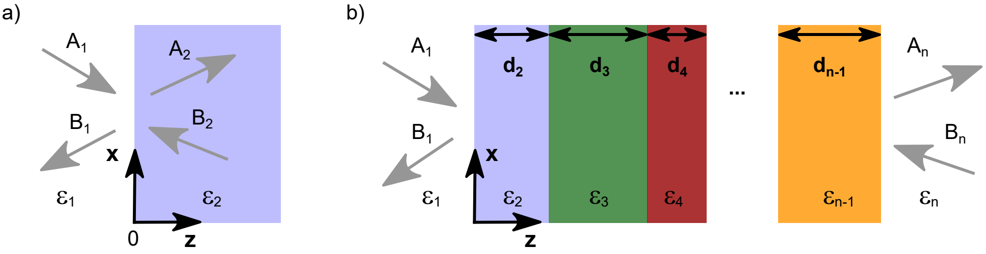

Figure 4.5. Geometries of the structures for which the TMM can be used. a) Case of a single interface. A field impinges at an interface between two materials of dielectric function ε_1 and ε_2. b) Case of several interfaces. A field impinges on a structure made of several layers having each thickness d_i and a dielectric function ε_i ($i \in \mathbb{N}^*$). A_i and B_i represent the field components in medium i.

To understand where the elementary matrices come from, we first consider the interface between two materials of dielectric functions ε_1 and ε_2 (that is called media 1 and 2 for simplification). The structure and the associated field components are represented in Figure 4.5a. For p-polarization, the magnetic field along y can be expressed as

$$H_{1y} = (A_1 e^{ik_{1z}z} + B_1 e^{-ik_{1z}z}) e^{iqx} e^{-i\omega t}, z < 0 \tag{4.4a}$$

$$H_{2y} = (A_2 e^{ik_{2z}z} + B_2 e^{-ik_{2z}z}) e^{iqx} e^{-i\omega t}, z > 0 \tag{4.4b}$$

where $A_i, B_i (i \in \{1,2\})$ are the magnetic field components for the forward and backward propagating fields, respectively, in media 1 and 2. $q(k_{iz})$ are the $x(z)$ components of the wavevector $k_i = \sqrt{\varepsilon_i}\omega/c$.

In the absence of current distributions at the surface, the boundary conditions for the magnetic field $\mathbf{H}_i$ and electric field $\mathbf{E}_i$ at $z = 0$ can be written as [112, 114]

$$\hat{\mathbf{n}} \times (\mathbf{H}_2 - \mathbf{H}_1) = 0 \tag{4.5}$$

$$\hat{\mathbf{n}} \times (\mathbf{E}_2 - \mathbf{E}_1) = 0 \tag{4.6}$$

where $\hat{\mathbf{n}}$ is the unit vector normal to the surface. This means that in the case of p-polarization, $H_{1y} = H_{2y}$ and $E_{1x} = E_{2x}$. Using these boundary conditions and the Maxwell's equation

$$\nabla \times \mathbf{H}_i = \varepsilon_0 \varepsilon_i \frac{\partial \mathbf{E}_i}{\partial t} \tag{4.7}$$

gives the equations

$$A_1 + B_1 = A_2 + B_2, \tag{4.8}$$

$$\frac{k_{1z}}{\varepsilon_1}(A_1 - B_1) = \frac{k_{2z}}{\varepsilon_2}(A_2 - B_2), \tag{4.9}$$

Hence, in the case of p-polarized light and at the interface between the isotropic media 1 and 2, the relationship between the field components can be described as

$$\begin{pmatrix} A_1 \\ B_1 \end{pmatrix} = D_{12} \begin{pmatrix} A_2 \\ B_2 \end{pmatrix}, \tag{4.10}$$

where the transmission matrix D_{12} is

$$D_{12} = \frac{1}{2} \begin{pmatrix} 1 + \frac{\varepsilon_1 k_{2z}}{\varepsilon_2 k_{1z}} & 1 - \frac{\varepsilon_1 k_{2z}}{\varepsilon_2 k_{1z}} \\ 1 - \frac{\varepsilon_1 k_{2z}}{\varepsilon_2 k_{1z}} & 1 + \frac{\varepsilon_1 k_{2z}}{\varepsilon_2 k_{1z}} \end{pmatrix}. \tag{4.11}$$

In addition, when considering a homogeneous and isotropic medium of dielectric function ε_i, the relationship between the amplitude coefficients at a distance z and at a distance $z + d_i$ can be written as

$$\begin{pmatrix} A_i(z) \\ B_i(z) \end{pmatrix} = P_i \begin{pmatrix} A_i(z + d_i) \\ B_i(z + d_i) \end{pmatrix}, \tag{4.12}$$

with the propagation matrix P_i defined as

$$P_i = \begin{pmatrix} e^{-ik_{iz}d_i} & 0 \\ 0 & e^{ik_{iz}d_i} \end{pmatrix}, \text{ with } k_{iz} = \sqrt{\varepsilon_i \frac{\omega^2}{c^2} - q^2}. \tag{4.13}$$

If we now consider n interfaces, as represented in Figure 4.5b, the relationship between the input and output fields can be calculated through the elementary matrices using the total matrix M, with

$$\begin{pmatrix} A_1 \\ B_1 \end{pmatrix} = M \begin{pmatrix} A_n \\ B_n \end{pmatrix}, \text{ and } M = D_{12}P_2D_{23}P_3D_{34}P_4...P_{n-1}D_{(n-1)n}. \tag{4.14}$$

The associated reflection and transmission coefficients can be deduced using the relations

$$r_{1n} = \left.\frac{B_1}{A_1}\right|_{B_n=0} = \frac{M_{21}}{M_{11}} \tag{4.15}$$

and

$$t_{1n} = \left.\frac{A_n}{A_1}\right|_{B_n=0} = \frac{1}{M_{11}} \tag{4.16}$$

where $M_{ij}(\{i,j\} \in \{1,2\})$ are the elements of M and $|_{B_n=0}$ means that that the field component B_n is set to zero (recall Figure 4.5b).

It should be noted that the amplitude coefficients A_i and B_i are the coefficients associated with the magnetic field $\mathbf{H}_i$ ($i \in \mathbb{N}^*$). To retrieve the reflection and transmission coefficients for the electric field, the duality principle can be used [114, p. 176]. This principle connects the values of the electric and the magnetic fields through the impedance in medium i, Z_i, such as

$$\hat{\mathbf{k}}_i \times \mathbf{E}_i = Z_i\mathbf{H}_i \text{ with } Z_i = \sqrt{\frac{\mu_0\mu_i}{\varepsilon_0\varepsilon_i}}, \tag{4.17}$$

where $\hat{\mathbf{k}}_i$ is the unit vector in the same direction as the wavevector $\mathbf{k}_i$ in the medium i. From Equation 4.17, it can be deduced that the reflection coefficient for the electric field remains the same as Equation 4.15. However, the transmission coefficient for the electric field t^E_{1n} relating the input electric field component A^E_1 and the transmitted electric field component A^E_n becomes

$$t^E_{1n} = \left.\frac{A^E_n}{A^E_1}\right|_{B^E_n=0} = \frac{1}{M_{11}}\frac{Z_n}{Z_1}. \tag{4.18}$$

The TMM thus provides a simple way to decompose an initially complex problem into elementary bricks and obtain physical coefficients out of it. In the particular case of evanescent fields such as SPPs, the condition for their existence can be derived by finding the poles of the reflection coefficient [112].

4.4.2 Theoretical dispersion relation for evanescent waves in a multilayer structure

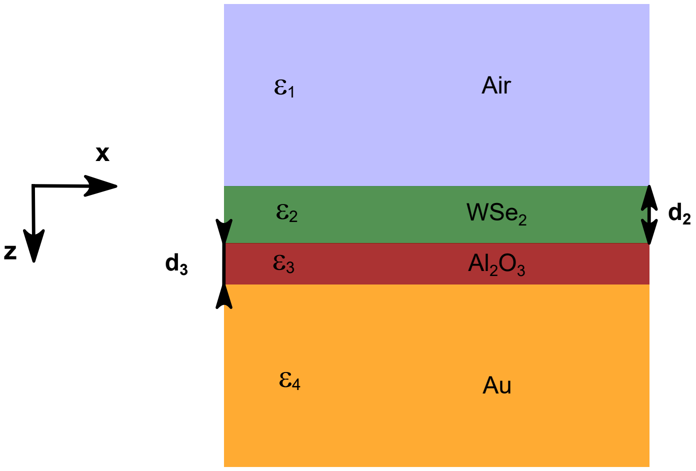

Figure 4.6. Sketch of the multilayer structure used in the experiments and for which the theoretical dispersion relation is calculated. From top to bottom, there is air of dielectric function $\varepsilon_1 = 1$, WSe_2 of dielectric function $\varepsilon_2 = 25 + 1.6i$ at 800 nm and thickness d_2, Al_2O_3 of dielectric function $\varepsilon_3 = 2.59$ and thickness $d_3 = 2$ nm, and gold (Au) of dielectric function $\varepsilon_4 = -27 + 1.1i$ at 800 nm.

The structure that is used in the near-field measurements of SPPs interacting with the excitons in WSe_2 is represented in Figure 4.6. The bottom layer (Au) is consisting of the monocrystalline gold platelets studied in Chapter 3. It is considered as semi-infinite, as the platelets are thick enough to neglect hybridization with a SPP mode propagating at the substrate/gold interface (not shown in the Figure 4.6), and it has a complex dielectric function ε_4. The gold platelets are covered with a thin layer of aluminum oxide (Al_2O_3) of dielectric function ε_3 and of fixed thickness $d_3 = 2$ nm, also present in the structures from Chapter 3. On top of the Al_2O_3 is WSe_2, of dielectric function ε_2 and of thickness d_2. As the sample and s-SNOM are in air, the top semi-infinite layer has a dielectric function $\varepsilon_1 = 1$.

The Matlab programs used to calculate the dispersion relation are given in Appendix D. In a nutshell, the goal of the programs is to find the in-plane wavevector q that satisfies the condition for the existence of evanescent fields for a given photon energy E. To do so, it uses the dielectric functions found in the literature for ε_2 [43], fitted with 10 Lorentz oscillators, ε_3 [83] (taken as a constant equal to 2.59) and ε_4 [77] and the thickness d_2 and d_3 to calculate the total matrix

$$M(q) = D_{12}(q)P_2(q)D_{23}(q)P_3(q)D_{34}(q). \tag{4.19}$$

Then, the condition for the existence of evanescent waves can be found by calculating the poles of the reflection coefficient, with the equation

$$M_{11}(q) = 0. \tag{4.20}$$

This equation is numerically solved for each value of the energy E in a range from 1.5 to 1.7 eV. The dispersion relation is then plotted as the $(q,\, E)$ pair found for each photon energy E.

It should be noted that finding the solutions to Equation 4.20 is not an easy task, even numerically. Indeed, the full complex values for the dielectric functions are needed here, meaning that the solution q is also to be found in the complex plane. To help the calculations, one can notice that the out-of-plane component of the wavevector k_{iz} is purely imaginary, as $k_{iz}^2 = \varepsilon_i \frac{\omega^2}{c^2} - q^2$ is negative in the case of evanescent fields such as SPPs. To help the program calculate, we can thus define:

$$k'_{iz} = k_{iz}/i = \sqrt{q^2 - \varepsilon_i \frac{\omega^2}{c^2}} \tag{4.21}$$

meaning also that P_i is consequently modified such as

$$P'_i = \begin{pmatrix} e^{k'_{iz} d_i} & 0 \\ 0 & e^{-k'_{iz} d_i} \end{pmatrix}. \tag{4.22}$$

Furthermore, following the continuity principle, once the solution for q is found for the first energy (1.5 eV), the initial guess for the next value of q is the solution from the previous iteration.

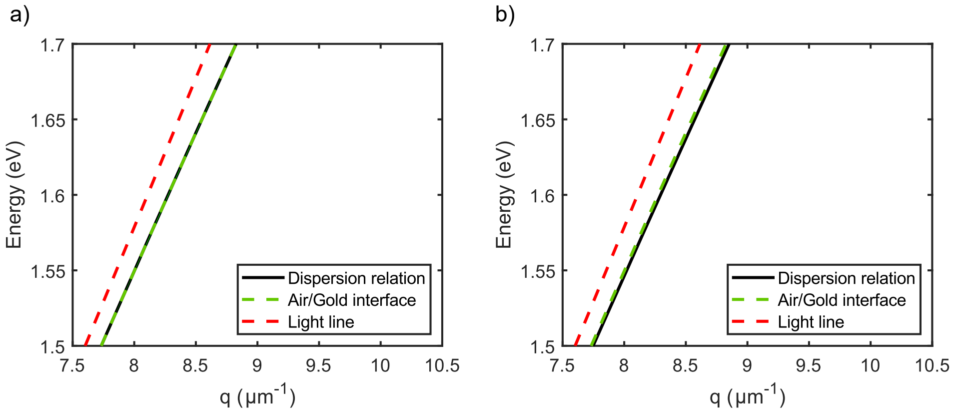

Figure 4.7. Calculated dispersion relation for the structure presented in Figure 4.6, with a) $d_2 = 0$ nm of WSe$_2$ and $d_3 = 0$ nm of Al$_2$O$_3$ and b) $d_2 = 0$ nm of WSe$_2$ and $d_3 = 2$ nm of Al$_2$O$_3$.

To benchmark the limiting behaviour of the model, the dispersion relation is plotted for a thickness of WSe$_2$ of $d_2 = 0$ nm and a thickness of Al$_2$O$_3$ of $d_3 = 0$ nm (see Figure 4.7a). The result is compared with the dispersion relation of the air/gold interface (dashed green line in Figure 4.7a). The two curves overlap perfectly, so the model has the correct limiting behaviour. Moreover, the effect of the 2-nm layer of Al_2O_3, still without WSe_2, is tested is Figure 4.7b. A slightly higher confinement can be seen Figure 4.7b compared to Figure 4.7a, due to the addition of the Al_2O_3 layer.

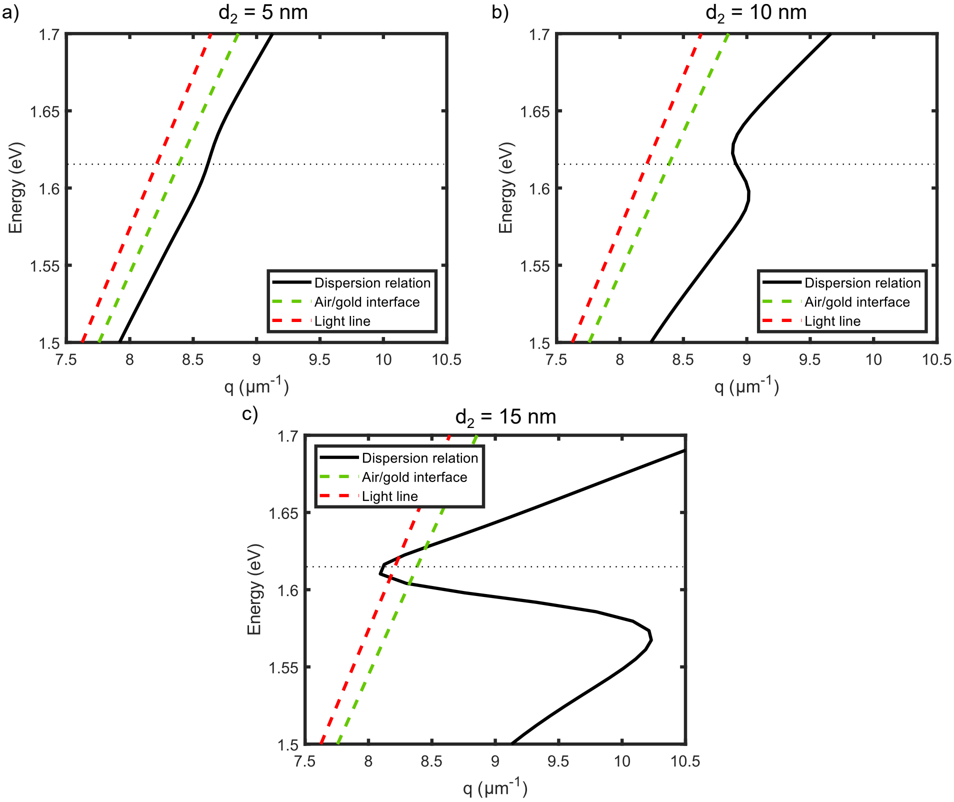

Figure 4.8. Calculated dispersion relation for the structure presented in Figure 4.6, when considering WSe_2 as an isotropic material. The thickness of WSe_2 is varied and takes the values a) $d_2 = 5$ nm, b) $d_2 = 10$ nm and c) $d_2 = 15$ nm. The horizontal dotted lines represent the A-exciton resonance energy.

The results of the calculation of the dispersion relation, for different thicknesses d_2=5, 10 and 15 nm, is presented in Figure 4.8. For a thickness of 5 nm, the dispersion relation differs little from the one of the air/gold interface. The main difference comes from the higher confinement of the SPPs due to the high refractive index of WSe_2. For a thickness of 10 nm, the coupling of the SPPs to the excitons - having in this case a resonance at 1.62 eV - starts to be visible through a characteristic back-bending. As the thickness of WSe_2 increases, the total field is also more confined which is reflected in the higher q values. This trend continues in the case of a thickness of 15 nm. The stronger confinement and back-bending with increasing WSe$_2$ thickness d_2 are in agreement with the intuition that the effective dielectric function felt by the SPPs becomes larger as d_2 increases.

It should be noted that in the case of $d_2 = 15$ nm, the dispersion relation is even crossing the light line in air. For the corresponding energies, the resulting wave is thus not bound to the interface and becomes leaky [18].

However, until now, WSe$_2$ has been considered as an isotropic material, with the same refractive index containing the characteristic resonances from the excitons in all directions. As discussed in Section 4.2, WSe$_2$ has different in-plane and out-of-plane refractive indices. This material is thus anisotropic and not taking this property into account in the calculation of the dispersion relation could lead to errors such as overestimation of the coupling.

4.5 Theoretical dispersion relation with anisotropy

As has been highlighted in recent articles [43,44,104–106], WSe$_2$ and similar multilayered materials have a different refractive index in the z-direction compared to the x- and y-directions. The anisotropy of these materials has thus to be taken into account. In this section, the basic properties of uniaxial anisotropic materials are presented, and a TMM adapted to these materials is derived.

4.5.1 Uniaxial anisotropic materials

For anisotropic materials with principal dielectric axes along the (x, y, z)-directions, the dielectric function can be described as [113, 115]

$$\overleftrightarrow{\varepsilon} = \begin{pmatrix} \varepsilon_x & 0 & 0 \\ 0 & \varepsilon_y & 0 \\ 0 & 0 & \varepsilon_z \end{pmatrix}. \tag{4.23}$$

In the case of uniaxial crystals such as WSe$_2$ [43], two of the dielectric functions are equal. The two equal dielectric functions are named *ordinary* dielectric function ε_{ord} and the remaining one is the *extraordinary* dielectric function ε_e [113]. The dielectric function of the uniaxial crystal can thus be expressed as

$$\overleftrightarrow{\varepsilon} = \begin{pmatrix} \varepsilon_{ord} & 0 & 0 \\ 0 & \varepsilon_{ord} & 0 \\ 0 & 0 & \varepsilon_e \end{pmatrix}. \tag{4.24}$$

For plane waves in a homogeneous anisotropic medium, the electric field should satisfy the wave equation [113]

$$\mathbf{k} \times (\mathbf{k} \times \mathbf{E}) + \frac{\omega^2}{c^2} \overleftrightarrow{\varepsilon} \mathbf{E} = 0. \tag{4.25}$$

Solving this wave equation in the case of a uniaxial crystal leads to a relation between ω and the components of the wavevector $\mathbf{k}$ satisfying [113, 115]

$$\left(\frac{k_x^2 + k_y^2}{\varepsilon_e} + \frac{k_z^2}{\varepsilon_{ord}} - \frac{\omega^2}{c^2}\right)\left(\frac{k^2}{\varepsilon_{ord}} - \frac{\omega^2}{c^2}\right) = 0. \tag{4.26}$$

Equation 4.26 has two solution, corresponding respectively to the leftmost and the rightmost factor being zero. The leftmost factor being zero is equivalent to the equation of an ellipsoid of revolution, while the rightmost factor corresponds to the equation of a sphere [115]. Both these surfaces determine the $\mathbf{k}$-components depending on the refractive indices $n_{ord} = \sqrt{\varepsilon_{ord}}$ and $n_e = \sqrt{\varepsilon_e}$ and the wavelength of the incident light. They are usually called $\mathbf{k}$-surfaces [115]. Due to the circular symmetry around the z-axis, both $\mathbf{k}$-surfaces can be represented in the (x,z)-plane without loss of generality, as sketched in Figure 4.9a.

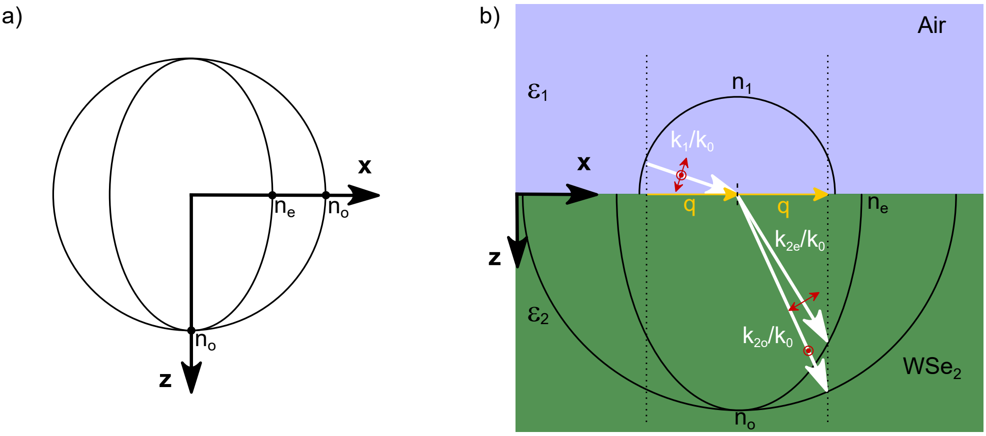

Figure 4.9. Anisotropy and the $\mathbf{k}$-surfaces in the case of the uniaxial crystal WSe$_2$. a) Sketch of the $\mathbf{k}$-surfaces for WSe$_2$ projected on the (x,z)-plane. In this sketch, $n_{ord} = \sqrt{\varepsilon_{ord}}$ and $n_e = \sqrt{\varepsilon_e}$ are respectively the ordinary and extraordinary refractive indices of WSe$_2$. b) Refraction at the air/WSe$_2$ interface for s- and p-polarized light. In each medium, half of the corresponding $\mathbf{k}$-surface is drawn. The in-plane wavevector q remains the same in both media. The intersections of the normal to the surface determined by q (black dotted lines) and the $\mathbf{k}$-surfaces correspond to the wavevector. The s-polarized light becomes the ordinary ray, while the p-polarized light becomes the extraordinary ray.

When a combination of s- and p-polarized light travels from an isotropic medium (characterized by a constant ε_1) to a uniaxial anisotropic medium (characterized by a constant ε_2), the $\mathbf{k}$-surfaces can be used to predict the direction and magnitude of the $\mathbf{k}$-vector of the s- and p-polarized light, depending on the incident direction. The method to do so in the case of a uniaxial crystal such as WSe$_2$ is sketched in Figure 4.9b. As we are in the (x,z)-plane, we can consider that $k_y = 0$ and define an in-plane component of the wavevector $k_x = q$. This in-plane wavevector q remains constant in both media. The direction and magnitude of the wavevector(s) in the second medium is thus determined by the intersection between the normal to the air/WSe$_2$ interface - positioned by q - (black dotted lines in Figure 4.9b) and the **k**-surfaces. As the p-polarization has a component along the z-direction, it is governed by the ellipsoid. On the other hand, the s-polarization is governed by the sphere [115]. The light is thus split in a p-polarized extraordinary ray and a s-polarized ordinary ray.

Thus, it follows that for the p-polarization, the out-of-plane component of the wavevector can be described as:

$$k_z = \sqrt{\varepsilon_{ord}\left(\frac{\omega^2}{c^2} - \frac{q^2}{\varepsilon_e}\right)} \tag{4.27}$$

More information about the optics of anisotropic materials can be found in references [113] and [115].

4.5.2 Anisotropic transfer matrix method

As TMDCs are uniaxial anisotropic crystals, the TMM should be adapted to the case of uniaxial crystals. To do so, instead of isotropic materials, we consider uniaxial crystals with a dielectric function $\overleftrightarrow{\varepsilon}$ given by Equation 4.24. In the following, as for Section 4.4.1, only the case of p-polarization is considered.

At the interface between two uniaxial crystals, Equations 4.4a and 4.4b, as well as the continuity equations 4.5 and 4.6 are still valid. The modifications to the usual TMM derivation starts at Equation 4.7. With the values for the dielectric function being different depending on the direction, Equation 4.7 becomes

$$-\frac{\partial H_{iy}}{\partial z}\hat{\mathbf{x}} + \frac{\partial H_{iy}}{\partial x}\hat{\mathbf{z}} = \varepsilon_0\varepsilon_{iord}\frac{\partial E_{ix}}{\partial t}\hat{\mathbf{x}} + \varepsilon_0\varepsilon_{ie}\frac{\partial E_{iz}}{\partial t}\hat{\mathbf{z}}. \tag{4.28}$$

in a medium characterized by $\overleftrightarrow{\varepsilon_i}$ and where $\hat{\mathbf{x}}(\hat{\mathbf{z}})$ are the unit vectors of the $x(z)$ directions. The projection of Equation 4.28 along the x-direction gives

$$-ik_{iz}(A_1 - B_1)e^{iqx}e^{-i\omega t} = -i\omega\varepsilon_0\varepsilon_{iord}E_{ix} \tag{4.29}$$

and the continuity of E_x at $z = 0$ therefore leads to

$$\frac{k_{1z}}{\varepsilon_{1ord}}(A_1 - B_1) = \frac{k_{2z}}{\varepsilon_{2ord}}(A_2 - B_2). \tag{4.30}$$

Equation 4.9 is thus replaced with Equation 4.30. In addition, the continuity of H_{iy} at the interface being still valid means that Equation 4.8 is verified in the anisotropic case. This means that for p-polarized light and in the case of a uniaxial material with principal axes along the (x, y, z)-directions, the transmission matrix D_{12} becomes

$$D_{12} = \frac{1}{2}\begin{pmatrix} 1 + \frac{\varepsilon_{1ord}k_{2z}}{\varepsilon_{2ord}k_{1z}} & 1 - \frac{\varepsilon_{1ord}k_{2z}}{\varepsilon_{2ord}k_{1z}} \\ 1 - \frac{\varepsilon_{1ord}k_{2z}}{\varepsilon_{2ord}k_{1z}} & 1 + \frac{\varepsilon_{1ord}k_{2z}}{\varepsilon_{2ord}k_{1z}} \end{pmatrix}. \tag{4.31}$$

Additionally, the form of the propagation matrix P_i remains the same in the anisotropic case. However, as mentioned in Section 4.5.1, the form of k_{iz} in an anisotropic medium i and for p-polarization is different. P_i thus becomes

$$P_i = \begin{pmatrix} e^{-ik_{iz}d_i} & 0 \\ 0 & e^{ik_{iz}d_i} \end{pmatrix}, \text{ with } k_{iz} = \sqrt{\varepsilon_{iord}\left(\frac{\omega^2}{c^2} - \frac{q^2}{\varepsilon_{ie}}\right)}. \tag{4.32}$$

with d_i the thickness of the layer i. The two new matrices in Equations 4.31 and 4.32 can be multiplied the same way as the usual TMM, leading to the same type of relationships as Equations 4.15 and 4.18 to find the reflection and transmission coefficients. The derivation of the impedance coefficients for the anisotropic case is given in Appendix D.

The transmission and propagation matrices were derived in this PhD work independently from the work of Majerus et al. [116] and Hammid et al. [117], and we arrived at the same matrices as Ref. [116] in the case of p-polarization.

As a remark, one could notice that the derivation of the TMM in the anisotropic case remains fairly simple mainly because the principal axes of the anisotropic material(s) are aligned with the x-,y- and z-directions. If this were not the case, a generalized 4x4 matrix method taking into account the mixing of the s- and p-polarizations should be used [113, 118].

4.5.3 Theoretical dispersion relation with anisotropic WSe$_2$

The studied structure and the main principle and explanations of the Matlab program used to calculate the dispersion relation is the same as the one presented in Section 4.4.2. The main differences to adapt to the anisotropic case lie in the expression of the transmission matrix $D_{i(i+1)}$, which is defined as Equation 4.31, and the expression of the propagation matrix defined as

$$P_i' = \begin{pmatrix} e^{k_{iz}'d_i} & 0 \\ 0 & e^{-k_{iz}'d_i} \end{pmatrix}, \text{ with } k_{iz}' = \sqrt{\varepsilon_{iord}\left(\frac{q^2}{\varepsilon_{ie}} - \frac{\omega^2}{c^2}\right)}. \tag{4.33}$$

Figure 4.10 displays the calculated dispersion relation for the thicknesses $d_2 = 5$, 10 and 15 nm. The isotropic solution is also shown in black dotted lines for comparison. The anisotropic solution shows a dispersion relation closer to the light line, meaning that the confinement of the polaritons is smaller. Furthermore, the splitting of the modes - related to the coupling strength - is also slightly reduced. These two effects arise from the difference between the out-of-plane dielectric function ε_e and the in-plane dielectric function ε_{ord} of the WSe$_2$. As ε_e is more than two times smaller than ε_{ord} (recall Figure 4.4) and the isotropic solution was only taking ε_{ord} into account, the isotropic solution was overestimating the “mean” dielectric function.

The difference is however smaller than what could be expected from a p-polarized wave such as SPPs, especially for smaller thicknesses. The only modification compared to the isotropic case is indeed coming from the propagation matrix, and not from the transmission matrix. As a consequence, as was argued in previous works [103, 104], the effect of the anisotropy becomes significant only above a thickness of a few tens of nanometers (about 15 nm in the case of WSe_2). Furthermore, the thicker the layer, the more important the effect of the anisotropy is. A similar conclusion on the effect of the thickness on the differences between the anisotropic and isotropic model was reached in Ref. [116].

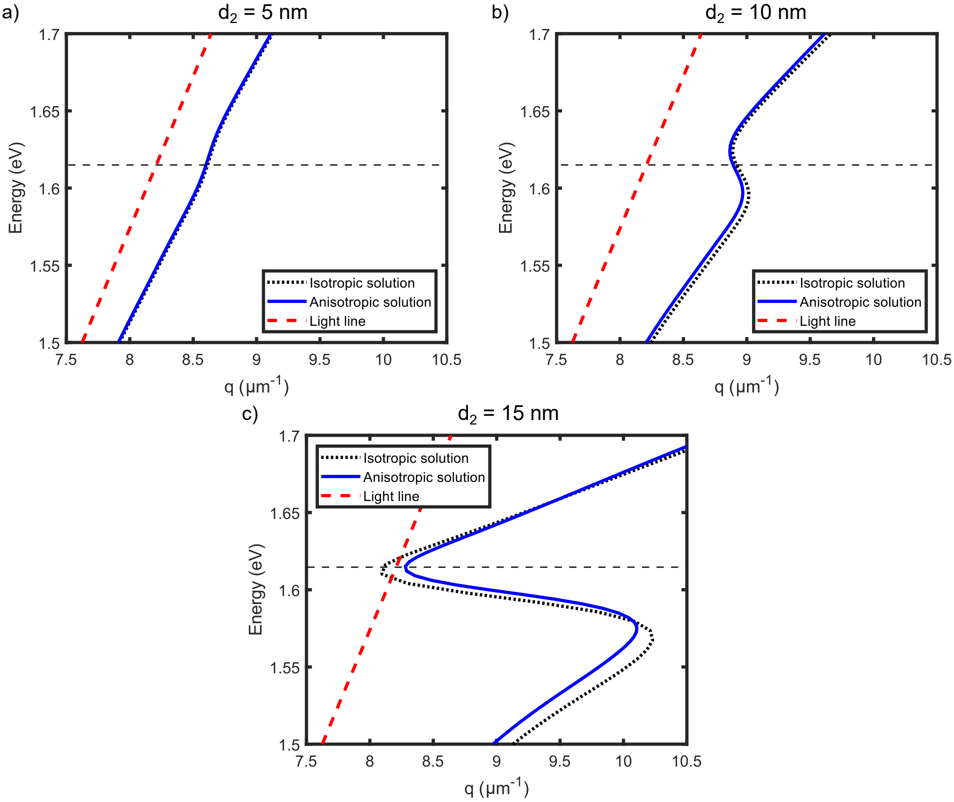

Figure 4.10. Calculated dispersion relation for the 4-layer structure, when taking into account that WSe_2 is an anisotropic material. The thickness of WSe_2 is varied and takes the values a) $d_2 = 5$ nm, b) $d_2 = 10$ nm and c) $d_2 = 15$ nm. The horizontal dashed lines represent the A-exciton resonance energy.

The anisotropy has thus been taken into account in the derivation of the TMM and this new model has been compared with the commonly used TMM, taking into account isotropic materials. To our knowledge, it the first time that the dispersion relation has been calculated for a TMDC on gold using the 2×2 anisotropic TMM. A comparison with experiments is therefore needed to verify if this model turns out to be more accurate than the isotropic TMM.

CHAPTER 5

s-SNOM measurements of the coupled system

Chapter 4 presented the theory and models behind the coupling between excitons in TMDCs and SPPs on gold. The thickness from which a splitting could be resolved is about 10-15 nm. In this chapter, preliminary experiments aiming to measure the coupling between excitons in multilayer WSe_2 with near-field methods are presented.

The fabrication of the sample with WSe_2 on gold is first be described. The dispersion relation is first reconstructed for a gold surface without TMDC, by using a tunable laser and measure the SPPs wavelength for each consecutive excitation energy. This step enables a comparison with the experiments from Chapter 3. Thereafter, near-field measurements of the sample with WSe_2 are described and analyzed.

5.1 Sample fabrication

The fabrication of the stratified structure involves the fabrication of a sample of about 10-15 nm thickness. The fabrication process involves the exfoliation of the bulk TMDC and the transfer of the desired flake onto a gold platelet. Both the exfoliation and transfer were carried out by Qiaoling Lin, PhD student.

5.1.1 Exfoliation of TMDs

Since the discovery of graphene in 2004 [89], the preferred method to obtain the highest quality of 2D materials has been the mechanical exfoliation of the origin 3D crystal.

Here, the substrate for the exfoliation was Polydimethylsiloxane (PDMS, here PF-40/17-X4 from Gel-pak®) deposited on a glass slide. The tape used for the exfoliation was the light blue tape from SPS Ltd. (1007R), as it has the advantage of leaving few residues on the substrate compared to the regular office scotch tape. The bulk crystal was WSe_2 from HQ graphene. A representative example of the bulk crystal is presented in Figure 5.1a.

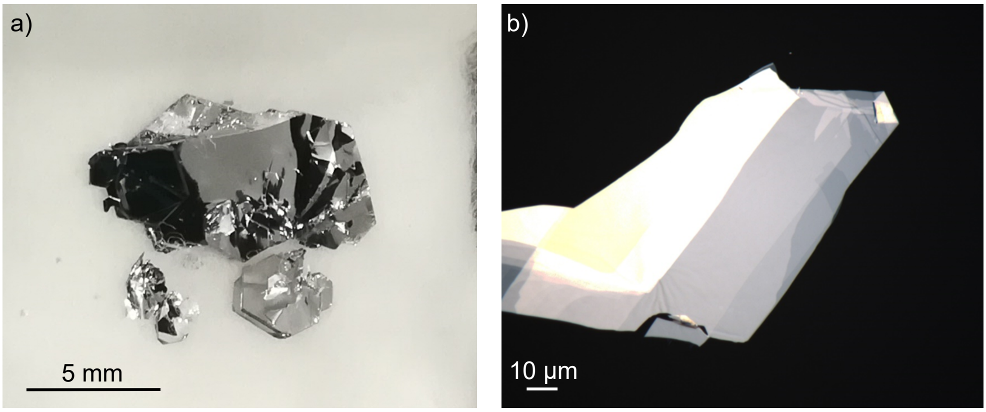

Figure 5.1. WSe_2 crystal. a) Picture of a bulk crystal of WSe_2. b) Picture of an exfoliated sample, made with an optical microscope with 100X magnification. The same sample is then transferred and measured in the following sections.

The exfoliation was carried in a similar way to the guide from Ossila LTD [119]. The bulk crystal was first deposited on a small piece of blue tape, such that only a thin layer of WSe_2 is left. The blue tape was then covered with a second piece of tape. After applying some pressure, the two tapes were pealed off. This process was repeated to cover a larger surface of the PDMS. The tape was then pressed on the PDMS substrate and pealed off. An example of the resulting flakes is shown in Figure 5.1b.

5.1.2 Dry transfer on gold

The flake shown in Figure 5.1b was transferred using the dry transfer method [120]. This method uses the viscoelastic properties of the PDMS stamp to transfer the WSe_2 onto the gold surface. As the Al_2O_3 layer deposited on the monocrystalline gold platelet have a low roughness, the WSe_2 flakes adhere well to the gold surface, which leads to a high yield of the transfer.

Figure 5.2a shows a bright field microscope picture of three WSe_2 flakes transferred on a 100-nm thick monocrystalline gold platelet covered with 2 nm of aluminum oxide, like the one studied in Chapter 3. The flake shown in Figure 5.1b has been transferred on the bottom right side of the gold platelet. The crystal slightly broke during the transfer process, but a large area without cracks is still measurable close to the bottom right edge.

Figure 5.2b presents a dark field microscope picture of the same sample. The dark field microscope reveals the scattered light, by blocking the direct reflection from the surfaces. While the WSe_2 surface seems mostly flat in the bright field picture, the dark field image highlights a number of bubbles, coming from air trapped between the TMDC and gold surfaces during the transfer. These bubbles can potentially disturb the near-field measurements by generating SPPs if they are small, or suppressing the contact between the TMDCs and the gold if they are large. They should thus be avoided as much as possible in the near-field measurements.

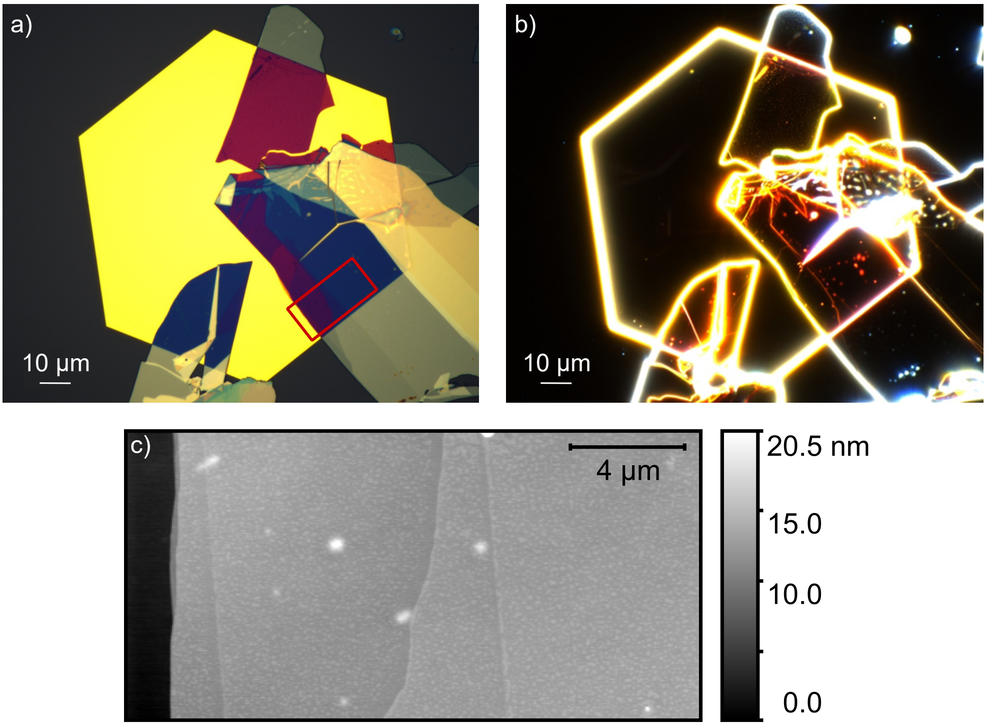

Figure 5.2. Sample after transfer. a) Picture of the sample after transfer, made with an optical microscope with 100X magnification used in bright field, and b) dark field. c) Topography of the area highlighted by the red box in a).

The thicknesses of the resulting flakes were determined using the topography given by the s-SNOM. The topography of the region marked by the red box in Figure 5.2b is presented in 5.2c. Apart from the gold substrate on the left, four different areas with four different thicknesses can be distinguished. The height of the different thicknesses was estimated using the *Terraces* function of Gwyddion[1]. From left to right, it was

---

[1] Parameters: step detection kernel of 3%, step detection threshold of 2.8%, broadening of 1 pixel, minimum terrace area of 0.5% and background fitted with a polynomial of degree 8.

found with this function that the different areas have thicknesses of 10.5 ± 0.4 nm, 10.6±0.4 nm, 11.7±0.4 nm, and 12, 3±0.4 nm. As one layer of WSe_2 has a thickness of 0.7 nm, the actual thicknesses are more likely 9.8 nm (14 layers), 10.5 nm (15 layers), 11.9 nm (17 layers) and 12.6 nm (18 layers). The fitted thicknesses are however be used in the following.

5.2 Experimental details for the near-field measurements

The procedures follows the same idea as in Chapter 3, with sometimes a few additional steps to retrieve the relevant signal. The setup used for the near-field measurements is corresponding to Figure 1.3 from Section 1.1.3. The laser used for the measurements is a femtosecond Tsunami laser, and the laser power is attenuated to 15 mW by placing a half-wave plate and a polarizer in front of the neaSNOM box (see Appendix B). Assoc. Prof. Binbin Zhou gave substantial help with the installation and alignment of the laser. The laser was used in continuous mode (i.e. not mode-locked), as in Refs. [51, 52, 108], and tuned from a wavelength of about 730 nm to about 810 nm. The wavelength of the laser was measured with a spectrometer (USB4000 from Ocean Insight Inc.).

For each wavelength of the laser, a near-field map was made, in the configuration as in Chapter 3. Due to laser instabilities, the PsHet detection could not be used. Thus, the nature of the resulting signal is different: as the PsHet could not be used, the measured signal corresponds to the intensity expressed in Equation 1.13. As the linewidth of the laser is larger than a HeNe laser, an uncertainty of ±1 nm - corresponding to the full-width half-maximum of the laser spectrum - is taken (see spectrum in Appendix B).

In the following sections, the resulting maps, linescans and their analysis to make the dispersion relation are presented.

5.3 Near-field measurements: dispersion relation on gold

To measure the dispersion relation of the sample of interest, the wavevector associated with each energy of the incident light (in the interesting energy range) needs to be probed. In the two following sections, the characterization of the wavevector is made by scanning the surface of the sample and retrieving the interesting wavevector from the resulting maps.

To benchmark the effect of the change of laser and compare the theoretical dispersion relation with the experimental dispersion relation from a familiar sample, the dispersion relation was first measured on gold, without transfer of WSe_2.

5.3.1 The different field contributions

The characterization of the complex wavevector was made on gold once again on the same gold platelet as in Chapter 3. The laser makes in this case an angle of 3° with the platelet edge. A map was made for five wavelengths from 731 nm to 811 nm. Figure 5.3 presents two near-field intensity maps representative of the five near-field intensity maps made to measure the dispersion relation on gold. The wavelength used is $\lambda_{\mathrm{laser}} = 731$ nm in Figure 5.3a and $\lambda_{\mathrm{laser}} = 811$ nm in Figure 5.3b. The raw data is shown on the left-hand side. Some plasmonic oscillations can be distinguished, but high variations of the mean value of the near-field intensity from one line to the other can also be seen. These variations can be attributed to instabilities of the Tsunami laser used as a CW laser. Moreover, the far-field background is not completely suppressed, as the PsHet is not used in this case, and could thus lead to some changes in the signal.

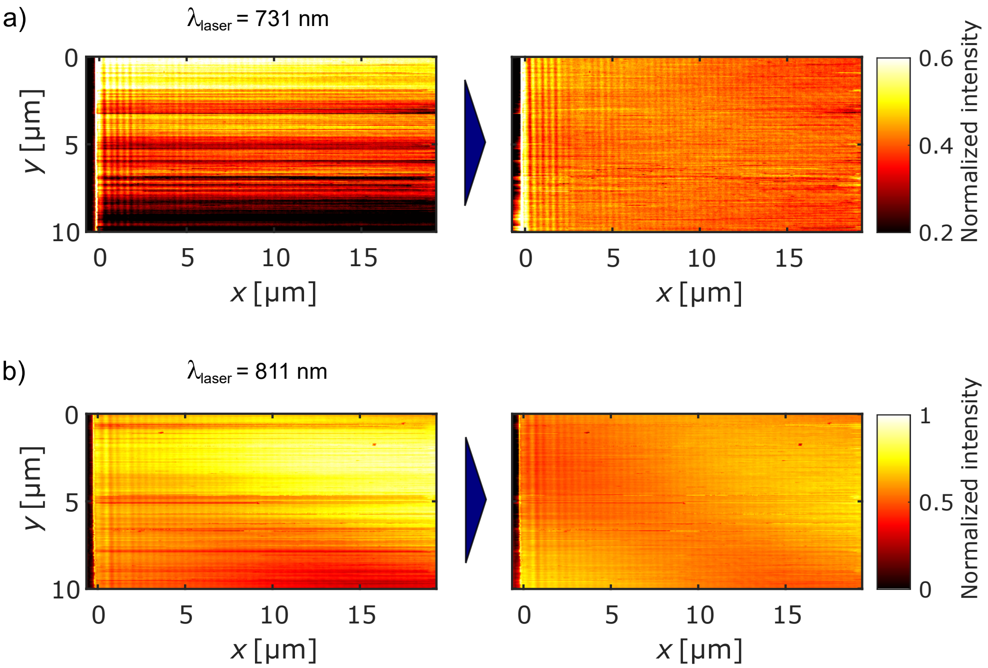

Figure 5.3. Normalized near-field intensity maps on gold for a wavelength of a) 731 nm and b) 811 nm. The raw data is on the left-hand side, and the post-processed data on the right-hand side.

To remove these unwanted variations, all the rows of the near-field map are set to the mean value of the map. The result of this treatment is shown on the right-hand side. The vertical variations are not totally suppressed, but less present and the plasmonic oscillations are much easier to distinguish. Thus, these instabilities do not seem to perturb the SPP wavefront.

The profiles extracted from these maps were made in the same manner as in Chapter 3, i.e. by calculating the mean value of all the lines from each map. The resulting profiles for $\lambda_{\text{laser}} = 731$ nm and $\lambda_{\text{laser}} = 811$ nm are presented in Figures 5.4a and 5.4b, respectively. Compared to the profiles in Chapter 3, the profiles do no have a constant mean value. We interpret this effect as the influence of the far-field background. The corresponding spectra for the total profile and from the selected red region is presented below each profile. The spectra are normalized to the tip-launched peak.

The tip-launched SPPs are still predominant at grazing angle, and the tip-reflected edge-launched SPPs are barely seen. However, another peak close to the tip-launched SPP wavelength can also be observed in the spectrum, in particular in the case of $\lambda_{\text{laser}} = 731$. This peak could correspond to second order effects such as interference between tip-launched and edge SPPs, and disappears when the region further from the edge is selected (see red spectra).

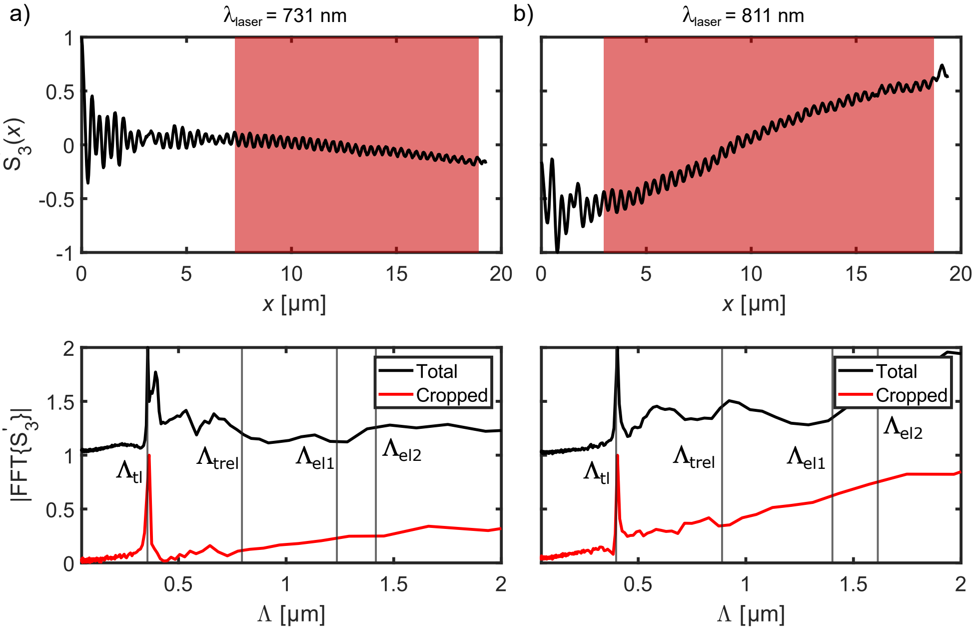

Figure 5.4. Normalized near-field intensity profiles and respective spectra on gold for a wavelength of a) 731 nm and b) 811 nm. The Fourier transform is plotted as a function of the fringe spacing $\Lambda = 2\pi/K$.

The dispersion relation could thus be retrieved simply by measuring the maximum value of the tip-launched peak. A more consistent method though would be to fit the profiles or the tip-launched peaks itself, as in Chapter 3. However, as the oscillations from the tip-launched SPPs are superimposed with low frequency variations, the fitting of the profiles with expressions of the same form as derived in Chapter 3 is difficult.

5.3.2 Fourier filtering

As seen in Figure 5.4, the plasmonic oscillations are superimposed with some low frequency variations that make the fitting in real space difficult. These low frequency variations can be filtered out by Fourier filtering. The idea of Fourier filtering is to suppress some frequency components in the spectrum, such that the corresponding variations are suppressed in the real space [121].

In practice, the spectrum is multiplied with a normalized filtering function, called a window function. The window function should not be abrupt, to avoid creating high frequency components that were not previously part of the signal.

Figure 5.5a shows the full view of the spectrum presented in Figure 5.4 - here as a function of the wavevector q - and the window function. In this case, we use a Tukey (or tapered cosine) window [122] with cosine fraction of $r = 0.1$, meaning a rectangular window with the first and last $r/2$ percent of the wavevector range equal to the ascending and descending parts of a cosine, respectively. This window function has the advantage of being flat up to the region around 10 $\mu\mathrm{m}^{-1}$, where the tip-launched peak is, so that this peak remains unchanged.

Figure 5.5b shows the product of the two functions presented in Figure 5.5a. The frequencies lower than 9.1 $\mu\mathrm{m}^{-1}$ are attenuated, with the lowest frequencies being totally removed. As can be seen when comparing the original profile in Figure 5.5c and filtered profile in 5.5d, this process is suppressing the low frequency background. Thereby, it facilitates the fitting of the profile and thus the retrieval of the wavelength and propagation length of the SPPs. However, one should keep in mind that, as seen in Section 3.4.2, the Fourier transform of a circular wave has non-zero frequency componant at $K = 0$, even when cropped. The suppression of the low frequency components could thus influence the estimation of the propagation length.

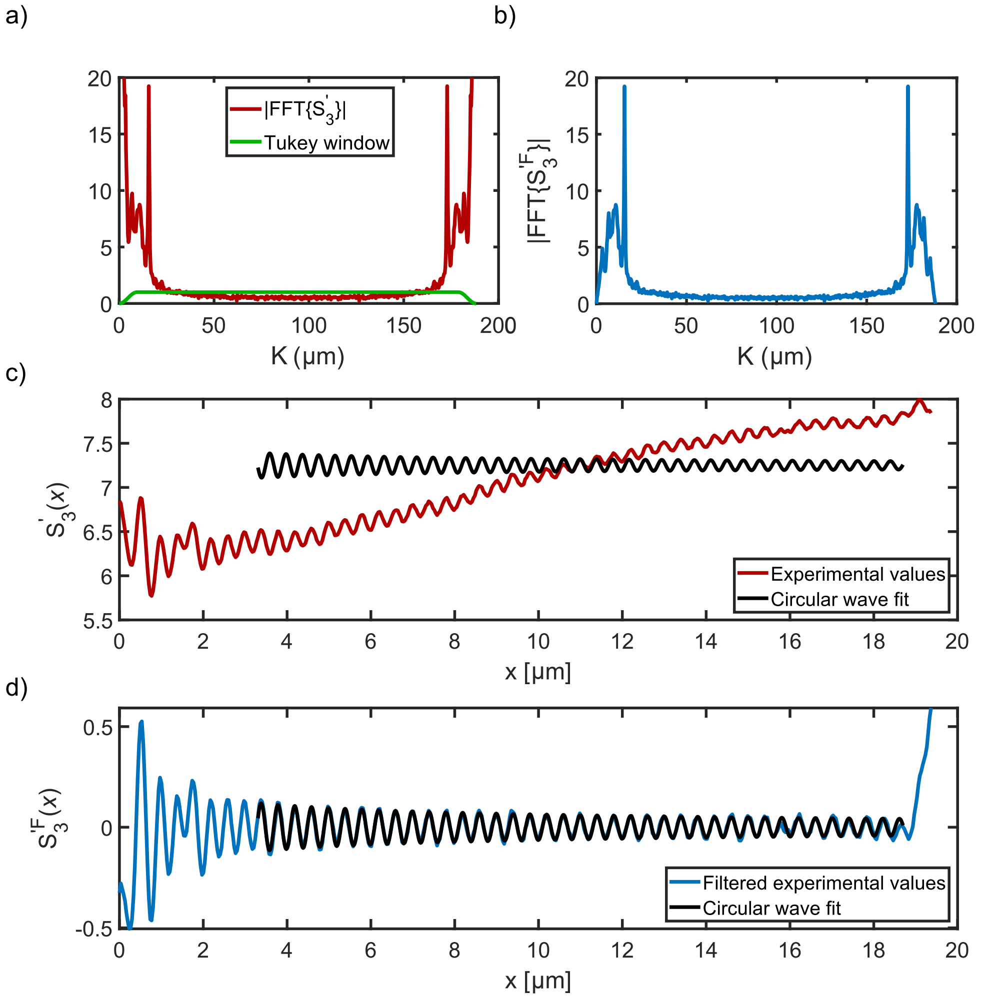

Figure 5.5. Fourier filtering. a) FFT of the profile showed in Figure 5.4b and Tuckey window. b) Product of the FFT and Tuckey window. c) Unfiltered profile and corresponding fit. d) Filtered profile and corresponding fit.

5.3.3 Dispersion relation and comparison with the theory

The tip-launched wavevector K_{tl}, the corresponding SPP wavelength λ_{SPP} and the tip-launched propagation length $L_{\mathrm{p}}^{\mathrm{tl}}$ resulting from the circular wave fit are presented in Table 5.1 for each laser wavelength λ_{laser}. In some cases, the propagation length was not converging to a value, and in such case the value of $L_{\mathrm{p}}^{\mathrm{tl}}$ is not given. The uncertainty on the laser wavelength λ_{laser} corresponds to the full-width half maximum of the laser spectrum see by the spectrometer.

The wavevector values are close to the theoretical ones and follow the same behaviour, but out of the 95% confidence range from the fit. However, as mentioned in Section 3.4.3, additional sources of uncertainty can come from the AFM positioning.

Concerning the propagation length, the difficulties to accurately determine L_p^tl and the discrepancies between the experimental and theoretical values are attributed to the Fourier filtering.

λ_laser (nm)	K_tl (µm^{-1})	λ_SPP (nm)	$K_\mathrm{tl}^\mathrm{th}$ (µm^{-1})	L_p^tl (µm)	$L_\mathrm{p}^\mathrm{tl,th}$ (µm)
731 ± 1	17.430 ± 0.006	720.8 ± 0.3	17.7	31 ± 6	50.4
749 ± 1	17.032 ± 0.005	737.8 ± 0.2	17.2		57.4
772 ± 1	16.486 ± 0.002	762.24 ± 0.04	16.7		65.3
790 ± 1	16.086 ± 0.006	781.2 ± 0.1	16.3		73.3
811 ± 1	15.677 ± 0.006	801.6 ± 0.2	15.8	84 ± 40	81.1

Table 5.1. Wavevector K_tl, propagation length L_p^tl and SPP wavelength λ_SPP for the different laser wavelengths λ_laser, resulting from the real space fit. The uncertainties here correspond to the 95% confidence bound given by the fit.

Figure 5.6 presents the comparison between the theoretical dispersion relation and the experimental one recreated from the 5 measurement points. The theoretical curve is calculated using the TMM presented in Section 4.4.1 and the code presented in Section 4.4.2, with 0 nm of WSe_2. The refractive index values are taken from McPeak et al. [77] for the gold and Tulio Aguilar-Gama et al. [83] for Al_2O_3. The experimental points are corresponding to the SPP wavevector defined as $K_\mathrm{SPP} = K_\mathrm{tl}/2$. The errorbars in the vertical direction correspond to the experimental uncertainties on the excitation energy, which correspond to an uncertainty on the laser of ±1 nm.

The measurements points are close to the the theory. They are however all to the left of the theoretical curve. There could be different reasons for these discrepancies. First, there could be a systematic error on the wavelength in the spectrometer, due to some error in the spectrometer calibration. To check this potential bias, the wavelength of the stabilized HeNe laser has been measured with the same spectrometer. No noticeable deviation from 633 nm has been seen. A second possibility would be an systematic error on the calibration of the AFM. However, the calibration of the AFM has been checked with a test grating (TGQ1 from Spectrum Instruments), and no bias from the AFM has been found. These systematic errors have therefore been ruled out.

As the systematic experimental errors have been excluded, the remaining reasons are either an underestimation of the experimental errors or differences between the theoretical model and the experiment. Concerning the second point, the TMM does not take into account the influence of the tip, and is a model that considered plane waves. As the tip is here only used for launching and detecting the SPPs, it shouldn't influence the wavelength of the SPPs. Furthermore, the refractive index or thickness of the aluminum oxide could be over- or under-estimated, respectively.

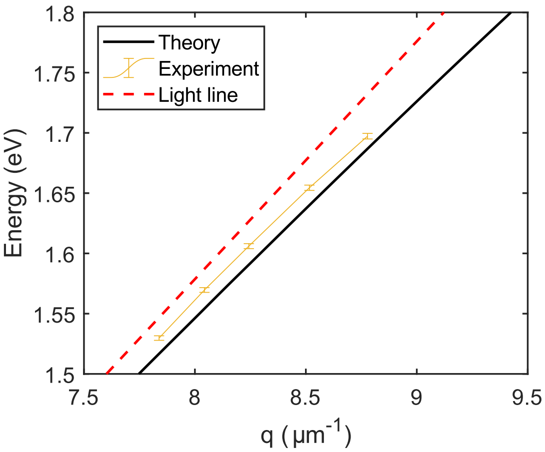

Figure 5.6. Dispersion relation of the SPPs on gold, covered with 2 nm of Al_2O_3. The theoretical curve has been calculated using the TMM, with the refractive index values from McPeak et al. [77] for the gold and Tulio Aguilar-Gama et al. [83] for Al_2O_3. The experimental points are half of the value of K_{tl} from Table 5.1.

In summary, the dispersion relation on gold determined experimentally follow the same tendency as the theory, but the experimental SPPs seem a bit less confined. The experiments with WSe_2 on gold could thus also give a slightly smaller experimental wavevector compared to the theory.

5.4 Near-field measurements of WSe_2 on gold

The measurement and analysis of one sample of WSe_2 on gold and the retrieval of the dispersion relation is presented.

5.4.1 The different field contributions

Figure 5.7 shows the topography and near-field maps of three out of 7 maps made in a wavelength range from 735 nm to 800 nm. On the topography from Figure 5.7a, four areas - highlighted with the red dotted lines - with four different thicknesses of WSe_2 can be distinguished. The area of thickness 10.5 nm is too thin and adjacent to the bare gold surface. It is therefore not studied in the following. As seen in Section 5.1.2, the three other areas have a WSe_2 thickness of 10.6 nm, 11.7 nm and 12.3 nm. Some bubbles can also be seen in the topography. These bubbles modify the near-field signal locally, but do not launch additional polaritons, which means that, provided that the bubble areas are avoided, the rest of the map can be analyzed.

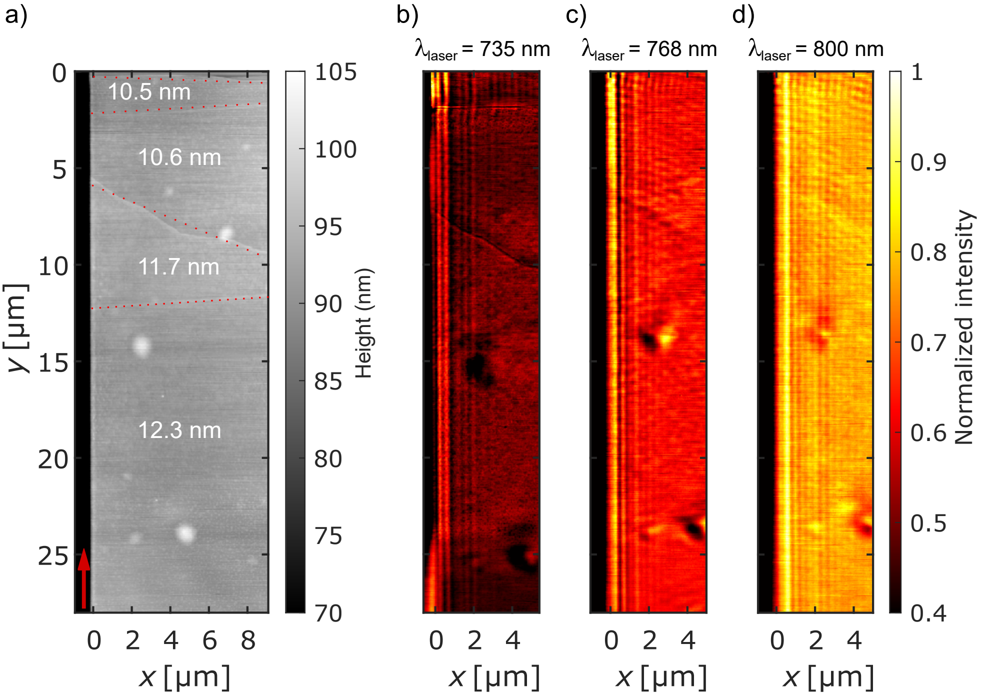

Figure 5.7. Near-field measurements of the WSe$_2$. a) Topography of the sample, and near-field intensity maps on a thin layer WSe$_2$ for a wavelength of b) 735 nm and c) 768 nm and d) 800 nm. The red arrow on the lower left corner of the topography represents the incident light.

Oscillations due to polaritons propagating at the interface(s) and parallel to the edge can be seen in the near-field intensity maps from Figures 5.7b, 5.7c and 5.7d. The longer the excitation wavelength, the longer their propagation length is. The propagation lengths are however much shorter than on bare gold, as expected from the higher confinement due to the high refractive index of WSe$_2$. It should also be noted that the oscillations parallel to the edge are also interfering with oscillations coming from the upper right corner of the map. This effect is particularly visible for a laser wavelength of 800 nm, where the propagation length is the longest. These additional polaritons are probably launched at the edge of the WSe$_2$ flake itself. Thus, the analysis could be influenced the interference with these additional oscillations, especially at longer excitation wavelengths.

Figure 5.8 shows the profiles as spectra obtained from the averaging of 100 lines of the maps at the position where the thickness of WSe$_2$ is equal to 11.7 nm. The vertical lines correspond to the wavelengths calculated for gold, without any WSe$_2$, according to Equations 3.6, 3.7 and 3.8. A number of peaks, probably coming from the tip-launched, edge-launched and tip-reflected edge-launched polaritons, can be seen in the spectrum of the full profile. Furthermore, the tip-launched wave if more confined than the corresponding tip-launched SPP without WSe_2, which confirms the higher confinement of the polaritons due to WSe_2.

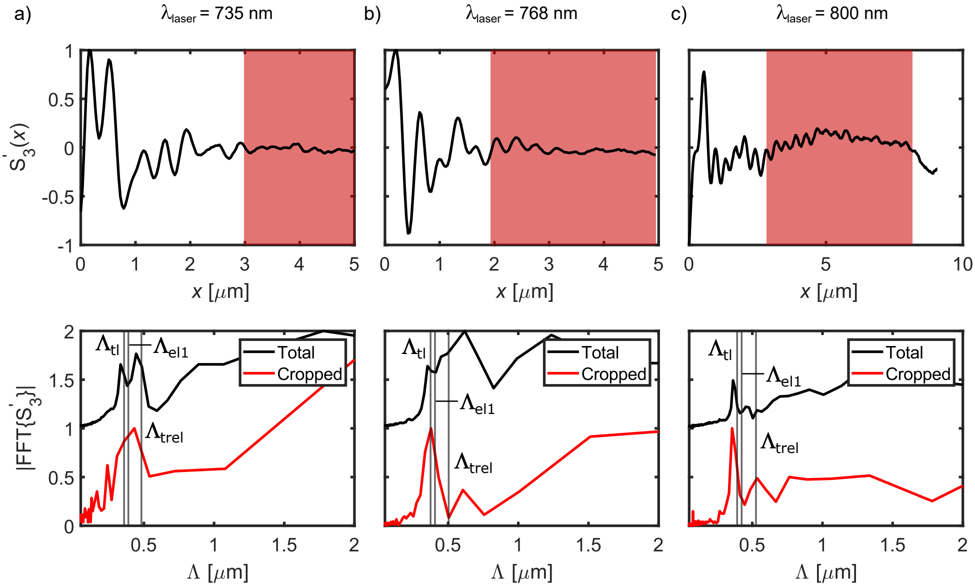

Figure 5.8. Normalized near-field intensity profiles and respective spectra from 11.7 nm of WSe_2 deposited on gold, for a wavelength of a) 735 nm and b) 768 nm and c) 800 nm.

Isolating the tip-launched polaritons is however difficult, especially at shorter wavelengths, due to a lack of clear oscillations away from the edge - probably due to shorter propagation length. As such, it is also difficult to fit the tip-launched signal, in real space and in Fourier space. The determination of the wavelength of these polaritons for the different laser excitations has thus here been implemented by taking the value of the tip-launched tip maximum, as has been done in previous works [51, 52, 108].

5.4.2 Dispersion relations and comparison with the theory

Figure 5.9a presents the comparison between the theoretical dispersion relation and the experimental one recreated from the 7 measurement points. The experimental wavevectors were determined by taking the maximum of the tip-launched peak in the spectrum of the total profiles (black spectra in Figure 5.8). For better precision on the determination of the maximum, the profiles were zero-padded with 7 times their total length before applying the Fourier transform. The theoretical curve is calculated using the anisotropic version of the TMM presented in Section 4.5.2 and the code presented in Section 4.5.3, with 11.7 nm of WSe$_2$. The refractive index values are taken from McPeak et al. [77] for the gold, Tulio Aguilar-Gama et al. [83] for Al$_2$O$_3$, and Munkbhat et al. [43] for WSe$_2$. The experimental points are corresponding to the measured SPP wavevector defined as $K_{\mathrm{SPP}} = K_{\mathrm{tl}}/2$. The errorbars are calculated in the same way as in Section 5.3.3.

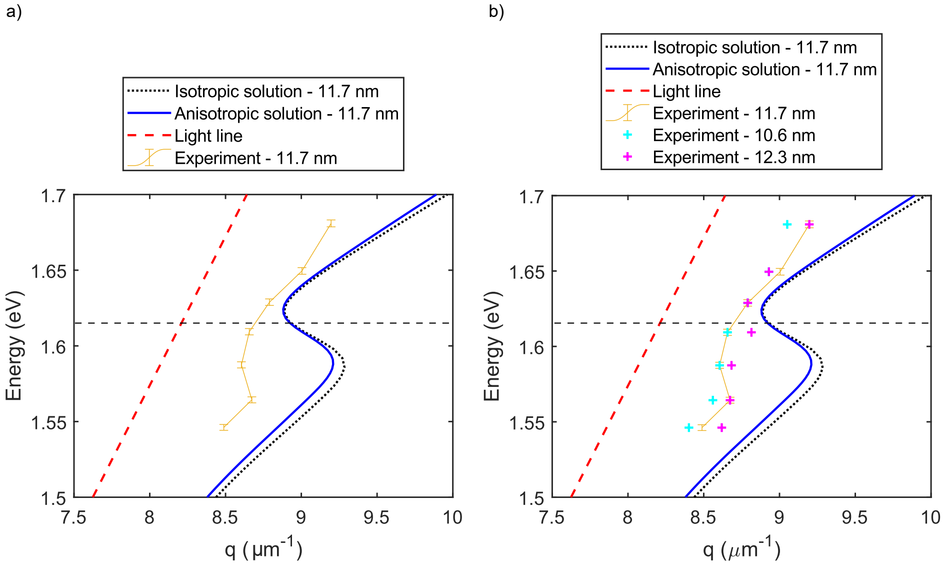

Figure 5.9. Dispersion relation of the polaritons on WSe$_2$ and gold a) for a WSe$_2$ thickness of 11.7 nm and b) for all the considered thicknesses. The theoretical curve has been calculated using the TMM, with the refractive index values from McPeak et al. [77] for the gold, Tulio Aguilar-Gama et al. [83] for the 2 nm Al$_2$O$_3$ layer, and Munkbhat et al. [43]. The experimental points are half of the value extracted from the spectra. The horizontal dashed lines represent the A-exciton resonance energy.

A back-bending can be observed from the dispersion relation at around 1.6 eV, which corresponds to the energy of the A-exciton in WSe$_2$. The back-bending is however smaller than the theory, and the experimental values are, as in Section 5.3.3, to the left of the theory curve, and generally not overlapping with the theory. Furthermore, the back-bending is not as clear for the other thicknesses, as can be seen in Figure 5.9b.

The difference between theory and experiment could have several reasons. First, as mentioned in the previous section, the oscillations from the polaritons are not as clear as the one from the bare gold surface. Indeed, at shorter wavelengths, the propagation length of the polaritons is shorter, thus it is difficult to disentangle them from the edge-launched polaritons. By contrast, at longer wavelengths, the absorption is lower and the propagation length is longer, but the tip-launched polaritons are interfering with oscillations coming from other edges. The measurement of the tip-launched wavelength could thus be influenced by this additional contribution. Furthermore, as mentioned in Section 5.3.3, the theory seems to slightly overestimate the confinement of the polaritons. A possible explanation could be the difference of treatment between the PW and the CW. Indeed, the derived TMM considers PWs, while the tip-launched SPPs are CWs. Thus, the additional geometrical losses could eventually influence the coupling. A more likely explanation could be that the dielectric function of our WSe_2 is different from the one of Munkhbat et al. [43], used for the theoretical predictions. The dielectric function measurements were performed on a silicon substrate in the case of Ref. [43], while our WSe_2 is on a gold substrate. A measurement of the reflection of our sample (WSe_2 on gold) has been made and compared to the same WSe_2 flake on the SiO_2/silicon substrate (substrate on which the gold lies). These two measurements are normalized by the intensity reflected by the bare monocrystalline gold platelet surface, as plotted in Figure 5.10. The substrate seems to influence the optical properties of the A-exciton, marked by the dip around 1.6-1.65 eV.

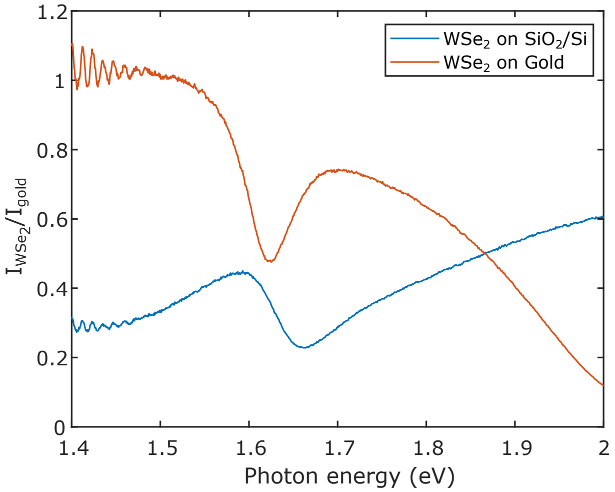

Figure 5.10. Reflection of the WSe_2 flake with 12.3 nm thickness on a SiO_2/silicon (SiO_2/Si) substrate compared to the monocrystalline gold substrate. The intensity reflected at the WSe_2 is normalized to the intensity reflected from the bare gold surface, considered as a perfect mirror in this spectral range.

In future works, some improvement to the analysis and the experiment could be implemented. On the analysis side, Fourier filtering of the maps (i.e. 2D Fourier filtering) could be done to remove the influence from the polaritons coming from other directions. The determination of the wavelength of the tip-launched polaritons could thereby be facilitated. Furthermore, the dielectric function from our sample (WSe_2 on gold) should be used in the TMM calculations. The in-plane dielectric function can be deduced from the reflection measurements, as has been done in Ref. [100].

On the experimental side, more s-SNOM measurements should be done to obtain clearer oscillations from the polaritons. The measurement of a larger WSe_2 area of constant thickness would avoid the interference with polaritons coming from other edges. Additionally, the stability of the laser should be increased. A workaround could be to get mode-locking with a small bandwidth, but could not be achieved in the present case at all wavelengths. Moreover, as the near-field signal is increased when the tip apex radius is increased, a larger tip apex radius could be used. We could also try to characterize the edge-launched polaritons instead of the tip-launched polaritons [16,51,52,79]. This would however require to defocus the laser, as has been done in a previous study [8], as the gaussian laser beam always moves with the tip. We could also deposit the WSe_2 flake in the middle of the gold and use its edge to launch the polaritons, as in Ref. [108].

In summary, these preliminary experiments show some influence from the excitons in WSe_2, with a slight back-bending at the A-exciton resonance frequency for a thickness of 11.7 nm, which indicates that the strong coupling is approached. However, more work has to be done to understand the behaviour of the resulting polaritons in a quantitative way. In particular, more experiments have to be made with larger areas in the same thickness range to confirm the observed tendencies.

Finally, a recent work was recently published [108] on the measurement of exciton-polaritons for WSe_2 on gold, just like our structure. The thicknesses used in this work are however much larger than in our work. This allows for a predicted splitting and a confinement of the polaritons which are much larger than ours. However, the upper polariton couldn't be measured in this study, while we have a chance to measure it with our structure. Furthermore, it seems that this study didn't take into account the anisotropy of WSe_2, which is likely to become important for higher thicknesses. It would thus be interesting to compare the theories with a sample of the same thickness as in Ref. [108]. Finally, to the best of our knowledge, the propagation length of these polaritons remains to be characterized.

Conclusion and outlook

In this thesis, we used a s-SNOM in a reflection configuration to quantitatively characterize the wavelength and the propagation length of SPPs on monocrystalline gold platelets, for an excitation wavelength of 633 nm. We then applied the gathered knowledge to study the interaction between these SPPs and excitons in WSe_2, by recreating the dispersion relation around the A-exciton resonance energy of WSe_2.

SPPs on monocrystalline gold platelets

We measured the near-field amplitude and phase of SPPs on a monocrystalline gold platelet, for six different azimuthal angles between the edge of the platelet and the incident light. Among these angles, we found that the grazing incidence angle is the best configuration to isolate the tip-launched SPPs from the edge SPPs. The isolation of the tip-launched SPPs could be achieved by selecting a region far from the edges of the platelet, as described in Ref. [36].

As a clear tip-launched signal could be retrieved, we derived a simple model to describe the amplitude and phase of the near-field profiles. This model considers the interference between the tip-launched SPPs and an offset coming from the near-field light that is directly back-scattered from the sample towards the s-SNOM tip. This model highlights a sinusoidal shape of both the near-field amplitude and the near-field phase, with a $\pi/2$ phase shift between these profiles. Both these descriptions are in agreement with the experimental profiles. Additionally, this model was found to be valid for a fairly large amplitude of the SPP oscillations compared to the amplitude of the offset.

As the tip-launched SPPs could be isolated and a model for the amplitude and phase of their near-field could be derived, the wavelength and propagation length of SPPs on monocrystalline gold platelets could be retrieved. We found a SPP wavelength of 608 nm and a SPP field propagation length of 24 µm, corresponding to a propagation length in intensity of 12 µm. These values were found to be consistent between the near-field amplitude and phase and not to be sensitively dependent on the choice of interval chosen for the fit. Furthermore, these values correspond well with the values calculated from the dielectric function of high-quality polycrystalline gold from McPeak et al. [77], as also highlighted in a recent work [10].

Moreover, with the Al_2O_3 protection layer, the high stability of the sample was shown by reproducing the same experiment after eight months.

These results could be used to characterize the dielectric function of other gold surfaces or other metals, as the wavelength and propagation length of SPPs is linked to the dielectric function. Furthermore, the change in the SPP propagation on metals having good plasmonic properties but degrading with time, such as silver, could be directly studied. The effect of the deposition of a protection layer could then be evaluated in a direct measurement. More generally, the method to retrieve the tip-launched signal and the model can be used for the study with PsHet detection of any kind of polaritons, across the optical spectrum. We also believe that the study of the angle between the incident light and the sample edge is relevant to other materials that face challenges such as the efficiency of the excitation of surface waves with the s-SNOM tip or interference with unwanted signals.

Coupling between excitons in WSe_2 and SPPs

We first calculated theoretically the dispersion relation for a sample made of thin-layered WSe_2 on top of the previously studied gold platelets. We derived a 2×2 TMM taking into account the anisotropy of WSe_2, and we obtained the same results as in a previous study of uniaxial van der Waals crystals [116]. We calculated the dispersion relation of the multilayer sample based on this anisotropic TMM. For comparison, we also calculated the dispersion relation in the case of the usual (isotropic) TMM, where only the in-plane dielectric function of WSe_2 is used. We found a slightly lower confinement and lower coupling between the excitons and the SPPs in the dispersion relation calculated using the anisotropic TMM. The difference in confinement and coupling becomes larger as the thickness of the WSe_2 layer is increased.

The 2×2 anisotropic TMM used in this thesis is applicable to any uniaxial crystal across the visible spectrum, both for far-field and near-field studies. As it is less computationally heavy than the 4×4 TMM, we believe it should be advertised for calculations on stratified structures with uniaxial crystals.

Using a tunable laser, we made preliminary measurements first on a bare monocrystalline gold platelet, and then on a sample with a WSe_2 flake - with thicknesses ranging from 10.5 nm to 12.3 nm - on a gold platelet. The Al_2O_3 layer was thereby used as a spacer between the gold and the WSe_2. We used the grazing angle configuration to extract the wavevector of the tip-launched polaritons for different excitation energies around the energy of the A-exciton of WSe_2. With this information, we reconstructed the dispersion relation of polaritons on this sample.

The experimental dispersion relation for SPPs on the bare gold platelet was found to be in fairly good agreement with the theoretical one. In the case of the sample with WSe_2, a small back-bending at the resonance energy of the A-excitons of WSe_2 was observed, showing that the strong-coupling interaction regime between the SPPs and the excitons was approached.

With these results, we are one step closer towards the full quantitative characterization of the wavelength and propagation length of plasmon-exciton polaritons in TMDCs. Further work should be done on the far-field characterization of the dielectric function of WSe_2 flakes on gold, to insure a proper value for the theoretical calculations. Furthermore, these preliminary measurements show the importance of having clean and large WSe_2 flakes to avoid interference with additional polaritons excited at other edges or at defects.

Applicability to other structures and near-field techniques

The methods developed in this thesis are applicable to the characterization of polaritons in other structures involving surface waves and TMDCs, for a s-SNOM in a reflection configuration. The characterization of these plane samples could serve as a baseline for more elaborate structures, such as waveguides and cavities, made out of the same materials. Such structures could then be characterized with s-SNOM, as we have done for example in the case of newly developed dielectric nano-cavities [123], to help their development and improve their design.

Furthermore, the same procedure to extract the wavelength and propagation length of tip-launched polaritons could be applied in the case of measurements made with a nano-FTS and a broadband source. Using the nano-FTS could enable the retrieval of the dispersion relation in one measurement, and to visualize the time-dependence of the polaritons.

Appendices

APPENDIX A

Pseudo-heterodyne detection - detailed calculations

A.1 Fourier components and multiplication

Let us calculate the Fourier decomposition of one of the conjugated terms in Eq. 1.10:

$$
\begin{aligned}
E_C &= E_{NF}E_B^* = \sum_n E_{c,n}\exp\{in\Omega t\} \\
E_C &= \left(\sum_n E_{\mathrm{nf},n}\exp(in\Omega t)\right)\left(\sum_n E^*_{b,n}\exp(-in\Omega t)\right) \\
E_C &= \sum_n\sum_k E_{\mathrm{nf},n}E^*_{b,k}\exp(i(n-k)\Omega t) \quad (n\to k) \\
&= \sum_n\sum_j E_{\mathrm{nf},n}E^*_{b,n-j}\exp(i(j)\Omega t) \quad (k\to j=n-k) \\
\sum_j E_{c,n}\exp(ij\Omega t) &\propto \sum_j\sum_n E_{\mathrm{nf},n}E^*_{b,n-j}\exp(ij\Omega t)
\end{aligned}
$$

Meaning:

$$
\begin{aligned}
E_{c,j} &= \sum_n E_{\mathrm{nf},n}E^*_{b,n-j} \\
&= \sum_k E_{\mathrm{nf},k}E^*_{b,k-j} \quad (n\to k) \\
E_{c,n} &= \sum_k E_{\mathrm{nf},k}E^*_{b,k-n} \quad (j\to n)
\end{aligned}
$$

The same principle goes for all the other terms in Eq. 1.10.

A.2 Back-check of equations 1.23 and 1.24

Let us try to find back $|E_{\text{nf},n}|$ from $|E_{\text{nf},n}^{\text{exp}}|$ and $\Phi_{\text{nf},n}$ from $\Phi_{\text{nf},n}^{\text{exp}}$.

For the amplitude:

$$\begin{aligned}|E_{\text{nf},n}^{\text{exp}}| &= 2.16|C|\sqrt{I_{n,2}^2 + I_{n,1}^2}\\ &= 2.16|C|2\kappa|E_{\text{nf},n}|\rho\sqrt{[J_2(2.63)\cos(\Phi_R - \Phi_{\text{nf},n})]^2 + [J_1(2.63)\sin(\Phi_R - \Phi_{\text{nf},n})]^2}\end{aligned}$$

Knowing that $J_2(2.63) = J_1(2.63) = 1/2.16$ and $|C| = 1/(2\kappa\rho)$

$$\begin{aligned}|E_{\text{nf},n}^{\text{exp}}| &= \frac{2.162\kappa\rho}{2.162\kappa\rho}|E_{\text{nf},n}|\\ |E_{\text{nf},n}^{\text{exp}}| &= |E_{\text{nf},n}|\end{aligned}$$

For the phase:

$$\begin{aligned}\Phi_{\text{nf},n}^{\text{exp}} &= \arctan\left(\frac{I_{n,1}}{I_{n,2}}\right)\\ &= \arctan\left(\frac{2\kappa|E_{\text{nf},n}|\rho J_1(2.63)\sin(\Phi_R - \Phi_{\text{nf},n})}{-2\kappa|E_{\text{nf},n}|\rho J_2(2.63)\cos(\Phi_R - \Phi_{\text{nf},n})}\right)\\ &= -\arctan\left(\frac{\sin(\Phi_R - \Phi_{\text{nf},n})}{\cos(\Phi_R - \Phi_{\text{nf},n})}\right)\\ \Phi_{\text{nf},n}^{\text{exp}} &= \Phi_{\text{nf},n} - \Phi_R\end{aligned}$$

APPENDIX B

Sources and detectors

B.1 Sources

The sources permanently available for this setup are summarized in Table B.1.

Laser	Wavelength range (nm)	Pulse duration (fs)	Max output power (mW)
HeNe	632.991	-	4
Green diode	521.6	-	28
Fusion	750 - 850	10	300
Tsunami	700 - 1000	100	300

Table B.1. Overview of the permanently available lasers sources

The most used laser source is a CW stabilized red HeNe laser (HRS015, Thorlabs GmbH). It is used for general alignment procedures as well as for measurements. For this laser, the manufacturer guaranties a wavelength of 632.991 nm and an output power of 4 mW has been measured.

Some experiments have used a green diode laser (Matchbox 0520L-15A-NI-PT-NF, Integrated Optics UAB). The manufacturer guaranties a wavelength of 521.6 ± 0.5 nm for this laser, and output powers from 0 to 28 mW can be set by changing the laser current.

The Fusion laser (Fusion Pro, FEMTOLASERS Produktions GmbH) is a femtosecond laser with a center wavelength at 800 nm and a pulse duration of about 10 fs. Thus, a wavelength range of 750 nm to 850 nm can potentially be probed in one measurement by using the nano-FTIR module. The repetition rate of this laser is 80 MHz.

The Tsunami laser (Tsunami, from Spectra-Physics Lasers Inc.) is a tunable femtosecond laser with a center wavelength that can be tuned from about 700 nm to about 1000 nm, and a pulse duration below 100 fs when mode-locked. It is pumped by a green laser (Millenia Pro, from Spectra-Physics Lasers Inc.). The Tsunami laser laser is most stable when it is mode-locked. It is however used in continuous wave mode in this thesis. The measured spectrum from this laser in continuous wave mode is plotted in Figure B.1. The repetition rate of this laser is 80 MHz.

It has to be noted that due to the number of mirrors involved in the beam path, the power at the output of the lasers is the not necessarily the same as the power entering the s-SNOM. Typically about 50% of the power would be lost, mainly after the beam expander. However, when the output power is still too high for the s-SNOM tip, a half-wave plate (AHWP10M-580, from Thorlabs GmbH) associated with a polarizer (LPNIR100-MP2, from Thorlabs GmbH) are used to attenuate the power at the input of the s-SNOM.

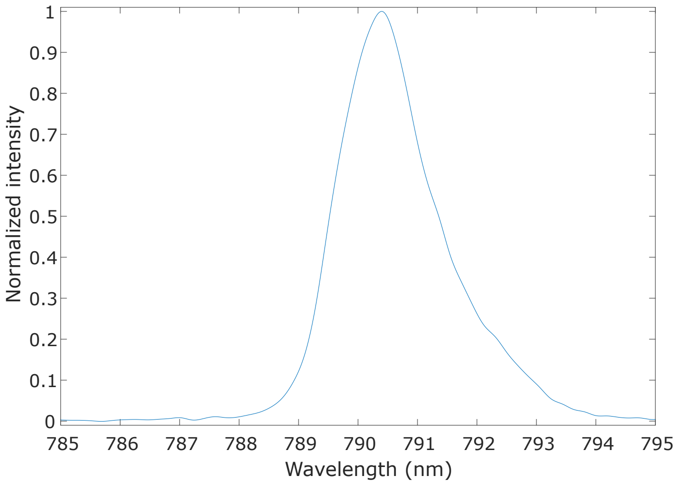

Figure B.1. Spectrum of the Tsunami laser in continuous mode, measured with the Ocean Optics spectrometer (USB4000 from Ocean Insight Inc.).

B.2 Detectors

The detector used in this thesis is a one-pixel 10-MHz adjustable photodiode (2051, from Newport Corp.).

APPENDIX C

Additional measurements of SPPs at grazing angle

This appendix shows the additional measurements of SPPs on monocrystalline gold platelets. The same platelet and same experimental configuration as for the results shown in Section 3.4.3 has been used. Both measurements were made 8 months after the measurement shown in Section 3.4.3. The figures and tables are the same as in the supplementary information from Ref. [66].

C.1 First additional measurement: $\varphi = -1.4°$

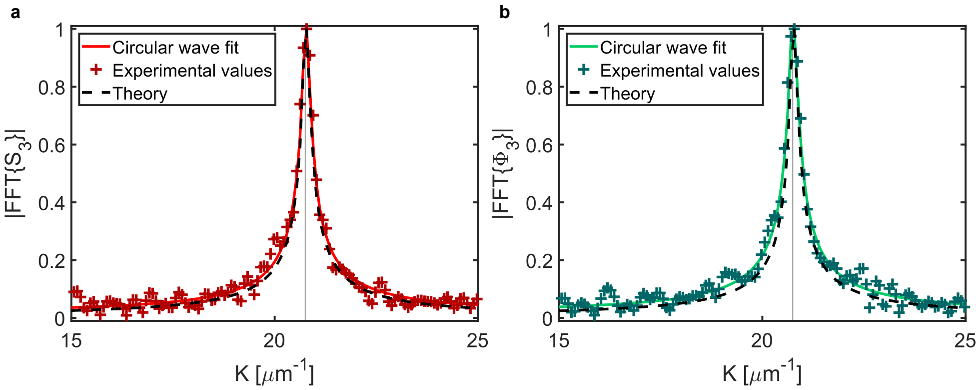

Figure C.1. Fit of amplitude and phase at grazing angle ($\varphi = -1.4°$), for a starting value $x_b = 3$ µm. (a) Fit of the tip-launched SPPs' amplitude peak. (b) Fit of the corresponding phase data.

	Amplitude		Phase		Theory
	k-space	real space	k-space	real space	-
K_{tl} (µm^{-1})	20.752 ± 0.007	20.75 ± 0.01	20.736 ± 0.004	20.743 ± 0.008	20.75
L_p^{tl} (µm)	11.8 ± 1	14 ± 2	10.6 ± 1	11.4 ± 0.1	13.65

Table C.1. Comparison of values for the wave-vector and propagation length, as obtained in real space and in Fourier space, for one starting value $x_b = 3$ µm.

	Amplitude		Phase		Theory
	k-space	real space	k-space	real space	-
K_{tl} (µm^{-1})	20.752 ± 0.006	20.754 ± 0.004	20.740 ± 0.008	20.745 ± 0.004	20.75
L_p^{tl} (µm)	11.7 ± 0.3	13.6 ± 0.8	10.7 ± 0.2	11.3 ± 0.4	13.65

Table C.2. Comparison of values for the wave-vector and propagation length, as obtained in real space and in Fourier space, for an average of 30 different starting values.

C.2 Second additional measurement: $\varphi = -0.4^\circ$

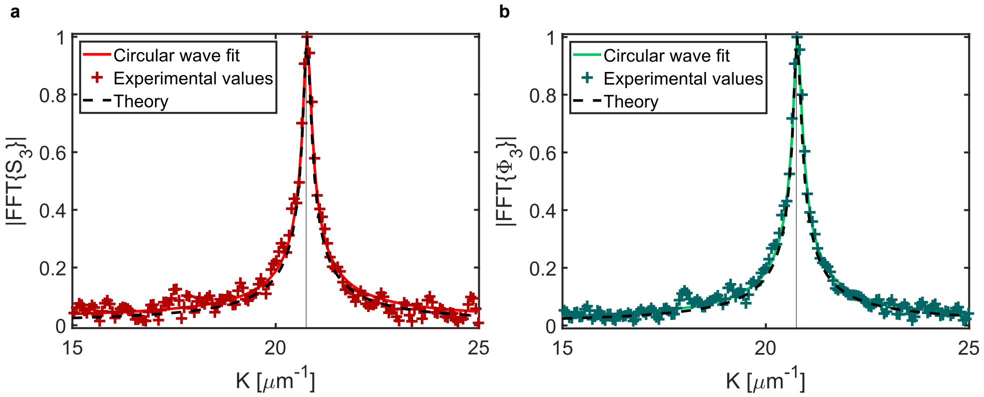

Figure C.2. Fit of amplitude and phase at grazing angle ($\varphi = -0.4^\circ$), for a starting value $x_b = 3$ µm. (a) Fit of the tip-launched SPPs' amplitude peak. (b) Fit of the corresponding phase data.

	Amplitude		Phase		Theory
	k-space	real space	k-space	real space	-
K_{tl} (µm^{-1})	20.757 ± 0.005	20.76 ± 0.01	20.754 ± 0.008	20.76 ± 0.01	20.75
L_p^{tl} (µm)	12.0 ± 0.9	13.2 ± 0.3	12.7 ± 1	14.4 ± 3	13.65

Table C.3. Comparison of values for the wave-vector and propagation length, as obtained in real space and in Fourier space, for one starting value $x_b = 3$ µm.

	Amplitude		Phase		Theory
	k-space	real space	k-space	real space	-
K_{tl} (µm^{-1})	20.758 ± 0.007	20.759 ± 0.007	20.758 ± 0.007	20.758 ± 0.003	20.75
L_p^{tl} (µm)	12.4 ± 0.5	14.8 ± 0.9	12.0 ± 0.6	13.0 ± 0.4	13.65

Table C.4. Comparison of values for the wave-vector and propagation length, as obtained in real space and in Fourier space, for an average of 30 different starting values.

The additional measurements are in agreement with the results presented in Chapter 3. The averaging over different starting values x_b results in values of K_{tl} and L_p^{tl} close to the values found for a fixed starting value x_b. Thus, the fit is stable with regards to the choice of x_b.

APPENDIX D

Transfer matrix method

D.1 Matlab code used to calculated the dispersion relation in the case of the isotropic TMM

D.1.1 Main code

```matlab
% Author: Laura N. Casses - 17.06.2022

close all
clear
clc

%% Constants

c= 299792458; % m/s
hbar=1.0546*10^-34; % in J.s
e=1.6022*10^-19; % C

%% Choice of TMDC parameters for eps

load('Lorentz_param_TMDC_220412')

%% CONSTANTS THAT CAN BE CHANGED

% ENERGY
EeV = linspace(1.5,1.7,50);

% eps TMDC
epsTMDC = 4.4*ones(1,length(EeV));
j=1;
for i=1:10
    epsTMDC = epsTMDC + cf(j)./(cf(j+1)^2 -EeV.^2 -1i*cf(j+2).*EeV);
    j=j+3;
end

% eps dielectric materials
epsD=1; % vacuum or air
epsAlO = (1.61)^2;

% eps Gold
[E_JC,E_N,E_MoS2,E_WS2,E_WSe2,E_MoSe2,eps_AuJC,eps_AuN,eps_MoS2,eps_WS2,...
```

```
    eps_WSe2,eps_MoSe2] = ImportData(); % All energies are in J.
E_N = E_N/e;
i_beg = find(E_N>1.49 & E_N<1.51);
i_end = find(E_N<1.81 & E_N>1.79);

epsAu = interp1(E_N(i_beg:i_end),eps_AuN(i_beg:i_end),EeV,'spline');

% Thickness of materials used
d_TMDC = 15E-9; % Effective thickness of WSe2, in m
d_AlO = 2E-9; % Effective thickness of AlOx, in m

%% Solve for q with TMM

omega = EeV*e/hbar; % in m^{-1}
sigma = 0;

Solution=zeros(length(EeV),1);
MatrixSol = zeros(length(EeV),1);

for i=1:length(EeV)
    syms q
    M = Mmatrix_4L_V02(epsD,epsTMDC(i),epsAlO,epsAu(i),d_TMDC,d_AlO,...
        omega(i),sigma,q);

    eqn = M(1,1)==0;
    if i ==1 || Solution(i-1)==0
        sol = 0;
        count =1;
        while sol == 0 && count <4
            Q=vpasolve(eqn,q,[sqrt(1).*EeV(i)*e/hbar/c+1i*7E4 ...
                sqrt(3).*EeV(i)*e/hbar/c+1i*5E5],'Random',true); %in m^{-1}
            s=isempty(Q);
            if s==0
                sol = 1;
                disp('Solution!')
            else
                fprintf('No solution... i= %3d\n',i)
                count = count +1;
            end
        end
    else
        Q=vpasolve(eqn,q,Solution(i-1));
    end

    s=isempty(Q);
    if s==1
        Solution(i)=0;
    else
        Solution(i)=Q(1,1);
        Matrix= Mmatrix_4L_V02(epsD,epsTMDC(i),epsAlO,epsAu(i),d_TMDC,...
            d_AlO,omega(i),sigma,Solution(i));
        MatrixSol(i) = Matrix(1,1);
    end
end

```

```matlab
%% Comparison with Goncalves formula

omegaDc = EeV*e/hbar/c; % omega(s^-1)/c

sigma = 0;

Solution2=zeros(length(EeV),1);
for i=1:length(EeV)
    syms q
    eqn1 = real(q)>0;
    eqn2 = imag(q)>0;
    eqn = epsD./sqrt(q.^2-epsD*omegaDc(i)^2)+epsAu(i)./sqrt(q.^2-...
        epsAu(i)*omegaDc(i)^2)==0;
    eqns = [eqn1 eqn2 eqn];
    Q=solve(eqns,q);
    s=isempty(Q);
    if s==1
        Solution2(i,:)=0;
    else
        Solution2(i,:)=Q(1,1);
    end
end

Solution2 = double(Solution2);

%% Save data

% save('DispRel_Air11.65nmTMDCAlOAu.mat','Solution')
% save('DispRel_AirAu.mat','Solution2')

%% Plot result

yaxis=EeV;
xaxis=real(Solution)*10^-6; % in um^-1
xaxis2=real(Solution2)*10^-6; % in um^-1
q_light = sqrt(epsD).*EeV*e/hbar/c*10^-6;

%Plot
figure;
hold on
plot(xaxis,yaxis,'k')
plot(xaxis2,yaxis,'g--')

% light line
plot(q_light,yaxis,'r--') % plot light line (in vacuum!)
hold off

xlabel('q (µm^{-1})')
ylabel('Energy (eV)')
legend('Dispersion relation','Air/gold interface','Light line',...
    'Location','northwest')


ylim([1.5 1.7])
axis([7.5 10.5 1.5 1.7]) % Select the axes boundaries
```

```
set(gcf, 'Position',  [100,100, 460, 370])
% title('Dispersion relation - 10 nm WSe_2 with A exciton')
```

SC_Disp_4L_V07.m

D.1.2 Total matrix function

```
function M = Mmatrix_4L_V02(epsD,epsTMDC,epsAlO,epsAu,d_TMDC,d_AlO,omega,sigma,q)
%UNTITLED13 Summary of this function goes here
%   Detailed explanation goes here
    D12p = TransmissionMatrixP_V02(q,omega,epsD,epsTMDC,sigma);
    P2 = PropagationMatrix_V02(q,omega,epsTMDC,d_TMDC);
    D23p = TransmissionMatrixP_V02(q,omega,epsTMDC,epsAlO,sigma);
    P3 = PropagationMatrix_V02(q,omega,epsAlO,d_AlO);
    D34p = TransmissionMatrixP_V02(q,omega,epsAlO,epsAu,sigma);

    M= D12p*P2*D23p*P3*D34p; % Total transfer matrix
end
```

Mmatrix_4L_V02.m

D.1.3 Transmission matrix function

```
function Dp = TransmissionMatrixP_V02(q_var,omega,eps1,eps2,sigma)
% TransmissionMatrix: Calculates the transmission matrix through an interface,
%                       from medum 1 to medium 2, with 2D material in between - or not.
% INPUT:
%       - q_var: in plane wavevector (real vector)
%       - omega: oscillating frequency of the light
%       - eps1, eps2: dielectric of media 1 and 2, respectively (number)
%       - sigma: conductivity at the interface (number)
% OUTPUT: Calculated transmission matrix Dp, for p polarization

%% Universal constants

epsilon_0 = 8.85*10^-12;
c= 299792458;

%% Other constants
k1z = sqrt(q_var.^2-eps1*omega^2/c^2);
k2z = sqrt(q_var.^2-eps2*omega^2/c^2);

xi_p = 1i*sigma*k2z./(epsilon_0*eps2*omega); % doesn't matter for our bulk case because sigma=0 (no boundary material)
eta_p = eps1*k2z./(eps2*k1z);

%% Matrix
```

```

Dp = sym(zeros(2,2,length(q_var)));

for i=1:length(q_var)
    Dp(1,1,i)=(1+eta_p(i)+xi_p(i))/2;
    Dp(1,2,i)=(1-eta_p(i)-xi_p(i))/2;
    Dp(2,1,i)=(1-eta_p(i)+xi_p(i))/2;
    Dp(2,2,i)=(1+eta_p(i)-xi_p(i))/2;
end

end
```

TransmissionMatrixP_V02.m

D.1.4 Propagation matrix function

```
function P = PropagationMatrix_V02(q_var,omega,eps,d)
% TransmissionMatrix: Calculates the propagation matrix in a medium,
% INPUT:
%       - q_var: in plane wavevector (real vector)
%       - omega: oscillating frequency of the light
%       - eps: dielectric of the medium
%       - d: thickness of the medium layer
% OUTPUT: Calculated propagation matrix P, for any polarization

%% Universal constants

c= 299792458;

%% Other constants
kz = sqrt(q_var.^2-eps*omega^2/c^2);

%% Matrix

P = sym(zeros(2,2,length(q_var)));

for i=1:length(q_var)
    P(1,1,i) = exp(kz(i)*d);
    P(2,2,i) = exp(-kz(i)*d);
end

end
```

PropagationMatrix_V02.m

D.2 Derivation of the impedance coefficients for uniaxial anisotropic crystals

For a plane wave without source currents, the Maxwell's equation $\nabla \times \mathbf{H} = \mathbf{j} + \frac{\partial \mathbf{D}}{\partial t}$ leads to

$$\mathbf{k} \times \mathbf{H} = -\omega\varepsilon_0 \overleftrightarrow{\varepsilon} \mathbf{E} \tag{D.1}$$

In the case of a uniaxial anisotropic crystal and *p*-polarization, this leads to the equation

$$\begin{cases} k_z H_y & = \omega\varepsilon_0\varepsilon_{ord} E_x \\ q H_y & = -\omega\varepsilon_0\varepsilon_e E_z \end{cases}, \tag{D.2}$$

with all notation being the same as in Chapter 4. This means the electric field components can be expressed as

$$\begin{cases} E_x & = \frac{k_z}{\omega\varepsilon_0\varepsilon_{ord}} H_y \\ E_z & = -\frac{q}{\omega\varepsilon_0\varepsilon_e} H_y \end{cases}. \tag{D.3}$$

Now, we have to find the anisotropic impedance Z_A that satisfies the equation $\hat{\mathbf{k}} \times \mathbf{E} = Z_A \mathbf{H}$, where $\hat{\mathbf{k}}$ is the unitary vector in the same direction as $\mathbf{k}$. Knowing that $\hat{\mathbf{k}} = \mathbf{k}/||\mathbf{k}||$ (where $||\mathbf{k}|| = \sqrt{q^2 + k_z^2}$ is the norm of $\mathbf{k}$) and $\mathbf{k} \times \mathbf{E} = \omega\mathbf{B} = \omega\mu_0\mathbf{H}$, we get

$$\frac{1}{||\mathbf{k}||}(\omega\mu_0\mathbf{H}) = Z_A\mathbf{H}. \tag{D.4}$$

Thus, the anisotropic impedance can be expressed as

$$Z_A = \frac{\omega\mu_0}{||\mathbf{k}||}. \tag{D.5}$$

Finally, we can use the relation $\omega = c\sqrt{\frac{q^2}{\varepsilon_e} + \frac{k_z^2}{\varepsilon_{ord}}}$, valid in the case of *p*-polarization, to get:

$$Z_A = \sqrt{\frac{\mu_0}{\varepsilon_0}}\sqrt{\frac{1}{q^2 + k_z^2}\left(\frac{q^2}{\varepsilon_e} + \frac{k_z^2}{\varepsilon_{ord}}\right)}. \tag{D.6}$$

This expression can be reduced to the isotropic impedance Z_i of medium i (see Equation 4.17), in the case of $\varepsilon_{ord} = \varepsilon_e$. Note that in this derivation we have considered that the relative permittivity of medium i, μ_i, is equal to 1.

Bibliography

[1] T. Araki, "The history of optical microscope," *Mechanical Engineering Reviews*, vol. 4, no. 1, pp. 16–00242–16–00242, 2017.

[2] L. Novotny and B. Hecht, *Principles of Nano-Optics.* Cambridge University Press, 2012.

[3] E. Synge, "Xxxviii. a suggested method for extending microscopic resolution into the ultra-microscopic region," *The London, Edinburgh, and Dublin Philosophical Magazine and Journal of Science*, vol. 6, no. 35, pp. 356–362, 1928.

[4] D. W. Pohl, W. Denk, and M. Lanz, "Optical stethoscopy: Image recording with resolution $\lambda/20$," *Applied physics letters*, vol. 44, no. 7, pp. 651–653, 1984.

[5] Y. Inouye and S. Kawata, "Near-field scanning optical microscope with a metallic probe tip," *Opt. Lett.*, vol. 19, pp. 159–161, Feb 1994.

[6] J.-J. Greffet and R. Carminati, "Image formation in near-field optics," *Progress in Surface Science*, vol. 56, no. 3, pp. 133–237, 1997.

[7] J. M. Atkin, S. Berweger, A. C. Jones, and M. B. Raschke, "Nano-optical imaging and spectroscopy of order, phases, and domains in complex solids," *Advances in Physics*, vol. 61, no. 6, pp. 745–842, 2012.

[8] A. Andryieuski, V. A. Zenin, R. Malureanu, V. S. Volkov, S. I. Bozhevolnyi, and A. V. Lavrinenko, "Direct characterization of plasmonic slot waveguides and nanocouplers," *Nano Lett.*, vol. 14, no. 7, pp. 3925–3929, 2014.

[9] F. Walla, F. Bürkle, I. Sinev, M. M. Wiecha, N. Mecklenbeck, K. Ladutenko, R. Malureanu, F. Komissarenko, A. Lavrinenko, A. Bogdanov, *et al.*, "Near-field observation of guided-mode resonances on a metasurface via dielectric nanosphere excitation," *ACS Photonics*, vol. 5, no. 11, pp. 4238–4243, 2018.

[10] Y. Lebsir, S. Boroviks, M. Thomaschewski, S. I. Bozhevolnyi, and V. A. Zenin, "Ultimate limit for optical losses in gold, revealed by quantitative near-field microscopy," *Nano Letters*, vol. 22, no. 14, pp. 5759–5764, 2022.

[11] A. A. Govyadinov, I. Amenabar, F. Huth, P. S. Carney, and R. Hillenbrand, “Quantitative measurement of local infrared absorption and dielectric function with tip-enhanced near-field microscopy,” *The Journal of Physical Chemistry Letters*, vol. 4, no. 9, pp. 1526–1531, 2013.

[12] F. Alfaro-Mozaz, P. Alonso-González, S. Vélez, I. Dolado, S. Mastel, F. Casanova, L. E. Hueso, P. Li, A. Y. Nikitin, R. Hillenbrand, *et al.*, “Nanoimaging of resonating hyperbolic polaritons in linear boron nitride antennas,” *Nature communications*, vol. 8, no. 1, pp. 1–8, 2017.

[13] L. Gomez, R. Bachelot, A. Bouhelier, G. P. Wiederrecht, S. hui Chang, S. K. Gray, F. Hua, S. Jeon, J. A. Rogers, M. E. Castro, S. Blaize, I. Stefanon, G. Lerondel, and P. Royer, “Apertureless scanning near-field optical microscopy: a comparison between homodyne and heterodyne approaches,” *J. Opt. Soc. Am. B*, vol. 23, pp. 823–833, 05 2006.

[14] N. Ocelic, A. Huber, and R. Hillenbrand, “Pseudoheterodyne detection for background-free near-field spectroscopy,” *Applied Physics Letters*, vol. 89, no. 10, p. 101124, 2006.

[15] S. Amarie, T. Ganz, and F. Keilmann, “Mid-infrared near-field spectroscopy,” *Opt. Express*, vol. 17, pp. 21794–21801, Nov 2009.

[16] E. Yoxall, M. Schnell, A. Y. Nikitin, O. Txoperena, A. Woessner, M. B. Lundeberg, F. Casanova, L. E. Hueso, F. H. Koppens, and R. Hillenbrand, “Direct observation of ultraslow hyperbolic polariton propagation with negative phase velocity,” *Nature Photonics*, vol. 9, no. 10, pp. 674–678, 2015.

[17] J. Taboada-Gutiérrez, G. Álvarez-Pérez, J. Duan, W. Ma, K. Crowley, I. Prieto, A. Bylinkin, M. Autore, H. Volkova, K. Kimura, T. Kimura, M.-H. Berger, S. Li, Q. Bao, X. P. A. Gao, A. Y. Errea, Ion and. Nikitin, R. Hillenbrand, J. Martín-Sánchez, and P. Alonso-González, “Broad spectral tuning of ultra-low-loss polaritons in a van der waals crystal by intercalation,” *Nat. Mater.*, vol. 19, no. 9, pp. 964–968, 2020.

[18] S. A. Maier, *Plasmonics: Fundamentals and Applications.* Springer Science & Business Media, 2007.

[19] D. K. Gramotnev and S. I. Bozhevolnyi, “Plasmonics beyond the diffraction limit,” *Nature photonics*, vol. 4, no. 2, pp. 83–91, 2010.

[20] S. Roh, T. Chung, and B. Lee, “Overview of the characteristics of micro-and nano-structured surface plasmon resonance sensors,” *Sensors*, vol. 11, no. 2, pp. 1565–1588, 2011.

[21] S. Celiksoy, W. Ye, K. Wandner, K. Kaefer, and C. Sonnichsen, “Intensity-based single particle plasmon sensing,” *Nano Letters*, vol. 21, no. 5, pp. 2053–2058, 2021.

[22] V. E. Ferry, J. N. Munday, and H. A. Atwater, “Design considerations for plasmonic photovoltaics,” *Adv. Mater.*, vol. 22, no. 43, pp. 4794–4808, 2010.

[23] S. Schmidt, B. Piglosiewicz, D. Sadiq, J. Shirdel, J. S. Lee, P. Vasa, N. Park, D.-S. Kim, and C. Lienau, “Adiabatic nanofocusing on ultrasmooth single-crystalline gold tapers creates a 10-nm-sized light source with few-cycle time resolution,” *ACS Nano*, vol. 6, no. 7, pp. 6040–6048, 2012.

[24] J. Kern, R. Kullock, J. Prangsma, M. Emmerling, M. Kamp, and B. Hecht, “Electrically driven optical antennas,” *Nat. Photon.*, vol. 9, no. 9, pp. 582–586, 2015.

[25] J. B. Khurgin, “How to deal with the loss in plasmonics and metamaterials,” *Nature nanotechnology*, vol. 10, no. 1, pp. 2–6, 2015.

[26] R. Deshpande, V. A. Zenin, F. Ding, N. A. Mortensen, and S. I. Bozhevolnyi, “Direct characterization of near-field coupling in gap plasmon-based metasurfaces,” *Nano Letters*, vol. 18, no. 10, pp. 6265–6270, 2018.

[27] S. V. Jayanti, J. H. Park, A. Dejneka, D. Chvostova, K. M. McPeak, X. Chen, S.-H. Oh, and D. J. Norris, “Low-temperature enhancement of plasmonic performance in silver films,” *Opt. Mater. Express*, vol. 5, pp. 1147–1155, May 2015.

[28] D. I. Yakubovsky, A. V. Arsenin, Y. V. Stebunov, D. Y. Fedyanin, and V. S. Volkov, “Optical constants and structural properties of thin gold films,” *Opt. Express*, vol. 25, pp. 25574–25587, Oct 2017.

[29] X. Wu, R. Kullock, E. Krauss, and B. Hecht, “Single-crystalline gold microplates grown on substrates by solution-phase synthesis,” *Cryst. Res. Technol.*, vol. 50, no. 8, pp. 595–602, 2015.

[30] B. Hoffmann, M. Bashouti, T. Feichtner, M. Mačković, C. Dieker, A. Salaheldin, P. Richter, O. Gordan, D. Zahn, E. Spiecker, and S. Christiansen, “New insights into colloidal gold flakes: structural investigation, micro-ellipsometry and thinning procedure towards ultrathin monocrystalline layers,” *Nanoscale*, vol. 8, no. 8, pp. 4529–4536, 2016.

[31] J.-S. Huang, V. Callegari, P. Geisler, C. Brüning, J. Kern, J. C. Prangsma, X. Wu, T. Feichtner, J. Ziegler, P. Weinmann, M. Kamp, A. Forchel, P. Biagioni, U. Sennhauser, and B. Hecht, “Atomically flat single-crystalline gold nanostructures for plasmonic nanocircuitry,” *Nat. Commun.*, vol. 1, no. 1, pp. 1–8, 2010.

[32] M. Prämassing, M. Liebtrau, H. Schill, S. Irsen, and S. Linden, “Interferometric near-field characterization of plasmonic slot waveguides in single-and polycrystalline gold films,” *Opt. Express*, vol. 28, no. 9, pp. 12998–13007, 2020.

[33] S. Boroviks, F. Todisco, N. A. Mortensen, and S. I. Bozhevolnyi, "Use of monocrystalline gold flakes for gap plasmon-based metasurfaces operating in the visible," *Opt. Mater. Express*, vol. 9, no. 11, pp. 4209–4217, 2019.

[34] S. Boroviks, Z.-H. Lin, V. A. Zenin, M. Ziegler, A. Dellith, P. Gonçalves, C. Wolff, S. I. Bozhevolnyi, J.-S. Huang, and N. A. Mortensen, "Extremely confined gap plasmon modes: when nonlocality matters," *Nature Communications*, vol. 13, no. 1, pp. 1–8, 2022.

[35] F. Walla, M. M. Wiecha, N. Mecklenbeck, S. Beldi, F. Keilmann, M. D. Thomson, and H. G. Roskos, "Anisotropic excitation of surface plasmon polaritons on a metal film by a scattering-type scanning near-field microscope with a non-rotationally-symmetric probe tip," *Nanophotonics*, vol. 7, no. 1, pp. 269–276, 2018.

[36] K. J. Kaltenecker, E. Krauss, L. Casses, M. Geisler, B. Hecht, N. A. Mortensen, P. U. Jepsen, and N. Stenger, "Mono-crystalline gold platelets: a high-quality platform for surface plasmon polaritons," *Nanophotonics*, vol. 9, no. 2, pp. 509–522, 2020.

[37] F. Xia, H. Wang, D. Xiao, M. Dubey, and A. Ramasubramaniam, "Two-dimensional material nanophotonics," *Nature Photonics*, vol. 8, no. 12, pp. 899–907, 2014.

[38] L. Zhao, Q. Shang, M. Li, Y. Liang, C. Li, and Q. Zhang, "Strong exciton-photon interaction and lasing of two-dimensional transition metal dichalcogenide semiconductors," *Nano Research*, vol. 14, no. 6, pp. 1937–1954, 2021.

[39] P. Fathi-Hafshejani, N. Azam, L. Wang, M. A. Kuroda, M. C. Hamilton, S. Hasim, and M. Mahjouri-Samani, "Two-dimensional-material-based field-effect transistor biosensor for detecting covid-19 virus (sars-cov-2)," *ACS Nano*, vol. 15, no. 7, pp. 11461–11469, 2021.

[40] C. Li, Q. Cao, F. Wang, Y. Xiao, Y. Li, J.-J. Delaunay, and H. Zhu, "Engineering graphene and tmds based van der waals heterostructures for photovoltaic and photoelectrochemical solar energy conversion," *Chemical Society Reviews*, vol. 47, no. 13, pp. 4981–5037, 2018.

[41] A. Chernikov, T. C. Berkelbach, H. M. Hill, A. Rigosi, Y. Li, B. Aslan, D. R. Reichman, M. S. Hybertsen, and T. F. Heinz, "Exciton binding energy and non-hydrogenic rydberg series in monolayer ws2," *Physical review letters*, vol. 113, no. 7, p. 076802, 2014.

[42] K. He, N. Kumar, L. Zhao, Z. Wang, K. F. Mak, H. Zhao, and J. Shan, "Tightly bound excitons in monolayer wse 2," *Physical review letters*, vol. 113, no. 2, p. 026803, 2014.

[43] B. Munkhbat, P. Wróbel, T. J. Antosiewicz, and T. O. Shegai, “Optical constants of several multilayer transition metal dichalcogenides measured by spectroscopic ellipsometry in the 300–1700 nm range: High index, anisotropy, and hyperbolicity,” *ACS Photonics*, vol. 9, no. 7, pp. 2398–2407, 2022.

[44] G. Ermolaev, D. Grudinin, Y. Stebunov, K. V. Voronin, V. Kravets, J. Duan, A. Mazitov, G. Tselikov, A. Bylinkin, S. Yakubovsky, DI Novikov, D. Baranov, N. AY, I. Kruglov, T. Shegai, P. Alonso-González, A. Grigorenko, A. Arsenin, K. Novoselov, and V. Volkov, “Giant optical anisotropy in transition metal dichalcogenides for next-generation photonics,” *Nature communications*, vol. 12, no. 1, pp. 1–8, 2021.

[45] X. Li, H. Liu, C. Ke, W. Tang, M. Liu, F. Huang, Y. Wu, Z. Wu, and J. Kang, “Review of anisotropic 2d materials: controlled growth, optical anisotropy modulation, and photonic applications,” *Laser & Photonics Reviews*, vol. 15, no. 12, p. 2100322, 2021.

[46] S. G. Menabde, S. Boroviks, J. Ahn, J. T. Heiden, K. Watanabe, T. Taniguchi, T. Low, D. K. Hwang, N. A. Mortensen, and M. S. Jang, “Near-field probing of image phonon-polaritons in hexagonal boron nitride on gold crystals,” *Science Advances*, vol. 8, no. 28, p. eabn0627, 2022.

[47] Z. Fei, A. Rodin, G. O. Andreev, W. Bao, A. McLeod, M. Wagner, L. Zhang, Z. Zhao, M. Thiemens, G. Dominguez, M. M. Fogler, A. H. C. Neto, C. N. Lau, F. Keilmann, and D. N. Basov, “Gate-tuning of graphene plasmons revealed by infrared nano-imaging,” *Nature*, vol. 487, no. 7405, pp. 82–85, 2012.

[48] J. Chen, M. Badioli, P. Alonso-González, S. Thongrattanasiri, F. Huth, J. Osmond, M. Spasenović, A. Centeno, A. Pesquera, P. Godignon, P. Godignon, A. Z. Elorza, N. Camara, F. J. G. de Abajo, R. Hillenbrand, and F. H. L. Koppens, “Optical nano-imaging of gate-tunable graphene plasmons,” *Nature*, vol. 487, no. 7405, pp. 77–81, 2012.

[49] A. Woessner, M. B. Lundeberg, Y. Gao, A. Principi, P. Alonso-González, M. Carrega, K. Watanabe, T. Taniguchi, G. Vignale, M. Polini, J. Hone, R. Hillenbrand, and F. H. L. Koppens, “Highly confined low-loss plasmons in graphene–boron nitride heterostructures,” *Nat. Mater.*, vol. 14, no. 4, pp. 421–425, 2015.

[50] W. Ma, P. Alonso-González, S. Li, A. Y. Nikitin, J. Yuan, J. Martín-Sánchez, J. Taboada-Gutiérrez, I. Amenabar, P. Li, S. Vélez, C. Tollan, Z. Dai, Y. Zhang, S. Sriram, K. Kalantar-Zadeh, S.-T. Lee, R. Hillenbrand, and Q. Bao, “In-plane anisotropic and ultra-low-loss polaritons in a natural van der waals crystal,” *Nature*, vol. 562, no. 7728, pp. 557–562, 2018.

[51] F. Hu, Y. Luan, M. Scott, J. Yan, D. Mandrus, X. Xu, and Z. Fei, “Imaging exciton–polariton transport in mose2 waveguides,” *Nature Photonics*, vol. 11, no. 6, pp. 356–360, 2017.

[52] F. Hu, Y. Luan, J. Speltz, D. Zhong, C. H. Liu, J. Yan, D. G. Mandrus, X. Xu, and Z. Fei, "Imaging propagative exciton polaritons in atomically thin wse$_2$ waveguides," *Phys. Rev. B*, vol. 100, p. 121301, Sep 2019.

[53] S. Zhang, B. Li, X. Chen, F. L. Ruta, Y. Shao, A. J. Sternbach, A. McLeod, Z. Sun, L. Xiong, S. Moore, X. Xu, W. Wu, S. Shabani, L. Zhou, Z. Wang, F. Mooshammer, E. Ray, N. Wilson, P. J. Schuck, C. R. Dean, A. N. Pasupathy, M. Lipson, X. Xu, X. Zhu, A. J. Millis, M. Liu, J. C. Hone, and D. N. Basov, "Nano-spectroscopy of excitons in atomically thin transition metal dichalcogenides," *Nature communications*, vol. 13, no. 1, pp. 1–8, 2022.

[54] A. Bylinkin, M. Schnell, M. Autore, F. Calavalle, P. Li, J. Taboada-Gutièrrez, S. Liu, J. H. Edgar, F. Casanova, L. E. Hueso, P. Alonso-Gonzalez, A. Y. Nikitin, and R. Hillenbrand, "Real-space observation of vibrational strong coupling between propagating phonon polaritons and organic molecules," *Nat. Photon.*, vol. 15, no. 3, pp. 197–202, 2021.

[55] G. Binnig, C. F. Quate, and C. Gerber, "Atomic force microscope," *Phys. Rev. Lett.*, vol. 56, pp. 930–933, Mar 1986.

[56] P. Eaton and P. West, *Atomic Force Microscopy.* Oxford University Press, 2010.

[57] *neaSNOM Scanning Near-Field Optical Microscope: User Manual - neaSCAN Version 1.3.* Neaspec GmbH, February 2016.

[58] B. Knoll and F. Keilmann, "Enhanced dielectric contrast in scattering-type scanning near-field optical microscopy," *Optics Communications*, vol. 182, no. 4, pp. 321–328, 2000.

[59] F. Keilmann and R. Hillenbrand, "Near-field microscopy by elastic light scattering from a tip," *Phil. Trans. R. Soc. A*, vol. 362, no. 1817, pp. 787–805, 2004.

[60] Nenad Ocelic, *Quantitative Near-field Phonon-polaritons Spectroscopy.* PhD thesis, Technischen Universität Munchen, Aug. 2007.

[61] A. Cvitkovic, N. Ocelic, and R. Hillenbrand, "Analytical model for quantitative prediction of material contrasts in scattering-type near-field optical microscopy," *Opt. Express*, vol. 15, pp. 8550–8565, Jul 2007.

[62] B. Hauer, A. P. Engelhardt, and T. Taubner, "Quasi-analytical model for scattering infrared near-field microscopy on layered systems," *Opt. Express*, vol. 20, pp. 13173–13188, Jun 2012.

[63] K. G. Wirth, H. Linnenbank, T. Steinle, L. Banszerus, E. Icking, C. Stampfer, H. Giessen, and T. Taubner, "Tunable s-snom for nanoscale infrared optical measurement of electronic properties of bilayer graphene," *ACS Photonics*, vol. 8, no. 2, pp. 418–423, 2021.

[64] A. García-Etxarri, I. Romero, F. J. García de Abajo, R. Hillenbrand, and J. Aizpurua, "Influence of the tip in near-field imaging of nanoparticle plasmonic modes: Weak and strong coupling regimes," *Phys. Rev. B*, vol. 79, p. 125439, Mar 2009.

[65] H. Sumikura, T. Wang, P. Li, A.-K. U. Michel, A. Heßler, L. Jung, M. Lewin, M. Wuttig, D. N. Chigrin, and T. Taubner, "Highly confined and switchable mid-infrared surface phonon polariton resonances of planar circular cavities with a phase change material," *Nano Letters*, vol. 19, no. 4, pp. 2549–2554, 2019.

[66] L. N. Casses, K. J. Kaltenecker, S. Xiao, M. Wubs, and N. Stenger, "Quantitative near-field characterization of surface plasmon polaritons on monocrystalline gold platelets," *Opt. Express*, vol. 30, pp. 11181–11191, Mar 2022.

[67] Mike Prämassing, *Experimental Near-Field Characterization of Plasmonic Nanostructures.* PhD thesis, Rheinische Friedrich-Wilhelms-Universität Bonn, Jan. 2021.

[68] P. R. Griffiths and J. A. de Haseth, *Fourier Transform Infrared Spectrometry.* john Wiley & Sons, 1986.

[69] F. Huth, M. Schnell, J. Wittborn, N. Ocelic, and R. Hillenbrand, "Infrared-spectroscopic nanoimaging with a thermal source," *Nature materials*, vol. 10, no. 5, pp. 352–356, 2011.

[70] F. Huth, A. Govyadinov, S. Amarie, W. Nuansing, F. Keilmann, and R. Hillenbrand, "Nano-ftir absorption spectroscopy of molecular fingerprints at 20 nm spatial resolution," *Nano Letters*, vol. 12, no. 8, pp. 3973–3978, 2012.

[71] Florian Huth, *Nanoscale Infrared Near-Field Spectroscopy.* PhD thesis, Universidad del Pais Vasco, Jan. 2015.

[72] M. Fox, *Optical Properties of Solids.* Oxford University Press, 2010.

[73] P. B. Johnson and R.-W. Christy, "Optical constants of the noble metals," *Phys. Rev. B*, vol. 6, no. 12, p. 4370, 1972.

[74] T. Rangel, D. Kecik, P. E. Trevisanutto, G.-M. Rignanese, H. Van Swygenhoven, and V. Olevano, "Band structure of gold from many-body perturbation theory," *Phys. Rev. B*, vol. 86, p. 125125, Sep 2012.

[75] A. D. Rakić, A. B. Djurišić, J. M. Elazar, and M. L. Majewski, "Optical properties of metallic films for vertical-cavity optoelectronic devices," *Appl. Opt.*, vol. 37, pp. 5271–5283, Aug 1998.

[76] R. L. Olmon, B. Slovick, T. W. Johnson, D. Shelton, S.-H. Oh, G. D. Boreman, and M. B. Raschke, "Optical dielectric function of gold," *Phys. Rev. B*, vol. 86, no. 23, p. 235147, 2012.

[77] K. M. McPeak, S. V. Jayanti, S. J. P. Kress, S. Meyer, S. Iotti, A. Rossinelli, and D. J. Norris, “Plasmonic films can easily be better: Rules and recipes,” *ACS Photonics*, vol. 2, no. 3, pp. 326–333, 2015.

[78] E. Krauss, R. Kullock, X. Wu, P. Geisler, N. Lundt, M. Kamp, and B. Hecht, “Controlled growth of high-aspect-ratio single-crystalline gold platelets,” *Crystal Growth & Design*, vol. 18, no. 3, pp. 1297–1302, 2018.

[79] J. Barnett, D. Wendland, M. Lewin, K. Wirth, A. Heßler, and T. Taubner, “Investigation of low-confinement surface phonon polariton launching on sic and srtio3 using scanning near-field optical microscopy,” *Applied Physics Letters*, vol. 120, no. 21, p. 211107, 2022.

[80] S. Dai, Z. Fei, Q. Ma, A. Rodin, M. Wagner, A. McLeod, M. Liu, W. Gannett, W. Regan, K. Watanabe, T. Taniguchi, M. Thiemens, G. Dominguez, A. H. C. Neto, A. Zettl, F. Keilmann, P. Jarillo-Herrero, M. M. Fogler, and D. N. Basov, “Tunable phonon polaritons in atomically thin van der waals crystals of boron nitride,” *Science*, vol. 343, no. 6175, pp. 1125–1129, 2014.

[81] E. Krauss, R. Kullock, X. Wu, P. Geisler, N. Lundt, M. Kamp, and B. Hecht, “Controlled growth of high-aspect-ratio single-crystalline gold platelets,” *Cryst. Growth Des.*, vol. 18, no. 3, pp. 1297–1302, 2018.

[82] M. Großmann, M. Black, J. Jaruschewski, A. Klick, T. Leißner, J. Fiutowski, H.-G. Rubahn, and M. Bauer, “Micro-spectroscopy of buried short-range surface plasmon polaritons supported by thin polycrystalline gold films,” *Plasmonics*, vol. 16, no. 3, pp. 737–746, 2021.

[83] M. T. Aguilar-Gama, E. Ramírez-Morales, Z. Montiel-González, A. Mendoza-Galván, M. Sotelo-Lerma, P. Nair, and H. Hu, “Structure and refractive index of thin alumina films grown by atomic layer deposition,” *J. Mater. Sci.: Mater. Electron.*, vol. 26, no. 8, pp. 5546–5552, 2015.

[84] P. U. Jepsen, “Phase retrieval in terahertz time-domain measurements: a “how to” tutorial,” *Journal of Infrared, Millimeter, and Terahertz Waves*, vol. 40, no. 4, pp. 395–411, 2019.

[85] Y. Li, N. Zhou, E. C. Kinzel, X. Ren, and X. Xu, “The origin of interferometric effect involving surface plasmon polariton in scattering near-field scanning optical microscopy,” *Opt. Express*, vol. 22, no. 3, pp. 2965–2972, 2014.

[86] D. Tranca, S. Stanciu, R. Hristu, C. Stoichita, S. Tofail, and G. Stanciu, “High-resolution quantitative determination of dielectric function by using scattering scanning near-field optical microscopy,” *Scientific reports*, vol. 5, no. 1, pp. 1–9, 2015.

[87] K. J. Kaltenecker, S. Rao DS, M. Rasmussen, H. B. Lassen, E. J. Kelleher, E. Krauss, B. Hecht, N. A. Mortensen, L. Grüner-Nielsen, C. Markos, O. Bang, N. Stenger, and P. U. Jepsen, "Near-infrared nanospectroscopy using a low-noise supercontinuum source," *APL Photonics*, vol. 6, no. 6, p. 066106, 2021.

[88] "The Mathworks, Inc. amplitude estimation and zero padding." `https://se.mathworks.com/help/signal/ug/amplitude-estimation-and-zero-padding.html`. Accessed: 2021-12-13.

[89] K. S. Novoselov, A. K. Geim, S. V. Morozov, D.-e. Jiang, Y. Zhang, S. V. Dubonos, I. V. Grigorieva, and A. A. Firsov, "Electric field effect in atomically thin carbon films," *science*, vol. 306, no. 5696, pp. 666–669, 2004.

[90] S. Haastrup, M. Strange, M. Pandey, T. Deilmann, P. S. Schmidt, N. F. Hinsche, M. N. Gjerding, D. Torelli, P. M. Larsen, A. C. Riis-Jensen, J. Gath, K. W. Jacobsen, J. J. Mortensen, T. Olsen, and K. S. Thygesen, "The computational 2d materials database: high-throughput modeling and discovery of atomically thin crystals," *2D Materials*, vol. 5, p. 042002, sep 2018.

[91] M. N. Gjerding, A. Taghizadeh, A. Rasmussen, S. Ali, F. Bertoldo, T. Deilmann, N. R. Knøsgaard, M. Kruse, A. H. Larsen, S. Manti, T. G. Pedersen, U. Petralanda, T. Skovhus, M. K. Svendsen, J. J. Mortensen, T. Olsen, and K. S. Thygesen, "Recent progress of the computational 2d materials database (c2db)," *2D Materials*, vol. 8, p. 044002, jul 2021.

[92] R. Frindt, "Single crystals of mos2 several molecular layers thick," *Journal of Applied Physics*, vol. 37, no. 4, pp. 1928–1929, 1966.

[93] J. Wilson and A. Yoffe, "The transition metal dichalcogenides discussion and interpretation of the observed optical, electrical and structural properties," *Advances in Physics*, vol. 18, no. 73, pp. 193–335, 1969.

[94] J. L. Verble and T. J. Wieting, "Lattice mode degeneracy in mos_2 and other layer compounds," *Phys. Rev. Lett.*, vol. 25, pp. 362–365, Aug 1970.

[95] H. Zeng, G.-B. Liu, J. Dai, Y. Yan, B. Zhu, R. He, L. Xie, S. Xu, X. Chen, W. Yao, and X. Cui, "Optical signature of symmetry variations and spin-valley coupling in atomically thin tungsten dichalcogenides," *Scientific reports*, vol. 3, no. 1, pp. 1–5, 2013.

[96] M. Geisler, X. Cui, J. Wang, T. Rindzevicius, L. Gammelgaard, B. S. Jessen, P. A. D. Gonçalves, F. Todisco, P. Bøggild, A. Boisen, M. Wubs, N. A. Mortensen, S. Xiao, and N. Stenger, "Single-crystalline gold nanodisks on ws2 mono-and multilayers for strong coupling at room temperature," *Acs Photonics*, vol. 6, no. 4, pp. 994–1001, 2019.

[97] Y. Zhou, G. Scuri, J. Sung, R. J. Gelly, D. S. Wild, K. De Greve, A. Y. Joe, T. Taniguchi, K. Watanabe, P. Kim, M. D. Lukin, and H. Park, "Controlling excitons in an atomically thin membrane with a mirror," *Phys. Rev. Lett.*, vol. 124, p. 027401, Jan 2020.

[98] J. Vogelsang, L. Wittenbecher, D. Pan, J. Sun, S. Mikaelsson, C. L. Arnold, A. L'Huillier, H. Xu, and A. Mikkelsen, "Coherent excitation and control of plasmons on gold using two-dimensional transition metal dichalcogenides," *ACS Photonics*, vol. 8, no. 6, pp. 1607–1615, 2021.

[99] H. Gu, B. Song, M. Fang, Y. Hong, X. Chen, H. Jiang, W. Ren, and S. Liu, "Layer-dependent dielectric and optical properties of centimeter-scale 2d wse2: evolution from a single layer to few layers," *Nanoscale*, vol. 11, no. 47, pp. 22762–22771, 2019.

[100] Y. Li, A. Chernikov, X. Zhang, A. Rigosi, H. M. Hill, A. M. Van Der Zande, D. A. Chenet, E.-M. Shih, J. Hone, and T. F. Heinz, "Measurement of the optical dielectric function of monolayer transition-metal dichalcogenides: mos2, mose2, ws2, and wse2," *Physical Review B*, vol. 90, no. 20, p. 205422, 2014.

[101] G.-H. Jung, S. Yoo, and Q.-H. Park, "Measuring the optical permittivity of two-dimensional materials without a priori knowledge of electronic transitions," *Nanophotonics*, vol. 8, no. 2, pp. 263–270, 2019.

[102] C. Hsu, R. Frisenda, R. Schmidt, A. Arora, S. M. De Vasconcellos, R. Bratschitsch, H. S. van der Zant, and A. Castellanos-Gomez, "Thickness-dependent refractive index of 1l, 2l, and 3l mos2, mose2, ws2, and wse2," *Advanced optical materials*, vol. 7, no. 13, p. 1900239, 2019.

[103] S. Yoo and Q.-H. Park, "Spectroscopic ellipsometry for low-dimensional materials and heterostructures," *Nanophotonics*, 2022.

[104] K. M. Islam, R. Synowicki, T. Ismael, I. Oguntoye, N. Grinalds, and M. D. Escarra, "In-plane and out-of-plane optical properties of monolayer, few-layer, and thin-film mos2 from 190 to 1700 nm and their application in photonic device design," *Advanced Photonics Research*, vol. 2, no. 5, p. 2000180, 2021.

[105] F. L. Ruta, A. J. Sternbach, A. B. Dieng, A. S. McLeod, and D. Basov, "Quantitative nanoinfrared spectroscopy of anisotropic van der waals materials," *Nano letters*, vol. 20, no. 11, pp. 7933–7940, 2020.

[106] N. Deng, H. Long, K. Wang, X. Han, B. Wang, K. Wang, and P. Lu, "Giant optical anisotropy of ws2 flakes in the visible region characterized by au substrate assisted near-field optical microscopy," *Nanotechnology*, vol. 33, no. 34, p. 345201, 2022.

[107] P. Gonçalves, L. Bertelsen, S. Xiao, and N. A. Mortensen, "Plasmon-exciton polaritons in two-dimensional semiconductor/metal interfaces," *Physical Review B*, vol. 97, no. 4, p. 041402, 2018.

[108] R. B. Iyer, Y. Luan, R. Shinar, J. Shinar, and Z. Fei, "Nano-optical imaging of exciton-plasmon polaritons in wse2/au heterostructures," *Nanoscale*, 2022.

[109] V. E. Babicheva, S. Gamage, L. Zhen, S. B. Cronin, V. S. Yakovlev, and Y. Abate, "Near-field surface waves in few-layer mos2," *Acs Photonics*, vol. 5, no. 6, pp. 2106–2112, 2018.

[110] S. Haroche and D. Kleppner, "Cavity quantum electrodynamics," *Phys. Today*, vol. 42, no. 1, p. 013901, 1989.

[111] P. Törmä and W. L. Barnes, "Strong coupling between surface plasmon polaritons and emitters: a review," *Reports on Progress in Physics*, vol. 78, no. 1, p. 013901, 2014.

[112] T. Zhan, X. Shi, Y. Dai, X. Liu, and J. Zi, "Transfer matrix method for optics in graphene layers," *Journal of Physics: Condensed Matter*, vol. 25, no. 21, p. 215301, 2013.

[113] P. Yeh, *Optical Waves in Layered Media.* John Wiley & Sons, 1988.

[114] U. Hohenester, *Nano and Quantum Optics.* Springer, 2020.

[115] B. E. Saleh and M. C. Teich, *Fundamentals of Photonics.* john Wiley & Sons, 2007.

[116] B. Majérus, E. Dremetsika, M. Lobet, L. Henrard, and P. Kockaert, "Electrodynamics of two-dimensional materials: Role of anisotropy," *Physical Review B*, vol. 98, no. 12, p. 125419, 2018.

[117] A.-G. Hammid, R. Gnawali, P. P. Banerjee, L. Sun, J. Slagle, and D. Evans, "2× 2 anisotropic transfer matrix approach for optical propagation in uniaxial transmission filter structures," *Optics express*, vol. 28, no. 24, pp. 35761–35783, 2020.

[118] J. Hao and L. Zhou, "Electromagnetic wave scatterings by anisotropic metamaterials: Generalized 4× 4 transfer-matrix method," *Physical Review B*, vol. 77, no. 9, p. 094201, 2008.

[119] E. Alexeev, "Guide: Viscoelastic transfer of 2d material using pdms." `https://www.ossila.com/pages/viscoelastic-transfer-of-2d-material-using-pdms`. Accessed: 2022-10-10.

[120] A. Castellanos-Gomez, M. Buscema, R. Molenaar, V. Singh, L. Janssen, H. S. Van Der Zant, and G. A. Steele, “Deterministic transfer of two-dimensional materials by all-dry viscoelastic stamping,” *2D Materials*, vol. 1, no. 1, p. 011002, 2014.

[121] R. N. Bracewell, *The Fourier Transform and its Applications - 3rd Ed.* McGraw-Hill New York, 1986.

[122] “The Mathworks, Inc. tukey (tapered cosine) window.” `https://se.mathworks.com/help/signal/ref/tukeywin.html`. Accessed: 2022-10-21.

[123] M. Albrechtsen, B. V. Lahijani, R. E. Christiansen, V. T. H. Nguyen, L. N. Casses, S. E. Hansen, N. Stenger, O. Sigmund, H. Jansen, J. Mørk, and S. Stobbe, “Nanometer-scale photon confinement inside dielectrics,” *arXiv preprint arXiv:2108.01681*, 2021.